



CRANFIELD UNIVERSITY

**Peter J. Stuttaford**

**Preliminary Gas Turbine Combustor  
Design Using a Network Approach**

School of Mechanical Engineering

PhD

CRANFIELD UNIVERSITY  
School of Mechanical Engineering

PhD Thesis

1997

**Peter J. Stuttaford**

**Preliminary Gas Turbine Combustor  
Design Using a Network Approach**

Supervisor: Dr Philip A. Rubini

February 1997

This thesis is submitted for the degree of  
Doctor of Philosophy

# **Abstract**

Gas turbine combustor design represents an ambitious task in numerical and experimental analysis. A significant number of competing criteria must be optimised within specified constraints in order to satisfy legislative and performance requirements. Currently, preliminary combustor flow and heat transfer design procedures, which by necessity involve semi-empirical models, are often restricted in their range of application.

The objective of this work is the development of a versatile design tool able to model all conceivable gas turbine combustor types. A network approach provides the foundation for a complete flow and heat transfer analysis to meet this goal.

The network method divides the combustor into a number of independent interconnected sub-flows. A pressure-correction methodology solves the continuity equation and a pressure-drop/flow-rate relationship. A constrained equilibrium calculation, incorporating mixing and recirculation models, simulates the combustion process. The new procedures are validated against numerical and experimental data within three annular combustors and one reverse flow combustor. A full conjugate heat transfer model is developed to allow the calculation of liner wall temperature characteristics. The effects of conduction, convection and radiation are included in the model. Film cooling and liner heat pick-up effects are included in the convection calculation. Radiation represents the most difficult mode of heat transfer to simulate in the combustion environment. A discrete transfer radiation model is developed and validated for use within the network solver. The effects of soot concentration on radiation is evaluated with the introduction of radial properties profiles. The accuracy of the heat transfer models are evaluated with comparisons to experimental thermal paint temperature data on a reverse flow and annular combustors.

The resulting network analysis code represents a powerful design tool for the combustion engineer incorporating a novel and unique strategy.

# Acknowledgements

The author would like to thank his supervisor, Dr Philip Rubini, for the advice and direction provided in completing this work.

The funding and support provided by Rolls-Royce and the Defence Research Agency in completing the work is gratefully appreciated. The valuable technical input provided by Mr David Lowe, Dr Chris Priddin and others at Rolls-Royce enhanced the content of this work. Thanks also for the assistance and direction provided by Dr Chris Wilson and Mr Richard Seoud of the Defence Research Agency.

The support and humour of family and friends helped keep the task at hand in perspective.

Finally, thanks to Jean-Marie for providing support and a welcome, much needed, distraction.



# Contents

ABSTRACT .....	i
ACKNOWLEDGEMENTS.....	ii
CONTENTS .....	iii
NOMENCLATURE.....	vi
1. INTRODUCTION.....	1
2. GAS TURBINE COMBUSTOR MODELLING FOR DESIGN .....	4
3. THE NETWORK ALGORITHM.....	13
3.1 INTRODUCTION .....	13
3.2 SOLUTION OF THE FLOW EQUATIONS .....	16
3.3 SOLUTION TO THE ENERGY EQUATION.....	25
3.4 NETWORK ALGORITHM OVERALL SOLUTION STRATEGY .....	28
4. COMBUSTOR FLOW MODELLING.....	30
4.1 INTRODUCTION .....	30
4.2 SEMI-EMPIRICAL ELEMENT GOVERNING EQUATIONS.....	33
4.2.1 Duct with area change (DG) .....	33
4.2.2 Restrictor with discharge coefficient (RD).....	35
4.2.3 Restrictor with loss coefficient (RL).....	36
4.2.4 Diffuser pressure drop with loss coefficient (PD) .....	37
4.2.5 Ports and Cooling/Dilution holes (HO).....	39
4.2.6 Radial pressure gradient.....	45
4.3 CONSTRAINED EQUILIBRIUM COMBUSTION COMPUTATION .....	46

4.4	MIXING AND RECIRCULATION MODELS .....	50
4.5	REAL GAS PROPERTY MODELS .....	52
4.6	COMBUSTOR CASE STUDIES .....	54
4.6.1	<i>Isothermal Annular Combustor .1.</i> .....	54
4.6.1.1	Network specification .....	54
4.6.1.2	Discussion .....	55
4.6.2	<i>Isothermal Annular Combustor .2.</i> .....	57
4.6.2.1	Network specification .....	57
4.6.2.2	Discussion .....	57
4.6.3	<i>Isothermal Annular Combustor .3.</i> .....	59
4.6.3.1	Network specification .....	59
4.6.3.2	Discussion .....	59
4.6.4	<i>Reverse Flow Combustor</i> .....	61
4.6.4.1	Network specification .....	61
4.6.4.2	Discussion .....	62
4.7	CONCLUSIONS .....	64
	Figures.....	66
<b>5.</b>	<b>COMBUSTOR HEAT TRANSFER MODELLING .....</b>	<b>80</b>
5.1	INTRODUCTION.....	80
5.2	CONSTRAINED EQUILIBRIUM ADIABATIC CORRECTION .....	83
5.3	CONJUGATE HEAT TRANSFER MODELS .....	84
5.4	CONDUCTION (CD).....	86
5.5	ANNULUS HEAT TRANSFER (AHT).....	91
5.5.1	<i>Convection</i> .....	91
5.5.2	<i>Radiation</i> .....	93
5.6	FLAMETUBE HEAT TRANSFER (FHT).....	95
5.6.1	<i>Convection</i> .....	95
5.6.2	<i>Radiation</i> .....	104
5.7	GAS TURBINE COMBUSTOR CASE STUDIES .....	107

5.7.1 Reverse Flow Combustor.....	107
5.7.2 Annular Combustor.....	110
5.8 CONCLUSIONS .....	112
Figures.....	114
 <b>6. COMBUSTOR RADIATION MODELLING .....</b>	<b>121</b>
6.1 INTRODUCTION.....	121
6.2 RADIATION MODELLING IN GAS TURBINE COMBUSTORS .....	124
6.3 DISCRETE TRANSFER RADIATION MODEL.....	126
6.3.1 Introduction .....	126
6.3.2 Numerical Algorithm.....	126
6.3.3 Quadrature Formulation.....	130
6.3.4 Ray Tracing .....	132
6.4 PROPERTIES MODELLING .....	138
6.4.1 Introduction .....	138
6.4.2 Gas Properties .....	138
6.4.3 Soot Properties.....	145
6.5 PROFILES/TEMPLATES.....	152
6.6 RESULTS AND DISCUSSION.....	154
6.6.1 Validation of DT method for simple geometries.....	154
6.6.2 Combustor simulations.....	156
6.7 CONCLUSIONS .....	162
Figures.....	164
 <b>7. CONCLUSIONS .....</b>	<b>181</b>
 <b>8. RECOMMENDATIONS FOR FUTURE WORK .....</b>	<b>183</b>
 <b>9. REFERENCES .....</b>	<b>186</b>

# Nomenclature

$A$  = area

$C$  = convective heat flux

$C_D$  = discharge coefficient

$C_L$  = loss coefficient

$C_C$  = contraction coefficient

$C_p$  = specific heat at constant pressure

$C_v$  = specific heat at constant volume

$C_0$  = soot index of refraction constant

$C_2$  = Planck's second constant = 0.0143879 mK

$C/H$  = carbon/hydrogen ratio of the fuel

$d$  = hole diameter or external mass flow into node

$dA$  = the surface area associated with the ray launch point

$d\Omega$  = associated solid angle

$D$  = duct diameter

$e$  = wall roughness

$E$  = energy equation source term

$f$  = friction factor

$f_v$  = soot volume fraction

$ff$  = fuel mass fraction

$h_{i,j}$  = convective heat transfer coefficient

$H$  = feature heat pick-up

$I$  = radiant intensity in the direction  $\Omega$

$I_w$  = incident intensity

$k$  = conductivity

$k_a$  = gas absorption coefficient

$k_s$  = gas scattering coefficient

$K$  = conductive heat flux or extinction coefficient

$l$  = hole length or lip length

$l_b$  = mean beam length

$L$  = luminosity factor

$\dot{m}$  = mass flow rate

$M$  = Mach number

$n, k$  = infrared-average optical constants of soot

$N_\theta$  = number of rays in the  $\theta$  direction, over the range  $0 < \theta < \pi/2$

$N_\phi$  = number of rays in the  $\phi$  direction, over the range  $0 < \phi < 2\pi$

$Nu$  = Nusselt number

$p$  = hole pitch

$P$  = pressure

$Pr$  = Prandtl number

$P(\Omega, \Omega')$  = probability that the incident radiation in the direction  $\Omega'$  will  
scattered into the increment of solid angle  $d\Omega$  about  $\Omega$

$q_+$  = energy flux outgoing

$q_-$  = energy flux incident

$q$  = local fuel/air ratio

$Q$  = volumetric flow rate

$Q_{radiation}$  = total radiative heat flux

$r$  = plunging radius

$R$  = gas constant

$R_1$  = radiative heat flux to casing

$R_2$  = radiative heat flux to flametube liner

$R_{ij}$  = conductive heat transfer coefficient terms

$Re$  = Reynolds number

$s$  = distance in the  $\Omega$  direction

$\Delta s$  = distance travelled along ray in the control volume

$S$  = slot or lip height

$t$  = material thickness

$T$  = temperature

$U$  = velocity

$V$  = velocity

$w$  = annulus width

$x$  = entrance length

$z$  = hole pitch

### Greek letters

$\alpha$  = blockage factor, or gas absorptivity, or pressure loss factor

$\beta$  = turbulence parameter

$\Omega$  = ray solid angle

$\epsilon$  = emissivity or convergence parameter

$\eta$  = film effectiveness

$\mu$  = dynamic viscosity

$\theta$  = injection angle or polar angle, angle between the ray direction  $s$  and the normal to the surface

$\phi$  = azimuthal angle

$\gamma$  = ratio of specific heats

$\Delta\theta$  = solid angle increment in the  $\theta$  direction

$\Delta\phi$  = solid angle increment in the  $\phi$  direction

$\rho$  = density

$\sigma$  = Stefan-Boltzmann constant =  $5.67 \times 10^{-8} \text{ W}/(\text{m}^2\text{K}^4)$

$\psi$  = air mass fraction

### Subscripts

0 = total

1 = hot or upstream side

2 = cold or downstream side

$a$  = cooling air

$an$  = annulus

$ca$  = casing

$f$  = film

$fi$  = initial film value

$fl$  = flametube

$i$  = centre node

$i,j$  = branch element

$g$  = hot (flametube) gas

$m$  = mean value

$n$  = entering volume element

$n+1$  = leaving volume element

$n_{ij}$  = branch node

$p$  = previous upstream axial location

$s$  = soot

$S$  = static

$T$  = total

$w$  = wall

$y$  = radial direction

$z$  = circumferential direction

# 1. Introduction

Preliminary gas turbine combustor design presents a challenging process of analytical analysis and rig testing. The development of a new combustor involves the application of a large pool of knowledge to conceptualise an overall structure. The design typically involves the use of cumbersome, geometry restrictive semi-empirical models which have the advantage of rapid execution times on the order of a few minutes or less. The results of such an analysis becomes the input for more thorough investigations, such as computational fluid dynamics (CFD) simulations and rig testing. The cost of rig testing and to a lesser degree CFD prohibits their use to the minimum necessary to produce a feasible design. Combustor simulations are therefore optimised using semi-empirical models as much as possible prior to further expensive advanced development. The more accurate this initial design the more expedient the following phases of development.

The progress in gas turbine combustor technology has led to more unusual and diverse designs which the more conventional one-dimensional preliminary design procedures have difficulty in solving. The need for a highly flexible, accurate analysis, capable of modelling the flow and heat transfer in all types of combustor irrespective of geometry was identified. A further key requirement was that the wealth of knowledge built up over the past few decades on gas turbine combustor design could be simply incorporated in an unrestrictive ongoing basis into the new procedure.

The new combustor analysis should provide mass flow splits and pressure drops through all combustor features. A full conjugate wall heat transfer analysis, including conduction, convection and radiation, was required to compute the liner wall thermal load and temperature distribution at any operating condition.

A network method was selected as a basis for meeting the above mentioned objectives. The flexibility of the approach has been well demonstrated in pipe network analysis. An existing pipe network solver was selected to form the foundation of the new gas turbine



combustor design tool. A flow and heat transfer analysis was developed to meet the requirements of a combustor design tool with the incorporation of detailed combustor specific sub-models.

The structure of the thesis follows the development of the gas turbine combustor network algorithm. The methodology used is described and discussed in detail. Due to the industrial sensitivity of portions of the physical data used in the combustor validation a complete description of the test cases are not possible. However, this does not limit the depth of the comparisons made and illustrated in validating the new algorithm.

A review of combustor design procedures in Chapter 2 provides the context and further justification for the network analysis developed in this work.

The overall governing equations of flow and heat transfer are presented in the form required by the network solver in Chapter 3. The network solution algorithm and the methods used to solve the overall governing equations are described. A pressure correction procedure is used to solve the flow equations and a Gauss-Seidel scheme is used to solve the energy equation. The application of the network features to provide a complete combustor model are discussed.

Chapter 4 presents a detailed description of the elements required to completely model the combustor flow characteristics, including pressure drops and mass flow splits throughout the combustor. The inclusion of a constrained equilibrium computation for the calculation of a local adiabatic flame temperature is described. Mixing models are used to provide corrected local fuel/air ratios for this calculation. A real gas properties model accounts for the changing physical properties of the combustion gases in the system. The new strategy is validated with comparisons between the network solver results and those of a proven one-dimensional combustor solver for three significantly different annular gas turbine combustors. Finally, a reverse flow combustor network analysis is compared with experimental data and associated calculations of mass flow splits and pressure drops.

The development of a full conjugate heat transfer model is presented in Chapter 5. A one and two-dimensional conduction model was developed for computing the heat transferred through the liner wall. Convection models account for the effects of film cooling on the hot-side of the liner. Heat pick up within the liner walls through features containing significant areas of heat transfer are described. A simple radiation model relating to the bulk combustion gas properties is included in the calculation. The network set-up required to model the heat transfer characteristics are described. The conjugate heat transfer wall temperature results are compared to experimental thermal paint measurements in an annular and reverse flow combustor to evaluate the accuracy of the procedure. The methodology and results of Chapter 4 and Chapter 5 have been published (Stuttaford and Rubini, 1996).

Thermal radiation within the combustor flametube is responsible for a significant proportion of the heat transferred to the liner wall. The need for a detailed radiative heat transfer analysis was identified. A new radiation procedure was developed using the discrete transfer radiation strategy. A complete description of the analysis is presented in Chapter 6. The effects of the products of combustion, including soot, are included in the radiation calculation, and the facility to resolve the radial profiles of temperature and soot in the radiation calculation are described. The radiation model is validated on simple cylindrical geometries. Three variations of a modern annular gas turbine combustor are modelled using the new analysis, and the wall temperatures and heat fluxes evaluated. The discrete transfer radiation model has been assessed in the framework of the network solver in a published work (Stuttaford and Rubini, 1997).

Finally the overall conclusions of the analysis are presented, and recommendations made for further development and use of this new preliminary gas turbine combustor design approach.

## **2. Gas Turbine Combustor Modelling for Design**

Gas turbine combustor development involves a lengthy process of analysis, beginning with the conception of overall performance requirements. Given an idea of the sizing requirements of a combustor, a basic geometrical layout may be developed providing the first step to detailed empirically based design validation, followed by more complex computational fluid dynamics (CFD) simulations and rig testing. Many of today's new combustors are extensions of well proven designs, and modified scale versions of these designs provide the first pass for the design validation procedures.

Gas turbine combustor designs should meet some fundamental requirements; complete combustion, minimal total pressure loss, combustion stability, smooth exit temperature profile, narrow cross-section and short length, no possibility of flameout, relightability, and usage over a wide range of operating conditions (Mattingly, 1996). Unfortunately the design requirements of a combustor conflict with one another and compromises must be made in finding the optimum parameters. The complexity of the physical process within a gas turbine combustion chamber has prevented the development of purely analytical tools able to completely model a combustor. The harsh operating environment of a combustion chamber has also precluded the possibility of making detailed measurements within the flametube. These limitations have resulted in past workable designs having to be based to a large degree on experience, extrapolation and rig testing (Oates, 1989).

Early combustor modelling relied entirely on empirical procedures, which became increasingly restrictive as the combustors diverged from the operating parameters for which the empirical models were developed. The development of more complex theoretical models has reduced this reliance on empirical procedures to the extent that combustor specific correlations may be neglected altogether. However, these new models remain severely limited in their ability to quantitatively capture the physical effects within a combustor.

Practical gas turbine combustors contain complex three-dimensional turbulent flow fields with coupled multiphase chemical kinetics, evaporation, and heat transfer mechanisms. Improvements in the understanding of the interaction between turbulence and kinetics, gas and solid phase kinetics, droplet/particle cloud combustion, soot formation and oxidation, and flame structure are of prime importance to a complete theoretical simulation of a gas turbine combustor (Gupta and Lilley, 1994). The prediction of levels of oxides of nitrogen, carbon monoxide, and unburned hydrocarbons produced by combustors has recently become a prime concern in meeting new environmental legislation (Beer, 1995). The interdependencies of all these characteristics do not allow the design engineer to ignore the effects of one phenomena in obtaining information on the effects of another, thus making the system extremely difficult to model. A further difficulty is in the specification of boundary conditions, the inferior resolution of which hampers the ability of computational models to predict the combustor characteristics (Mongia, 1994).

Preliminary gas turbine combustor design procedures are based on overall performance requirements including combustion efficiency, lean lightoff and blowoff limits, exit temperature traverse, and emissions of CO and NO<sub>x</sub>. Mellor and Fritsky (1990) demonstrated the application of a characteristic time model in achieving these goals. The model provided full details of primary and secondary air requirements. The algorithm was calibrated using emissions data from representative aircraft engine combustors. Comparisons with rig test data proved reasonably accurate. This form of analysis provides a sound basis for more detailed computations, giving predictions of mass flow splits, pressure loss, and heat transfer. The results allow a fine tuning procedure improving upon the initial design. Variations of this method have been successfully employed to estimate emissions from a wide range of combustor types (Connors et al, 1996).

A number of empirically based models have been developed in the past. Turbulent flame speed models simulate the effect of turbulence on combustion by calculating a turbulent

flame speed based on analogy with a laminar flame speed. The turbulent flame speed is used to compute the propagation of the flame from ignition sources within the flametube, thus resolving the overall combustor dimensions and performance. The analysis was developed for ramjet type combustors with constant cross-section and no secondary air addition (Hammond and Mellor, 1970). The flame speed is calculated assuming a uniform propagation of the flame from the flame holder. None of these requirements are met in the turbulent recirculating flow of a gas turbine combustor. Thus, finding a characteristic flame speed becomes increasingly improbable.

Microvolume burning models account for mixing and reaction chemistry in a series of turbulent eddies within small cubic volumes comprising the flametube. The eddies are discrete masses of fluid which move relative to other eddies. Ultimately the eddies, containing either burned or unburned gases, are transported out of the combustion zone by turbulent fluctuations, at which point they mix with eddies of fresh gas. Ignition occurs and the eddy burns if a sufficiently high temperature is reached. Although in turbulent flow eddies do form and decay over a certain mixing length, assuming all eddies to be of a similar size is a gross approximation. Further difficulties arise in predicting the mixing rate and ignition delay time within the eddy (Hammond and Mellor, 1970).

Stirred reactor models assume that the turbulence level is so high that mixing is instantaneous and therefore the mixing is assumed negligible in comparison to the reaction rate. A stirred reactor consists of a zone of homogeneous reacting mixture. Flow entering the volume is assumed to be instantaneously mixed, so combustion depends on reaction kinetics alone. The same amount of flow leaves a volume as that which arrives, and the flow leaving the volume is assumed to be of the same composition as that within the volume. Stirred reactors may be connected in series to represent secondary air mixing, or in parallel to simulate recirculation zones. Hammond and Mellor (1970) developed a model incorporating stirred reactors in parallel to model the primary zone recirculation followed by a series of plug flow reactors (a continuous series of stirred reactors infinitesimally thick through which the flow passes). The model was able

to predict qualitatively accurate performance characteristics within a combustor, but the resolution was limited.

Swithenbank et al (1973) developed a model containing partially stirred reactors, accounting for combustion and unmixedness. The analysis included the effects of turbulent mixing, droplet evaporation, chemical kinetics, and flow recirculation. The heat release from the propane/air combustion was calculated from a reaction-rate equation. A heat balance within the stirred reactors between the heat input due to chemical reaction and heat removed, was formulated in terms of oxygen conversion. The mixedness of a partially stirred reactor was a function of the combustor geometry and the method used for flame stabilisation. Interconnected stirred reactor modules were used to simulate the primary, secondary and dilution zones. The model was shown to predict blow-off stability limits, overall combustion efficiency, combustion intensity, and overall pressure loss. The strategy also provided information on  $\text{NO}_x$  and unburned hydrocarbon levels, as well as noise emissions. The method was successfully verified using seven interconnected stirred reactors to represent an experimental gas turbine combustor flametube.

Mellor (1978) in an evaluation of modular gas turbine models found the approach of Mosier et al (1973), and Mado and Roberts (1974) the most successful. In this model the internal flowfield is approximated by a series of co-annular, one-dimensional reacting streamtubes. A one-dimensional streamtube represents the flow recirculation in the primary zone, i.e. a well stirred reactor. A procedure was developed whereby the streamtubes exchange mass, momentum and energy via turbulent mixing. Sub-models were included to account for the chemistry and fuel spray. The effects of port and film cooling air injection were modelled semi-empirically. The method was shown to reasonably predict emissions trends with differing operating conditions and configurations.

Stirred reactor theory remains a powerful design and development tool in predicting emissions. Detailed analysis of the conflicting requirements of combustion performance

and emissions in lean premixed primary zones has been performed (Zelina et al, 1996), with favourable comparisons to measured data. The calculations were able to well predict fuel effects on emissions. Increasing hydrogen content of the fuel clearly illustrated an increase in gaseous emissions of pollutants.

One-dimensional models, such as that described by Burrus et al (1987), have been used successfully for the preliminary design and sizing of a combustor. Given target airflow distributions, the required flow areas could be computed, or given the areas, the various flow splits and pressure-drops may be calculated. However, the analysis lacked a heat transfer capability and could not predict exit pattern factors or three dimensional dependent performance characteristics.

Murthy (1988) developed a one-dimensional analysis for examining the flow and heat transfer within straight tubular, tubo-annular and annular combustors. A wealth of semi-empirical correlations were used to model specific flow features and heat fluxes. A simplified reaction mechanism was used to obtain equilibrium species concentrations, providing an adiabatic flame temperature which was corrected for heat loss. The procedure proved to be a useful combustor design analysis code. However, the algorithm was limited in the range of geometries it could model.

Rodriguez and O'Brien (1997) developed a one-dimensional, steady model for straight and reverse flow gas turbine combustors. The model demonstrated the ability to predict pressure drop and mass flow splits. An equilibrium model was used to estimate the heat release due to combustion. The accuracy of the method was not evaluated against real engine data. The ability of the algorithm to model more unusual geometries, such as multi-annular combustors, appears limited by a reliance on continuous flow streams.

Multi-dimensional resolution is a shortfall of semi-empirical algorithms. The one-dimensional models incorporate numerous experimental data, and empirically derived correlations to support the simplified overall governing equations (Mellor, 1990).

Empirically based procedures have led to successful evolutionary combustor improvements, but they exhibit shortfalls when significantly different technological designs from those of proven concepts are required. Advances in CFD modelling have allowed the successful simulation of gas turbine combustor flows. However, the accuracy of such simulations remains limited by the sub-models they employ. CFD computations require the time consuming procedure of grid generation, boundary condition specification, and obtaining solution convergence.

Combining detailed three-dimensional physical models with semi-empirical formulations, compensating for shortfalls in the physical description, have proven a valuable combustor design tool (Holdeman, et al, 1989). Examples of the successful application of such a procedure to specific combustors are given by Mongia et al (1986). Historical trend lines, and one dimensional models were used to develop a preliminary design based upon the engine cycle and mission specifications. This initial analysis must be performed interactively with other engine components, especially the compressor and turbine. A detailed empirical/analytical design procedure follows, targeting specific combustion chamber goals. These include combustion efficiency, overall pressure drop, smoke, lean blowout, ignition characteristics, combustor exit temperature traverse, liner wall temperatures and gradients, and other overall requirements such as weight, complexity, maintainability, etc. Following a satisfactory specification of these goals combustor development may proceed. Development involves rig testing specific components, engine testing, and further analysis using analytical tools. This is an iterative procedure, and minimising the number of iterations significantly reduces the overall cost. The better the analytical description of the new combustor the fewer such iterations will be required to achieve an acceptable combustor design. A three-dimensional empirical/analytical procedure was employed to augment the basic design, providing a good qualitative analysis, using the sub-models of turbulent reactive flow available.

A number of detailed three-dimensional gas turbine combustor flow strategies have been recently developed with varying degrees of success. Shyy et al (1989) used a non-orthogonal curvilinear multigrid solver with a standard  $k-\epsilon$  turbulence model and a



combustion model with an assumed probability density function (pdf) and conserved scalar formulation. Three annular combustors were evaluated and comparisons made with experimental data. The exit temperature traverses compared well, with the essential characteristics of the flowfield being captured. The liner wall was assumed adiabatic.

Rizk and Mongia (1991) obtained satisfactory agreement with experimental results for a range of combustors under various operating conditions, using a three-dimensional analytical/empirical performance model. Emissions, soot oxidation/formation, and lean blowoff limits were based upon semi-empirical formulations using the detailed three-dimensional characteristics of the flowfield computed. Flametube wall temperature calculations were performed incorporating a semi-empirical correlation for the radiative heat flux in a luminous hydrocarbon burning system.

Bai and Fuchs (1995) performed a sensitivity analysis of the gas turbine combustor flowfield to the interaction between turbulence and combustion. The species concentrations obtained were compared with experimental measurements. The calculation incorporated a detailed radiation model to compute radiative sources within the flowfield. Results comparable to measured data were obtained over a range of conditions.

Hybrid approaches, combining semi-empirical correlations with computational combustor dynamics (CCD) have been used with success to predict emissions, smoke, lean blowout, ignition, pattern factor and liner wall temperatures. A variation of this method, anchored CCD, has been developed by Danis et al (1996). The objective of the analysis was to provide quantitatively accurate predictions of emissions, performance, operability, liner wall temperature, and life characteristics of a new combustor. The approach makes use of existing CFD codes and sub-models for combustion. The process of anchoring may be performed in several ways. Firstly, the modelling strategy may be calibrated against a specific combustor, and then applied identically to other combustors.

The accuracy of such methods becomes limiting as the combustors vary more from the original calibration case. A second approach continuously refines the anchoring as more data becomes available. This too may prove difficult if the data becomes conflicting. A final scheme locally anchors empirical constants with appropriate inlet and boundary conditions for specific classes of combustor designs. Although this may prove to be the most accurate it becomes limiting in the evaluation of new designs. Danis et al (1996) only evaluated the first approach. A double annular combustor was used for the calibration and then computations were performed on three annular and two double annular combustors. The agreement between measured and predicted values was good in the low power range. The accuracy over the whole power range was less promising and the authors are currently addressing this issue. Nevertheless the authors were able to demonstrate the usefulness of the approach in a developmental double annular combustor with quantitatively accurate pre-test predictions of later measurements.

Mavris and Roth (1997) demonstrated the combination of a suite of computational models to evaluate a combustor liner cooling configuration for a high speed civil transport. A response surface analysis, providing a simplified model for the liner temperature, was used to optimise the impingement cooling requirement of the combustor liner wall. The technique demonstrated the usefulness of a simplified model, derived from a series of complex multi-dimensional algorithms, in combustor design and optimisation.

Ultimately rig testing remains a key feature in the design and development of combustors. Although numerical analysis has limited the need for such testing it remains the final confidence building step to production of a new combustor. Although costly and time consuming, measurements provide confidence in design as well as a key source of information in validating and improving computational schemes. Typically, engine rig testing is used to ensure pattern factors compatible with the downstream turbine requirements, and measure emissions levels. The other critical component is the flametube liner wall, and thermal paint or thermocouples may be employed to measure the wall temperature. The ability to make detailed measurements has gradually improved

over time, and although there are still limitations on the measurements which can be cost effectively made, detailed flow field measurements within combustors are possible (Switzer et al, 1994 and Hanson, 1997).

The use of three-dimensional computational models is a time consuming task, and only undertaken in an attempt to visualise a combustor for which a preliminary design has already been developed. Phenomena displayed by this more complicated analysis may lead to modifications in the design prior and during rig testing. Although CFD does economise the rig testing requirement, by predicting the flowfield structure well, it remains a time consuming method of analysis producing only qualitatively accurate results.

The solution procedures discussed above are typically linked to the continuous geometry of the combustor, making them very complex in some cases. The modelling task could be greatly simplified if the geometry could be made independent of the governing equations. Network methods offer this possibility.

A flexible geometry independent semi-empirical model, while lacking the resolution of the three-dimensional models, is still able to predict reasonably accurate results very rapidly. The flexibility of a network analysis allows the relatively simple modelling of complex geometries, and removes many of the restrictions placed upon conventional one-dimensional models. The sub-models within these solution procedures, e.g. equilibrium models, film-cooling models, radiation models, etc. can be easily modified as required. The network approach offers a simple modular framework for incorporating the latest sub-models in an algorithm, enabling the complete modelling of a combustor.

The following chapters will provide a detailed description of the application of a network method to a gas turbine combustor design analysis.

## 3. The Network Algorithm

### 3.1 Introduction

A variety of methods are available for solving the Navier-Stokes equations. Typically the solutions of these equations are linked to continuous geometry, and solved for the entire domain. Network methods offer the possibility of simply divorcing the solution of the overall governing equations from the geometry, i.e. the physical geometry becomes independent of the equations. The effect of the geometry on the parameters within the governing equations are accounted for in the description of the flow through individual geometrical features.

The network method divides the combustor into a series of one-dimensional sub-flows, containing independent semi-empirical governing equations, depending on the feature modelled. These sub-flows are linked together in the overall governing equations to obtain a complete solution of the entire flow field. In this way pressure-drops and flow-splits may be obtained throughout the region of interest. A heat transfer model may be incorporated within this strategy, computing conduction, convection and radiation effects.

The requirement for detailed steady-state analysis of flow and pressure in pipe systems has led to a great deal of work utilising network techniques, which are ideally suited to such solution strategies. The first strategies for solving pipe networks were developed by Hardy Cross (1936). In this case a method was developed for solving closed loop equations based on adjusting the flow rates to individually balance each of the equations. An alternative method was to adjust the pressure at each of the network nodes to satisfy the continuity equation. Since the adjustments were made independent of each other the method suffered from convergence difficulties (Wood and Rayes, 1981). Digital

computers have made the prospect of solving large networks feasible and a significant amount of development has taken place.

There are essentially three methods for solving networks. These are node methods, loop solvers, and element methods. The first two categories require the specification of initial head pressures for each node, or initial mass flow for each element, with continuity being satisfied within each node (Dupuis et al, 1987). In the third method the continuity equation need not be satisfied.

The advantage of solving loop equations is that they require less computer storage than the other two schemes (Greyvenstein and Laurie, 1994). However, the initial flow distribution must satisfy the continuity equation. A further disadvantage is that the structure of the loop set-up greatly affects the solution efficiency, and deciding the loop structure can become a complicated task.

Element methods do not require that the continuity equation be satisfied when specifying initial flows (Greyvenstein, 1994), and convergence is very rapid. Unfortunately these methods require more computer storage than the other two methods, and also require the specification of a number of loops.

Node methods require less computer storage than element methods, and do not require the specification of loops or initial flows (Greyvenstein, 1994). Node methods have the advantage of being able to use mixed boundary conditions, i.e. mass flow or pressure. CFD calculations typically make use of node methods in solving the Navier-Stokes equations. In an evaluation of the various methodologies Wood and Rayes (1981) found the nodal method to be more unreliable than the other two methods due to the node method's sensitivity to initial pressures, and the inability of the method to account for low resistance lines. However, when successful the node method achieved accurate convergence very rapidly. Nogueira (1993) addressed the problem of low resistance lines, e.g. a large pipe of short length with relatively very low flow, by designing a hybrid

element. The element was incorporated in the governing equations, rectifying the ill-condition of the system of equations.

As networks become large the computer storage requirement may become excessive. Ti and Preece (1992) addressed this issue by separating the large network into a number of sub-networks, significantly reducing the memory requirement. The mathematical efficiency of large networks has also been analysed, and approaches developed which minimise the computational complexity of solution algorithms (Sommer et al, 1993).

A popular node method is the SIMPLE (Semi-Implicit Method for Pressure-Linked Equations) method, described by Patankar (1980). Greyvenstein and Laurie (1994) adapted the SIMPLE algorithm to compressible flow in pipe networks, and developed a reliable analysis applicable to a wide variety of networks. This algorithm was used as a basis for the combustor analysis developed in this work, and is described in the sections which follow.

### 3.2 Solution of the flow equations

The domain of interest is modelled by overlaying a network on the system geometry. The network consists of a number of elements and nodes. The elements represent actual physical features in the domain, e.g. duct sections, holes, etc. The nodes join the elements to one another, thus combining independent features into a meaningful overall structure. The overall governing equations are solved within the nodes, while semi-empirical relationships may be employed to describe the flow through an element.

The procedure used for obtaining a solution to the flow equations is the SIMPLE (Patankar, 1980) pressure correction methodology. The one dimensional flow may be incompressible or compressible.

The overall governing flow equations are the continuity equation, and a pressure-drop/flow rate relationship (Greyvenstein and Laurie, 1994). The continuity equation may be specified as,

$$\sum_{j=1}^J \rho_{i,j} Q_{i,j} s_{i,j} = -d_i \quad i = 1, 2, \dots, J \quad (3.1)$$

and the pressure-drop/flow-rate relationship as,

$$\Delta P_{i,j} = P_{n_{i,j}} - P_i = s_{i,j} H_{i,j} g_{i,j} f_{i,j} \quad (3.2)$$

where,

$$\begin{aligned} g_{i,j} &= g_{i,j}(\rho_{i,j}) \\ f_{i,j} &= f_{i,j}(|Q_{i,j}|) \\ H_{i,j} &= \frac{Q_{i,j}}{|Q_{i,j}|} \end{aligned}$$

The  $s$  terms in Eq. (3.2) are used to relate the flow direction to that specified by the user. The positive direction is taken to be from node 1 to node 2 in setting up the network, so  $s$  is defined as,

$$\begin{aligned} s_{i,j} &= 1 && \text{if the flow is in the positive direction} \\ s_{i,j} &= -1 && \text{if the flow is in the negative direction} \end{aligned}$$

These functional relationships are derived from semi-empirical formulations for combustor features and internal flows. Examples of the formulations, such as the Darcy-Weisbach equation and flow in duct sections, may be found in Jeppson (1977) and Saad (1985). Internal flow effects such as momentum addition and recirculation could be accounted for in the pressure-drop equations, but only from an empirical stand point. The functional relationships are written as coefficients in the overall solution matrix, and simultaneously solved using the direct method discussed later in this section.

For an ideal gas,

$$\rho_{i,j} = \frac{P_{i,j}}{RT_{i,j}} \quad \text{or} \quad \rho_{i,j} = \frac{P_i + P_{n_{i,j}}}{2RT_{i,j}} \quad (3.3)$$

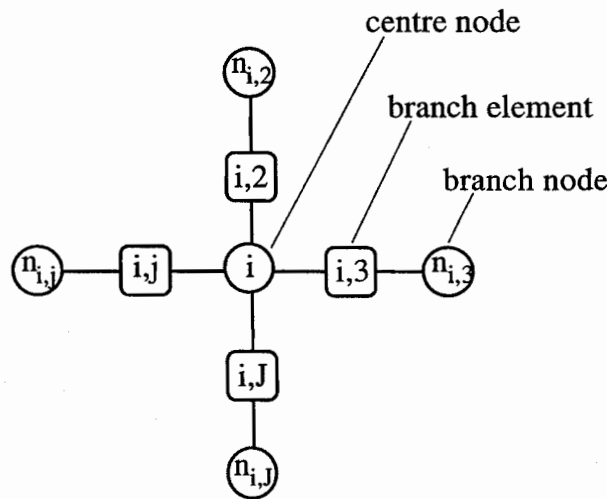


Figure 3.1. Network nomenclature



Figure 3.1. shows a section of a typical network. Initially, the temperatures and pressures at the nodes,  $T_{i,j}^*$  and  $P_i^*$ , are predicted, and if the flow is compressible Eq. (3.3). is used to calculate  $\rho_{i,j}^*$ . Using Eq. (3.2). a predicted flow-rate,  $Q_{i,j}^*$ , is calculated.

The predictions are corrected using the following relationships,

$$\begin{aligned} P &= P^* + P' \\ Q &= Q^* + Q' \\ \rho &= \rho^* + \rho' \end{aligned} \quad (3.4)$$

The \* symbol refers to the predicted values, and the ' symbol indicates the corrections.

The density correction follows from Eq. (3.3),

$$\rho'_{i,j} = \frac{P'_i + P'_{n_{i,j}}}{2RT_{i,j}} \quad (3.5)$$

To correct these values a relationship between the flow-rate and pressure is computed, obtained by differentiating Eq. (3.2). with respect to  $Q_{i,j}$ ,

$$Q'_{i,j} = P'_{n_{i,j}} \left[ \frac{1}{s_{i,j} g_{i,j}^* f l_{i,j}^*} - \frac{H_{i,j} a_{i,j} f_{i,j}^* g l_{i,j}^*}{g_{i,j}^* f l_{i,j}^*} \right] - P'_i \left[ \frac{1}{s_{i,j} g_{i,j}^* f l_{i,j}^*} + \frac{H_{i,j} a_{i,j} f_{i,j}^* g l_{i,j}^*}{g_{i,j}^* f l_{i,j}^*} \right] \quad (3.6)$$

where,

$$a_{i,j} = \frac{1}{2RT_{i,j}} ; \quad g l_{i,j} = \frac{\partial g_{i,j}}{\partial \rho_{i,j}} ; \quad f l_{i,j} = \frac{\partial f_{i,j}}{\partial |Q_{i,j}|}$$

The continuity equation, Eq. (3.1), is modified by including the corrected values of Eq. (3.4) as follows,

$$\sum_{j=1}^J (\rho_{i,j}^* Q_{i,j}^* + \rho'_{i,j} Q_{i,j}^* + \rho_{i,j}^* Q'_{i,j} + \rho'_{i,j} Q'_{i,j}) s_{i,j} = -d_i \quad (3.7)$$

The term  $\rho'_{i,j} Q'_{i,j}$  may be neglected as it approaches zero as the solution approaches convergence. Eq. (3.7) may then be rewritten as,

$$\sum_{j=1}^J (\rho_{i,j}^* Q_{i,j}^* + \rho'_{i,j} Q_{i,j}^* + \rho_{i,j}^* Q'_{i,j}) s_{i,j} = -d_i \quad (3.8)$$

Substituting Eq. (3.5). and Eq. (3.6). into Eq. (3.8). gives

$$P'_i = \frac{\sum_{j=1}^J (c_{i,j} P_{n,j}) + b_i}{c_{i,i}} \quad (3.9)$$

where,

$$\begin{aligned} c_{i,i} &= \sum_{j=1}^J \left[ \frac{\rho_{i,j}^*}{g_{i,j}^* f 1_{i,j}^*} + s_{i,j} H_{i,j} a_{i,j} \left( \frac{\rho_{i,j}^* f_{i,j}^* g 1_{i,j}^*}{g_{i,j}^* f 1_{i,j}^*} - |Q_{i,j}^*| \right) \right] \\ c_{i,j} &= \frac{\rho_{i,j}^*}{g_{i,j}^* f 1_{i,j}^*} - s_{i,j} H_{i,j} a_{i,j} \left( \frac{\rho_{i,j}^* f_{i,j}^* g 1_{i,j}^*}{g_{i,j}^* f 1_{i,j}^*} - |Q_{i,j}^*| \right) \\ b_i &= d_i + \sum_{j=1}^J (\rho_{i,j}^* Q_{i,j}^* s_{i,j}) \end{aligned}$$

Eq. (3.9) is solved simultaneously for all nodes in the network. Updated values for flow-rate, pressure and density are calculated from Eq. (3.4). The process is repeated until convergence is achieved.

The convergence criterion for the continuity equation is,

$$\varepsilon_m < \frac{|h_i|_{max}}{|\dot{m}|_{mean}} \quad (3.10)$$

where,

$$h_i = \sum_{j=1}^J (\rho_{i,j} Q_{i,j} s_{i,j}) + d_i$$

and for the pressure-drop equation,

$$\varepsilon_p < \sum_{e=1}^E \left| \frac{\Delta P_1 - \Delta P_2}{\Delta P_1} \right| \quad (3.11)$$

where ,

$\Delta P_1$  = pressure-drop across element from Eq. (3.2).

$\Delta P_2$  = pressure difference between two nodes associated with element

The stability of the iterative procedure requires that the term  $c_{ij}$  in Eq. (3.9) always be positive,

$$\frac{\rho_{i,j}^*}{g_{i,j}^* f 1_{i,j}^*} \geq a_{i,j} \left( |Q_{i,j}^*| - \frac{\rho_{i,j}^* f_{i,j}^* g 1_{i,j}^*}{g_{i,j}^* f 1_{i,j}^*} \right) \quad (3.12)$$

A general pressure-drop / flow-rate relationship has the form,

$$\Delta P = K \rho^\beta Q^\alpha \quad (3.13)$$

and the functional relationships become,

$$\begin{aligned} f &= KQ^\alpha & \text{and} & & f1 &= \alpha KQ^{\alpha-1} \\ g &= \rho^\beta & & & g1 &= \beta \rho^{\beta-1} \end{aligned} \quad (3.14)$$

Substituting Eq. (3.14) into Eq. (3.12) results in,

$$\rho_{i,j}^* \geq a_{i,j} K_{i,j} (\rho_{i,j}^*)^\beta (Q_{i,j}^*)^\alpha (\alpha - \beta) \quad (3.15)$$

Substituting Eq. (3.13) into Eq. (3.15) gives,

$$\frac{\Delta \rho_{i,j}^*}{\rho_{i,j}^*} \leq \frac{2}{\alpha - \beta} \quad (3.16)$$

where,

$$\Delta \rho_{i,j} = \frac{\Delta P_{i,j}}{RT_{i,j}}$$

The mean element density is given by,

$$\rho_{i,j}^* = \frac{\rho_i^* + \rho_{n_{i,j}}^*}{2} \quad (3.17)$$

and the difference in density is given by,

$$\Delta \rho_{i,j}^* = \rho_{n_{i,j}}^* - \rho_i^* \quad (3.18)$$

It follows from Eq. (3.16), Eq. (3.17) and Eq. (3.18) that stability will be guaranteed if  $(\alpha - \beta) \leq 1$  (Greyvenstein and Laurie, 1994). Most pressure-drop / flow-rate relationships meet this criterion.

As discussed in the previous section, Wood and Rayes (1981) found shortcomings in the node method. The reason for this is that solutions to the node equations do not enforce an exact continuity balance. This problem also occurs in the SIMPLE method when coefficients in the pressure correction equation differ significantly in different co-ordinate directions (Greyvenstein and Laurie, 1994). The problem is alleviated by obtaining a good solution to the pressure correction equation before continuing to the next iteration of the solution algorithm. The linearised continuity equation, Eq. (3.8), is exactly satisfied if Eq. (3.9) is exactly satisfied. Thus the reliability of the simultaneous node method is significantly improved by solving Eq. (3.9) exactly (Greyvenstein and Laurie, 1994). The envelope method (George and Liu, 1981) is used to solve Eq. (3.9) exactly.

There are essentially four phases to a sparse matrix storage scheme; ordering, storage allocation, factorisation, and triangular solution (George and Liu, 1981). Formally, the envelope method is identical to the Gaussian elimination method. In matrix form Eq. (3.9) may be written as,

$$MP' = b \quad (3.19)$$

with

$$\begin{aligned} m_{i,j} &= c_{i,j} \\ m_{i,n_{i,j}} &= -c_{i,j} \end{aligned}$$

The remaining elements of  $M$  are zero. Assuming  $M$  is symmetric and positive definite, i.e.  $m_{i,j} = m_{j,i}$ , and  $x^T M x > 0$  for all non-zero vectors  $x$ , respectively, Cholesky's method gives the triangular factorisation (George and Liu, 1981),

$$M = LL^T \quad (3.20)$$

where  $L$  and  $L^T$  are the lower and upper triangular matrices respectively.  $P'$  may be obtained in two stages by back substitution into the two triangular systems,

$$\begin{aligned} Lx &= b \\ L^T P' &= x \end{aligned} \tag{3.21}$$

Ideally, all quantities known in advance to be zero need not be computed. However, as George and Liu (1981) illustrated, the more zeros ignored in the computational scheme, the more complex the matrix structure becomes. A balance must be made between economical storage and solution computational overhead. The envelope method was selected to meet this requirement (Greyvenstein and Laurie, 1994).

All the leading zeros in a specific row of  $M$  are preserved in  $L$ . Hence only the elements between the first non-zero and the diagonal need be considered. Although zeroes may exist in this region they will not be ignored in the calculation.

A further refinement may be made by re-ordering the nodes in the network, to reduce the bandwidth (number of elements including zeros between first non-zero element and the diagonal). The method used here is the Reverse Cuthill-McKee re-ordering algorithm. In this way significant improvements are made on program storage and computation requirements.

The re-ordering algorithm may be simply described in three steps (Greyvenstein and Laurie, 1994):

1. Begin at any node in the network and find the node furthestmost from it. Repeat this from the new node, and continue repeating until the path length stops increasing. The last node found becomes the first node, and is numbered 'one'.
2. Visit the lowest numbered node and order all of its un-numbered neighbours in increasing order of the number of elements attached to each node, giving each the next available number. This is repeated until all nodes are re-numbered.
3. Reverse the ordering, so the last node is re-numbered 'one' and the first node becomes the last one.

Greyvenstein and Laurie (1994) illustrated a typical example where this re-ordering resulted in a reduction of over 50% in the number of elements in the lower triangular factor. In theory this method is mathematically identical to a standard Gaussian elimination, and hence Eq. (3.9) is solved exactly. The assumption was made that the matrix  $M$  was symmetric and positive definite. This is only rigorously satisfied if the terms including  $a_{i,j}$  are ignored in Eq. (3.9). However, these terms are typically relatively small compared to the other terms, and the assumption can be made that the accuracy is not significantly affected by the lack of symmetry.

The scheme was shown to be significantly faster in achieving convergence than other methods. Greyvenstein and Laurie (1994) demonstrated a solution in half the number of iterations when compared with the well known Newton-Raphson iterative technique. No convergence difficulties were observed over a wide range of sample problems.

### 3.3 Solution to the energy equation

The energy equation is satisfied by ensuring an enthalpy balance at each node within the network. This may be specified at nodes with branch elements containing mass transfer as,

$$T_i = \frac{\sum_{j=1}^J (E_{i,j} + \dot{m}_{i,j} Cp T_{n_{i,j}})_{\text{inflow elements}}}{\sum_{j=1}^J (\dot{m}_{i,j} Cp)_{\text{inflow elements}}} \quad (3.22)$$

where,

$$E = (\text{heat transfer to element}) - (\text{work done by element})$$

A semi-implicit formulation is used to compute node temperatures on boundaries or within walls, i.e. at nodes where the branch elements contain no mass flow. On the flow boundaries, where conduction, convection and radiation are present, this may be expressed as,

$$T_i = \frac{\left( \sum_{j=1}^J R_{i,j} T_{n_{i,j}} \right)_{\text{conduction}} + \left( \sum_{j=1}^J h_{i,j} T_{n_{i,j}} \right)_{\text{convection}} + Q_{\text{radiation}}}{\left( \sum_{j=1}^J R_{i,j} \right)_{\text{conduction}} + \left( \sum_{j=1}^J h_{i,j} \right)_{\text{convection}}} \quad (3.23)$$

where,

$h_{i,j}$  = convective heat transfer coefficient

$R_{i,j}$  = conductive heat transfer coefficient

$Q_{\text{radiation}}$  = heat flux

The form of Eq. (3.23) may be altered to expedite the convergence, depending on the formulation of the radiation component, as will be demonstrated in later chapters.



Within the solid where conduction is the only mode of heat transfer,

$$T_i = \frac{\left( \sum_{j=1}^J R_{i,j} T_{n_{i,j}} \right)_{conduction}}{\left( \sum_{j=1}^J R_{i,j} \right)_{conduction}} \quad (3.24)$$

The heat transfer coefficient terms in Eq. (3.23) are evaluated using semi-empirical correlations and data for the cooling types found in gas turbine combustors. The effect of film cooling has a significant effect on the wall temperatures, and must be modelled accurately. These formulations take the form of Nusselt number correlations, employing numerous experimental data. A wide range of cooling effects are modelled, including Z-rings, lipped-rings, slots, effusion patches and transply patches. Heat pick-up by the fluid moving though the flametube wall is computed, and is included as a source term in the governing energy equation. These features will be discussed in detail in later chapters.

The Gauss-Seidel iterative procedure is used to solve the enthalpy balance. This method has the advantage of being simple and efficient when applied to large systems of equations. The procedure consists of three simple steps (Anderson et al, 1984):

1. Initial guesses are made for all unknowns.
2. Each equation is solved for the unknown whose coefficient is the largest in magnitude, using the guessed initial values, or updated values on the iterations which follow.
3. The process is repeated using the computed values as the initial values, until the changes in the unknowns becomes very small, i.e. convergence.

If the system of equations, represented by  $u$ , are irreducible and,

$$\left| u_{i,i} \right| \geq \sum_{\substack{j=1 \\ j \neq i}}^n \left| u_{i,j} \right| \quad (3.25)$$

for all  $i$ , and if for at least one  $i$ ,

$$|u_{i,i}| > \sum_{\substack{j=1 \\ j \neq i}}^n |u_{i,j}| \quad (3.26)$$

then the Gauss-Seidel procedure will converge.

Successive over-relaxation is used to accelerate the solution convergence. This simply corrects the variable in the direction of convergence, and thus speeds it up. The procedure may be written as follows,

$$u_{i,j}^{new} = u_{i,j}^* + \omega(u_{i,j}^{old} - u_{i,j}^*) \quad (3.27)$$

The variable solved by the Gauss-Seidel iteration is thus updated through the use of the relaxation factor,  $\omega$ .

The solution of the flow and energy equations are fully coupled.

### 3.4 Network algorithm overall solution strategy

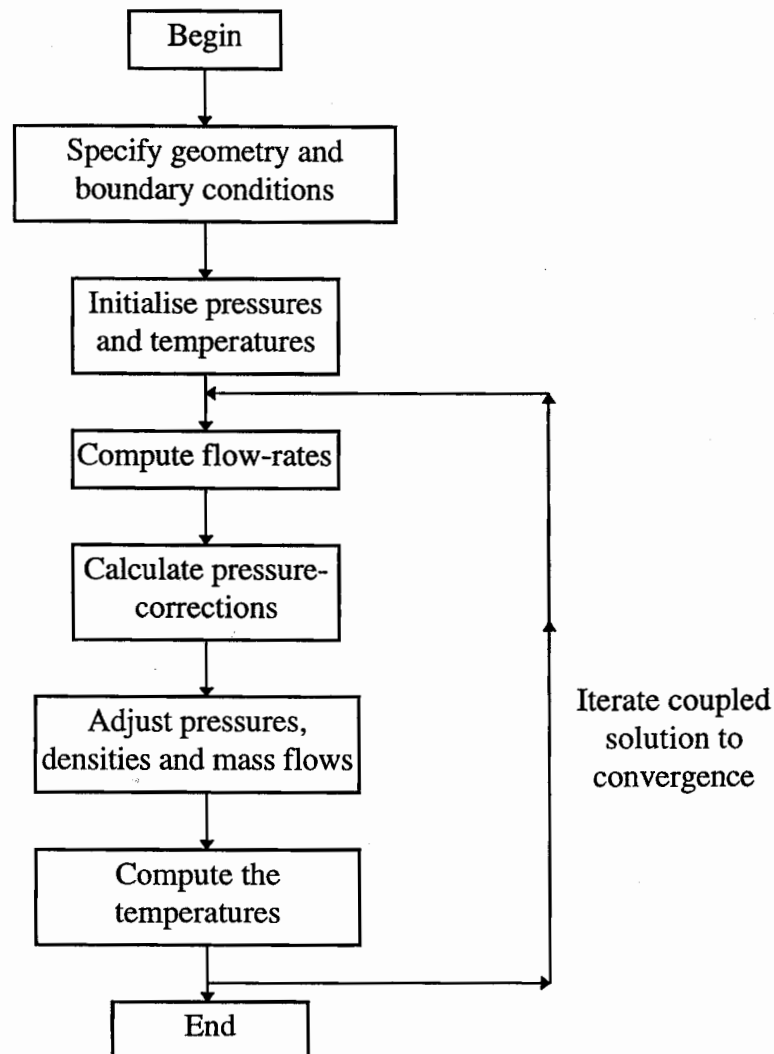


Figure 3.2 Overall flow structure of algorithm

Figure 3.2 above illustrates the overall strategy for solving the coupled flow and energy equation. Each step may be broken into a number of sub-sections, but the essence of the solver is as shown. The geometry specification takes the form of an input file requiring the definition of each of the elements to be used in the network. Initial pressures and temperatures are guessed, based upon the boundary conditions, and these values are used to compute mass flows. The pressure corrections are then solved, and the pressures,

densities and mass flows updated. To solve the flow equations this process is repeated until convergence. For a fully coupled solution strategy the energy equation is solved at the end of each flow loop, before iterating to the next loop. The number of separate iterations of both the flow and the energy equations may be specified to accelerate convergence. The equations may be loosely coupled without any significant loss in accuracy.

## 4. Combustor flow modelling

### 4.1 Introduction

The aerodynamic design is of vital importance to the performance of the gas turbine combustor. Although a wide variety of combustors have been developed in the past, they all have similar basic underlying features. The objective of the diffuser and annulus is to slow the air and distribute it to the combustion zones with a minimal amount of loss. Within the combustor flametube the goals are to achieve large scale recirculation in the primary zone to stabilise the flame, dilution of the products of combustion, and optimisation of the liner wall cooling requirement. Mixing processes are of prime importance, especially in the primary zone where the high burning rates are only possible with good mixing. The mixing of air with combustion products in the dilution region is essential to obtaining a satisfactory temperature distribution of the exhaust gases entering the turbine (Holdeman et al, 1988 and Oechsle and Mongia, 1993). Mixing is achieved only with penalties in pressure loss and combustor length, and an optimum must be found.

Assuming a given compressor delivery condition, the distribution of the air is governed by the geometry of the combustor. The liner wall features are responsible for admitting the correct proportions of air into the flametube to meet the overall design objectives. Thus the prediction of flow recirculation, jet penetration and mixing, mass flows, pressure-drop, and the discharge coefficients of the liner holes and cooling features is necessary.

Figure 4.1 illustrates the method used to achieve combustor flow modelling goals. The double annular combustor network illustrates all the key features required for the complete semi-empirical flow modelling of a combustor. The nomenclature is as in the previous chapter, i.e. the squares represent the elements describing the combustor

geometry, and the circles represent the nodes where the overall governing equations are solved.

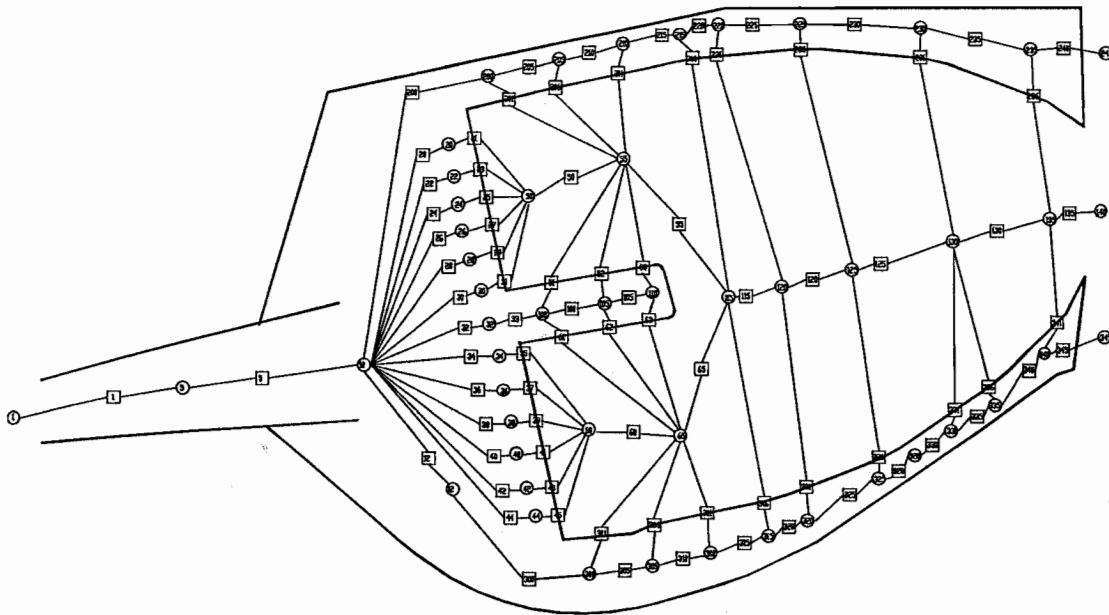


Figure 4.1. Double annular combustor network diagram

The elements contain the semi-empirical governing equations required to model the mass flow and pressure-drop through particular geometrical features. The elements which fall along the flametube liner wall represent holes, cooling features and atomisers or injectors. The elements within the flametube represent the sections of duct which make up the flametube. Likewise in the annulus the elements represent sections of duct combined to model the annuli geometry. The elements in the diffuser section account for the pressure losses associated with diffusers. Thus a relatively simple description of the combustor has been generated using a network.

The one-dimensional nature of the network solver does not allow the resolution of circumferential non-uniformities. However, the network model may be generated for any particular sector or slice of the combustor. Thus the algorithm may account for local liner feature effects. The importance of this facility is less crucial in the flow modelling

compared to the heat transfer modelling where local features may have a significant effect on the liner film cooling, e.g. the destruction of a cooling film by a primary port.

The purpose of this chapter is to address the issue of predicting the combustor mass flow distribution and pressure-drop. The sub-models required by the network solver to achieve these goals are presented, and their implementation described. Finally the accuracy of the models are evaluated on a number of combustor test cases of widely varying geometry.

## 4.2 Semi-empirical element governing equations

### 4.2.1 Duct with area change (DG)

The flow in the flametube and annuli are modelled using this element type. The inlet conditions and cross-sectional areas most significantly effect the computed element velocity. The flow in the annuli has a significant effect on the flow field within the flametube, and also the liner wall temperature distribution. Although the effectiveness of liner wall convective cooling is enhanced with increasing annulus velocities, the velocities are designed low to meet more critical requirements (Lefebvre, 1983), which include,

- liner holes in the same row pass a similar airflow
- higher hole discharge coefficients
- steeper jet penetration angles
- lower friction loss
- low expansion losses downstream of holes

Within the flametube the DG elements accumulate the effects of the discharge of the liner features, including frictional losses, and momentum addition.

The compressible flow total pressure-drop governing equations for ducts with area change is given by (Jeppson, 1977, Saad, 1985 and Shames, 1982),

$$\Delta P_0 = \frac{P_0}{P_s} \left( \frac{fL}{D_{hm}} + \sum K_s + K_M + \frac{\Delta T_0}{T_0} \right) \frac{1}{2} \rho V^2 \quad (4.1)$$

where,

$$K_M = \text{loss coefficient due to injected momentum} = \frac{2}{\dot{m}} \sum \dot{m}_i \left( 1 - \frac{V_i \cos \theta_i}{V} \right)$$

$$\sum K_s = \sum \frac{\Delta P_{0s}}{\frac{1}{2} \rho V^2} = \text{sum of secondary loss coefficients}$$

$$\Delta P_{0s} = \text{total pressure drop across secondary component}$$



$$f = \frac{0.25}{\left[ \log \left( \frac{e}{3.7 D_{Hm}} + \frac{5.74}{Re^{0.9}} \right) \right]^2} \quad (\text{for } 5 \times 10^3 < Re < 10^6)$$

$$f = \frac{64}{Re} \quad (\text{for } Re < 2300)$$

$Re$  = Reynolds number

$e$  = wall roughness

$P_o$  = mean total pressure in duct

$P_s$  = mean static pressure in duct

$L$  = duct length

$D_{Hm}$  = duct mean hydraulic diameter

$\rho$  = mean density

$V$  = mean velocity

$T_o$  = mean total temperature

The pressure rise due to momentum addition from the liner wall features to the mainstream flametube flow is normally of significance. The mechanism is illustrated in Figure 4.2.

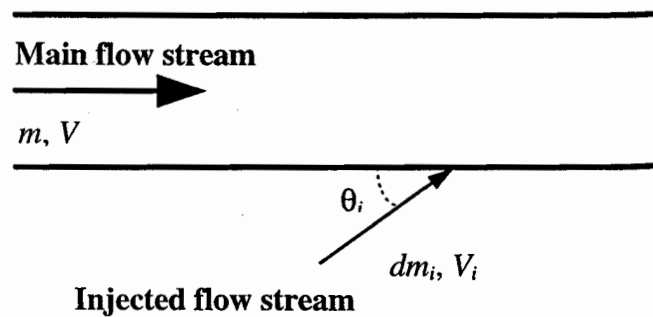


Figure 4.2. Illustration of mass flow momentum addition to a duct

#### 4.2.2 Restrictor with discharge coefficient (RD)

Restrictors may be used for modelling unusual combustor features for which the discharge coefficients are known. This may include the simplified representation of swirlers, atomisers, or baseplate features. The element has also proven useful in accounting for snouts and their associated geometry upstream of the combustor baseplate.

The compressible total pressure-drop relationship for restrictors with discharge coefficients is given by,

$$\Delta P_0 = P_{01} \left( 1 - \frac{P_s}{P_{01}} \right) \quad (4.2)$$

where,

$P_{01}$  = upstream total pressure

$P_s$  = static pressure in restrictor throat

The relationship between static pressure and upstream total pressure may be written as,

$$\frac{P_s}{P_{01}} = \left( 1 + \frac{\gamma - 1}{2} M^2 \right)^{\frac{-\gamma}{\gamma - 1}} \quad (4.3)$$

Therefore, the Mach number,  $M$ , may be given as,

$$M = \sqrt{\frac{2}{\gamma - 1} \left[ \left( 1 - \frac{\Delta P_0}{P_{01}} \right)^{\frac{1-\gamma}{\gamma}} - 1 \right]} \quad (4.4)$$

and the restrictor mass flow as,

$$\dot{m} = MA'P_{01}\sqrt{\frac{\gamma}{RT_{01}}}\left[1 + \frac{\gamma-1}{2}M^2\right]^{\frac{-(\gamma+1)}{2(\gamma-1)}} \quad (4.5)$$

where,

$A' = C_D A$  = effective throat area

$C_D$  = discharge coefficient

$A$  = physical throat area

### 4.2.3 Restrictor with loss coefficient (RL)

These elements are for similar applications as the RD elements discussed in the previous section. However, the information required by the element to account for pressure drop are feature contraction and loss coefficients.

The total pressure-drop equation for compressible flow in restrictors with loss coefficients is given by,

$$\Delta P_0 = C_L P_{01} \left(1 - \frac{P_s}{P_{01}}\right) \quad (4.6)$$

where,

$P_{01}$  = upstream total pressure

$P_s$  = static pressure in restrictor throat

$C_L$  = loss coefficient

Similarly to RD bits the Mach number may be written as,

$$M = \sqrt{\frac{2}{\gamma-1} \left[ \left(1 - \frac{\Delta P_0}{C_L P_{01}}\right)^{\frac{1-\gamma}{\gamma}} - 1 \right]} \quad (4.7)$$

and the mass flow, as

$$\dot{m} = MA'P_{01}\sqrt{\frac{\gamma}{RT_{01}}}\left[1 + \frac{\gamma-1}{2}M^2\right]^{\frac{-(\gamma+1)}{2(\gamma-1)}} \quad (4.8)$$

where,

$A' = C_c A$  = effective throat area

$C_c$  = contraction coefficient

$A$  = physical throat area

#### 4.2.4 Diffuser pressure drop with loss coefficient (PD)

The air delivered by the compressor to the combustor has a high axial velocity which must be significantly reduced (typically a reduction of approximately one third) to allow stable combustion. The diffuser is used to meet this requirement. Diffuser analysis is complicated by flow separation and large pressure gradients. A good review of diffuser design has been provided by Klein (1995). One-dimensional analysis relies on the specification of empirical loss coefficients. Particular diffusers have been well characterised to provide the pressure-drops required by the combustor, and the loss coefficients for these diffuser are typically available to the design engineer.

The purpose for designing this element type was for modelling combustor diffuser pressure-drops. The governing equation is,

$$\Delta P_0 = \alpha (P_{01} - P_{s1}) \quad (4.9)$$

where,

$\alpha$  = specified pressure loss factor

$P_{01}$  = upstream total pressure

$P_{s1}$  = upstream static pressure

The pressure-drop across the element is dependent solely on the upstream pressures and a user specified loss factor. The mass flow through the element is computed as the total mass flow through the downstream nodes.

In some cases the compressor delivery profiles may be highly non-uniform, which will have an effect on the properties of the air transported through the diffuser. The ability to account for pre-diffuser inlet total pressure and total temperature profiles has been included in the network solver, the objective being an analysis capable of simulating mass flows and pressure-drops in spatially non-uniform flows. The circumferentially averaged profiles may be either flat, radially dimensional, or radially non-dimensional.

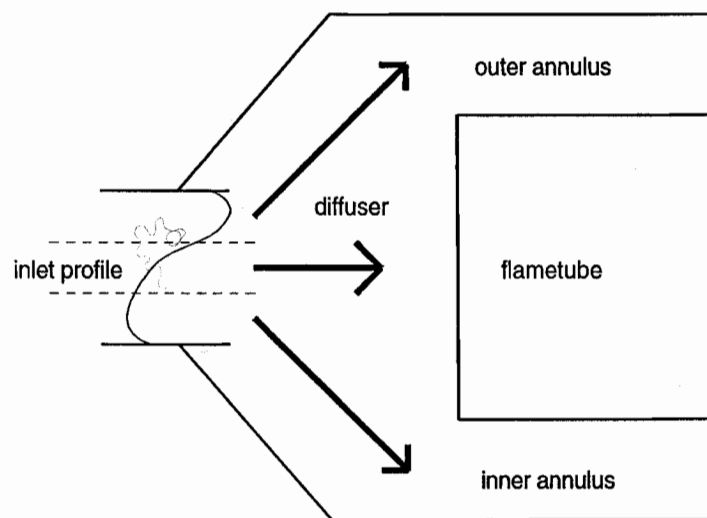


Figure 4.3 Illustration of compressor delivery profile calculation

Each PD element downstream of the pre-diffuser is influenced by the radial diffuser inlet profile. The influence of the profile is on the upstream total pressure,  $P_{01}$ , and upstream total temperature,  $T_{01}$ , of the PD element. The proportion of mass flow through downstream PD elements is proportional to the component of the radial profile feeding the PD element, as illustrated in Fig. 4.3. Hence if the mass flow through the PD element is known, the average upstream total pressure and temperature may be computed from the equivalent fraction of total diffuser inlet profile. This average value is computed by

integrating along the profile using the trapezoidal method (Schwarz, 1989) between the ranges (duct heights) of interest.

Since the mass flow in the PD element is computed from a summation of mass flows in its downstream neighbours, the process is iterative, and will have a slight detrimental effect on the rate of convergence of the network solver.

The PD element pressure loss is computed using the new upstream total and static pressures obtained from the diffuser inlet profile,

$$\Delta P_0 = \alpha (P_{01_{new}} - P_{s1}) \quad (4.10)$$

The temperature fluctuation in the diffuser inlet profile is accounted for by computing a new average upstream temperature based on the proportion of mass flow in the PD bit concerned. The new profile temperature is compared to the old mean diffuser inlet temperature to obtain an enthalpy change across the PD bit.

$$H = \dot{m} C_p (T_{01_{new}} - T_{01_{old}}) \quad (4.11)$$

This enthalpy change appears as a source term in the overall governing energy equation, giving a new PD element exit temperature corrected for the effect of the upstream temperature profile.

#### 4.2.5 Ports and Cooling/Dilution holes (HO)

The liner wall features meter the air required for the critical processes of combustion and film cooling within the combustor flametube. Flow through liner holes is not just a function of the size and pressure-drop across them. The annulus geometry and the flow

conditions near the hole influence the effective flow area. The compressible flow governing relationship for cooling/dilution holes is given by,

$$\Delta P = P_{01} \left( 1 - \frac{P_s}{P_{01}} \right) \quad (4.12)$$

where,

$P_{01}$  = upstream total pressure

$P_s$  = static pressure in orifice throat

Two options exist for specifying the pressure drop:

Option A:  $\Delta P_0 = \Delta P_A = P_{01} - P_{s2}$

Option B:  $\Delta P_0 = \Delta P_B = P_{s1} - P_{s2}$

Assuming the downstream static pressure is equal to the downstream total pressure,

$$\begin{aligned} \Delta P_0 &= P_{01} - P_{02} \\ &= \Delta P_A \\ &= \Delta P_B - (P_{s1} - P_{01}) \end{aligned}$$

hence,

$$\Delta P_0 = P_{01} \left( 1 - \frac{P_s}{P_{01}} \right) + I \quad (4.13)$$

where,

$$I = 0 \quad (\text{Option .A.})$$

$$I = P_{01} \left( 1 - \frac{P_{s1}}{P_{01}} \right) \quad (\text{Option .B.})$$

Now, two additional options may be included,

Option C:  $\Delta P_0 = \Delta P_A = P_{01} - P_{s2}$

Option D:  $\Delta P_0 = \Delta P_B = P_{s1} - P_{s2}$

but, no assumptions are made concerning the downstream static pressure. The new values of  $I$  in Eq. (4.13) are,

$$I = P_{02} \left( \frac{P_{s2}}{P_{02}} - 1 \right) \quad (\text{Option .C.})$$

$$I = P_{01} \left( 1 - \frac{P_{s1}}{P_{01}} \right) + P_{02} \left( \frac{P_{s2}}{P_{02}} - 1 \right) \quad (\text{Option .D.})$$

In the above equation,

$$\frac{P_{s1}}{P_{01}} = \left( 1 + \frac{\gamma - 1}{2} M_1^2 \right)^{\frac{-\gamma}{\gamma - 1}} \quad (4.14)$$

$$\frac{P_{s2}}{P_{01}} = \left( 1 + \frac{\gamma - 1}{2} M_2^2 \right)^{\frac{-\gamma}{\gamma - 1}} \quad (4.15)$$

where,

$M_1$  = cross - stream Mach number at orifice inlet

$M_2$  = cross - stream Mach number at orifice outlet

and,

$$\frac{P_s}{P_{01}} = \left( 1 + \frac{\gamma - 1}{2} M^2 \right)^{\frac{-\gamma}{\gamma - 1}} \quad (4.16)$$

where,

$M$  = Mach number at orifice throat

The Mach number in the orifice throat may therefore be written as,



$$M = \sqrt{\frac{2}{\gamma - 1} \left[ \left( 1 - \frac{\Delta P_0 - I}{P_{01}} \right)^{\frac{1-\gamma}{\gamma}} - 1 \right]} \quad (4.17)$$

and,

$$\dot{m} = MA'P_{01} \sqrt{\frac{\gamma}{RT_{01}}} \left[ 1 + \frac{\gamma - 1}{2} M^2 \right]^{\frac{-(\gamma+1)}{2(\gamma-1)}} \quad (4.18)$$

where,

$A' = C_D A$  = effective throat area

$C_D$  = discharge coefficient

$A$  = physical throat area

The discharge coefficient varies with hole geometry and flow conditions. The discussion which follows describes the various options available for calculating discharge coefficients within the combustor.

A significant amount of work has been performed to correlate the discharge coefficient of liner wall features. Many of the correlations have been derived by gas turbine engine manufacturers to aid in the design process. A number of the correlations included for liner feature discharge represent 'in house data', and are not publicly available. Nevertheless, a number of correlations are presented here which may be found in the open literature.

The coefficient of discharge of liner holes is influenced by several phenomena (Lefebvre, 1983):

- type (plain, plunged, etc.)
- shape (circular, rectangular, etc.)
- ratio of hole spacing to annulus height
- liner pressure-drop

- distribution of static pressure around the hole inside the liner
- presence of swirl in the upstream flow
- local annulus air velocity

Kaddah (1964) performed a detailed analysis on the flow through a liner wall and found the coefficient of discharge for plain circular, oval and rectangular holes in an incompressible non-swirling flow to be,

$$C_D = \frac{1.25(K-1)}{[4K^2 - K(2-\alpha)^2]^{0.5}} \quad (4.19)$$

Freemen (1965) performed a similar analysis to obtain the discharge coefficient for plunged holes,

$$C_D = \frac{1.65(K-1)}{[4K^2 - K(2-\alpha)^2]^{0.5}} \quad (4.20)$$

Adkins and Gueroui (1986) performed a detail theoretical and experimental analysis on the flow through plane circular holes in a cross-stream, and included the effect of annulus curvature. The coefficient of discharge was found to be,

$$C_D = f \sqrt{C_{fc}^2 - 1 + \phi} \quad (4.21)$$

where,

$$f = \frac{\text{circumferential surface area}}{\text{circular plan area}}$$

$$C_{fc} = \left[ 1 - \exp(-1) + \exp\left(-\frac{1}{\sqrt{1-\phi}}\right) \right] \left[ 1 - \frac{\phi(1-\phi)}{3} \right]$$

$$\phi = \frac{p_a - p_c}{P_a - p_c}$$

$p_a$  and  $P_a$  = upstream annulus static and total pressure, respectively

$p_c$  = downstream flametube static pressure

The semi-empirical equations used to compute the discharge through holes may be combined to compute the effects of a number of liner wall features, such as, effusion patches, Z-rings, static fed lipped cooling rings, total fed lipped cooling rings, and total-static fed lipped cooling rings. Two examples of the network requirement for the latter are shown in Fig. 4.4 and Fig. 4.5 below.

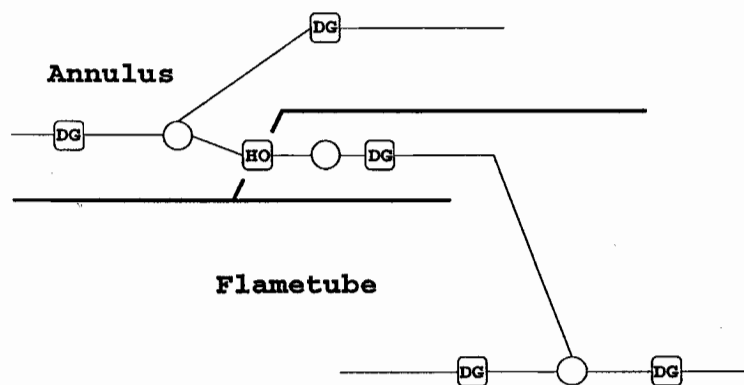


Figure 4.4. Total-fed lipped cooling ring

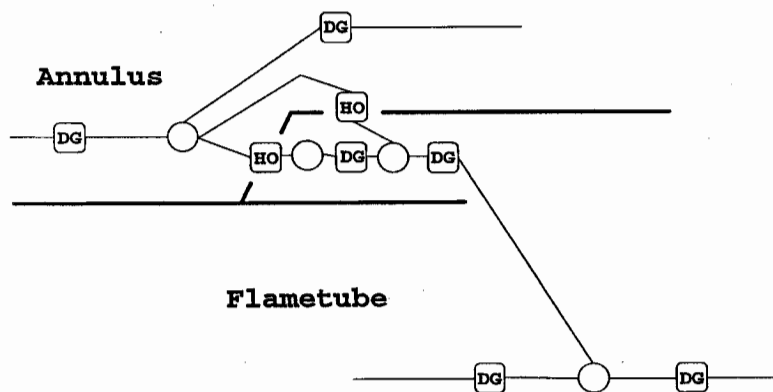


Figure 4.5. Total-static-fed lipped cooling ring

#### 4.2.6 Radial pressure gradient

In straight ducts there is no significant pressure gradient perpendicular to the direction of the flow. However, for curved ducts these pressure gradients become significant. Since the discharge from liner wall features is dependent upon the pressure-drop across the liner, pressure effects must be taken into account. An example of such a geometry is a reverse flow combustor where the flametube turns through 180 degrees. To take into account this difference between the inner and outer arc pressures in a curved duct the following formula is used, for radial pressure difference from the centre of the duct,

$$\Delta P = \frac{H}{2} \frac{\rho V^2}{R} \quad (4.22)$$

where,

$H$  = width of duct

$V$  = mean velocity

$R$  = radius of curvature from the centre of the duct

### **4.3 *Constrained equilibrium combustion computation***

Simulating the combustion within a gas turbine combustor presents a formidable task. Combustion involves detailed multiphase reaction kinetics, heat loss, turbulence interaction and evaporation. The problem is further complicated by the complexity of common fuels, such as kerosene, for which a detailed reaction scheme has yet to be derived. Combustion simulations rely on the use of simplifying models to provide a representation of the combustion processes.

Time dependent single or multi-step reaction kinetics are typically used for CFD calculations including combustion. The eddy break-up model relates the dissipation of eddies to the fluctuation in concentrations (Spalding, 1971) or mean concentrations (Magnussen and Hjertager, 1976) of intermittent reactants. Bilger (1976) developed a laminar flamelet approach by relating the mean reaction rate to the scalar dissipation rate. The concentrations and other chemistry dependent scalars are related to the mixture fraction, and the turbulence interaction is included by integrating the scalar functions of mixture fraction across a probability density function of mixture fraction. A more detailed description of these two popular methods is provided by Bressloff (1996).

Chemical equilibrium models are a popular, simpler alternative method to providing flame temperatures in both three-dimensional CFD calculations and more simple one-dimensional calculations where the detailed three-dimensional components of the flow are not available. The equilibrium computation calculates adiabatic flame temperatures based upon local species concentrations, and accounts for the dissociation of major species. The equilibrium model used in this work is based upon the algorithm developed by Gordon and McBride (1971). The fuel properties information required for the calculation is read into the code prior to the main calculation. During the main solution procedure the temperature calculation is performed within DG elements where the combustion occurs.

The equilibrium model uses the local fuel fraction to compute the species concentrations and hence the adiabatic flame temperature. The fuel fractions are computed within each node, by performing a summation of the air mass fraction, and input to the equilibrium procedure to provide an adiabatic flame temperature for the element. The fuel fraction in an element is given by,

$$ff = \frac{\text{mass flow of fuel}}{\text{mass flow of fuel} + \text{mass flow of air}} \quad (4.23)$$

and, the air mass fraction is,

$$\psi = 1 - ff \quad (4.24)$$

Then using the notation shown in Fig. 3.1 the fuel fraction at each node may be computed from,

$$ff_i = 1 - \frac{\sum_{j=1}^J (\dot{m}_{e,i,j} \psi_{n_{i,j}})_{\text{inflow elements}}}{\sum_{j=1}^J (\dot{m}_{e,i,j})_{\text{inflow elements}}} \quad (4.25)$$

The Gauss-Seidel iteration, as described in chapter 3, is used to solve for the fuel fraction in the entire network. The fuel fraction is dependent upon the mixing and recirculation of air from the liner features, into the flametube. This process is accounted for by using a series of mixing and recirculation rules, as described in the following section, to compute a more realistic local fuel fraction.

Chemical species do not always attain full equilibrium in practical combustion systems. The gas temperature is highly affected should the fuel/air mixture reach a partial or constrained equilibrium state. The equilibrium model used here requires the CO and CO<sub>2</sub> concentrations to be calculated and constrained. The equilibrium model uses these

constraints with the predicted fuel fraction to compute other species concentrations, and hence flame temperature. In order to calculate these constraints an efficiency curve must be fitted to the flametube centreline. The empirical efficiency curve is different for each combustor type and must be specified unless an unconstrained equilibrium calculation will suffice. The efficiency curve is derived from empirical data to include the effects of mixing and heat loss in the computed flame temperature.

The thermodynamic properties of a chemical system may be computed if the chemical equilibrium composition can be found. Two equivalent formulations for describing the chemical equilibrium are the use of equilibrium constants and the minimisation of free energy, the minimisation of free energy being the least restrictive of the two formulations (Gordon and McBride, 1971).

The equilibrium point of a system occurs where a combusting fuel/air mixture decomposes into a mixture of chemical species at a specific temperature. The composition of this equilibrium mixture may be described by a minimisation of free energy formulation. Gibbs free energy is given by (Gordon and McBride, 1971),

$$g = \sum_{j=1}^n \mu_j n_j \quad (4.26)$$

where,

$$\mu_j = \text{chemical potential of species } j = \left( \frac{\partial g}{\partial n_j} \right)_{T, P, n_{i \neq j}}$$

$n_j$  = concentration of species  $j$

The minimisation of free energy is subject to the following constraint,

$$b_i^o - b_i = 0 \quad i = 1, 2, \dots, l \quad (4.27)$$

where,

$b_i^o$  = assigned number of kilogram - atoms of element  $i$  per kilogram - mole species  $j$

$$b_i = \sum_{j=1}^n a_{ij} n_j \quad i = 1, 2, \dots, l$$

$a_{ij}$  = number of kilogram - atoms of element  $i$  in species  $j$

$l$  = number of elements

$n$  = number of species

A full discussion of the solution of these equations is provided by Gordon and McBride (1971).

The constrained equilibrium may be accounted for by specifying the final concentrations of certain species, such as CO and CO<sub>2</sub>, by setting it as an extra element  $b_i$ , thereby increasing the number of constraints that the calculation is subject to by one per constrained species.



## 4.4 Mixing and recirculation models

The accuracy of the constrained equilibrium calculation is a strong function of local fuel/air ratio. The location and characteristics of the liner features determine this ratio. Typically, flow entering the flametube through the liner does not immediately mix into the combusting gases and burn. Depending upon the geometry of the feature the annulus air may mix into the flow downstream or upstream of the feature. This effect will strongly influence the adiabatic flame temperature.

A number of mixing and recirculation rules have been developed to describe the rate at which feature flows combine with the mainstream flametube flow, and may be described as follows:

- *Baseplate features*: all air added directly to the front end of the flametube
- *Primary holes*: a specified proportion of the flow recirculates to the front end of the flametube, and the remaining mass flow is linearly added, a specified number of hole diameters, downstream from the hole centreline
- *All other holes*: flow is added linearly, a specified number of hole diameters, downstream from the feature centreline (see Fig. 4.6, the rectangular sections labelled 'bits' refer to a series of DG elements)

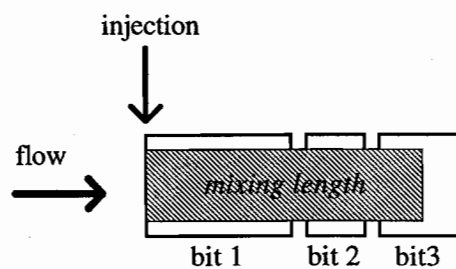


Figure 4.6. Hole/cooling ring/impingement flow mixing

- *Cooling rings and Impingement outlet devices*: flow is added linearly from the feature centreline up to a specified number of slot heights, or feature depths, downstream
- *Effusion and Transpiration patches*: flow is added linearly from the upstream edge of the patch to the downstream edge of the patch (see Fig. 4.7)

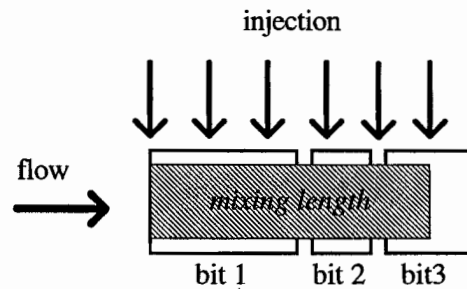


Figure 4.7. Effusion and transpiration flow mixing

- *Reverse flow cooling rings*: flow is added linearly a specified number of slot heights upstream of the feature centreline to a maximum at the feature centreline (see Fig. 4.8)

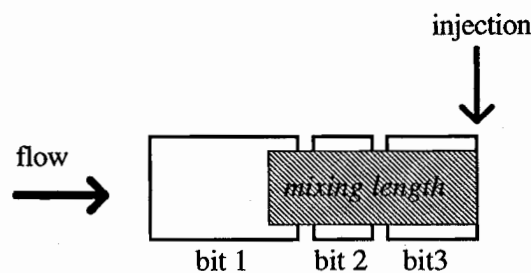


Figure 4.8. Reverse flow cooling ring mixing

Although these rules are crude, they allow a more realistic attempt to resolve the local fuel/air ratio. A mixed mass flow may be computed at any axial location, in any combustion stream, influenced by any number of liner wall flow features connected to the combustion stream within the combustor.

## 4.5 Real gas property models

The change in temperature, pressure and species within a combustor results in a significant variation in the fluid properties. A series of properties routines have been incorporated to account for these effects within systems containing air and products of combustion. The dynamic viscosity, thermal conductivity, and specific heat are calculated using polynomial fits and interpolation.

Sutherland's formula for the viscosity of air is used at low temperatures (Anderson et al, 1984),

$$\mu = 1.458 \times 10^{-6} \frac{T^{1.5}}{T + 110.4} \quad (4.28)$$

At higher temperatures (400K-2200K) air viscosity is calculated using a polynomial curve fit (ESDU, 1973). Tables of data have been generated for the variation of dynamic viscosity with temperature and fuel/air ratio for use in combustion systems (Poferl et al, 1969 and Poferl and Svehla, 1973). Polynomial curve fits to this data are used in this work.

The thermal conductivity of air at temperatures below 1000K is calculated using a polynomial fit obtained from ESDU data (ESDU, 1978). At higher temperatures curve fits generated from the data of Poferl et al (1969) and Poferl and Svehla (1973) are used. Data presented by the same authors is used to generate polynomial fits for the variation of thermal conductivity of the products of combustion with temperature and fuel/air ratio.

Specific heat at constant pressure,  $C_p$ , is computed in the same way, using polynomial fits. However, when the equilibrium calculation is used to obtain flame temperatures, the

specific heat is calculated from the concentration of the individual species in the combustion products.

The ratio of the specific heats is calculated using a constant value for the real gas constant,

$$\gamma = \frac{C_p}{C_p - R} \quad (4.29)$$

The Prandtl number is calculated from,

$$Pr = \frac{C_p \mu}{k} \quad (4.30)$$

## **4.6 Combustor case studies**

The validation of the mass flow and pressure distribution using the network solver was undertaken using comparisons to proven numerical and experimental data. Three significantly different combustors with annular geometries were evaluated using the network algorithm and the results compared with those from a proven one-dimensional combustor design code, CODAS (Lowe, 1995). A reverse flow geometry was also modelled and the results compared to experimental and analytical predictions. Comparisons could not be made with the proven one-dimensional design code in this instance as it was unable to simulate the more complex reverse flow geometry.

### **4.6.1 Isothermal Annular Combustor .1.**

#### **4.6.1.1 Network specification**

A not to scale network diagram for the first annular combustor modelled is shown in Fig. 4.9. The airspray combustor was modelled at take off condition (compressor delivery pressure of 16 bar and temperature 855K). All the baseplate holes had specified discharge coefficients. A Z-ring immediately downstream of the baseplate on the inner and outer liner was used to generate a cooling film, which was maintained all the way down the liner by a series of angled effusion patches. Primary and dilution ports were responsible for controlling and sustaining the combustion. The snout loss, and inner and outer dump losses were modelled with the PD element. The medium dashed line shows the logic link used for this calculation. The losses in these sections may have a specified dependency on the pre-diffuser inlet or exit total pressure, hence the requirement for the logic link to define the inlet pressure to be used by the element governing equation. The short dashed lines signify the logic links required for calculating the discharge coefficients, since Mach numbers and sometimes pressures are required from

surrounding elements in the network. Momentum addition is included for all holes in the flametube, as specified by the long dashed lines in the network. For holes simply discharging into the flametube, at no specific angle, the injection angle is calculated and used in the momentum addition calculation. Various bleeds in the annuli and dump diffuser region are accounted for by specifying mass sinks at the node situated in that region of the network.

#### **4.6.1.2 Discussion**

The following table (Table 4.1) summarises the overall results obtained from the isothermal annular combustor run.

	<b>CODAS</b>	<b>Network</b>
<b>Outer dump loss</b>	2.962%	2.963%
<b>Inner dump loss</b>	2.693%	2.693%
<b>Outer annulus head (fraction of inlet)</b>	0.306	0.306
<b>Inner annulus head (fraction of inlet)</b>	0.257	0.257
<b>Baseplate head (fraction of inlet)</b>	0.367	0.367
<b>Flametube exit head (fraction of inlet)</b>	0.808	0.808
<b>Overall combustor pressure loss</b>	5.192%	5.236%

Table 4.1. Isothermal Annular combustor .1. pressure and mass flow splits

The table clearly shows the close tie-up between the CODAS and network solution. The PD element accurately predicts the dump diffuser losses and associated flows in the snout and inner and outer annuli. The flametube exit head mass flows illustrate the convergence in the CODAS solution. Since the network solver conserves mass, the mass

flow represents the actual mass flow leaving the flametube, while the CODAS value represents the converged flow solution, and so too the error in the numerical solution. The percentage overall combustor pressure losses, obtained as the ratio of flametube exit total pressure to pre-diffuser inlet total pressure were in close agreement.

Figure 4.11 compares the flametube axial mass flows as predicted by CODAS and the network solver. The network predicted mass flow plotted was the value located at the centre of the DG elements within the flametube. The two profiles compared closely, and the slight differences between the curves was due only to the specific location at which the two codes added the hole mass flow into the flametube. This would obviously be dependent upon the location of the elements in the network solver or the control volumes in CODAS. The proof of this statement is shown in the comparison of mass flow splits in the inner and outer annuli (see Fig. 4.11). Since the location of the holes modelled in CODAS was exactly known, the flow splits at those precise locations could be compared. The almost exact comparison between the mass flows in the annuli show that the mass flows entering the flametube in CODAS and the network solver are almost identical. This corresponds to the similar discharge coefficients for the flametube holes, obtained using the two codes. The discharge coefficients never differed by more than 1%.

The total pressures are illustrated in Fig. 4.12. The graph showed a close similarity between the two results. The maximum difference in the predicted pressures was 0.09%. The characteristic shape of the curve also compared closely, i.e. a gradually increasing total pressure initially, followed by decreasing values as the flametube exit was approached. The static pressures shown in Fig. 4.13 corresponded in a similar way to the total pressures, the maximum difference being 0.10%. Following a slight rise downstream of the baseplate, the values decreased towards the flametube exit.

## **4.6.2 Isothermal Annular Combustor .2.**

### **4.6.2.1 Network specification**

The second annular combustor modelled is shown in Fig. 4.14. The geometry and operating conditions of this airspray combustor were significantly different from the previous case study. Isothermal Annular Combustor .2. was analysed at take-off conditions (compressor delivery pressure of 43 bar and temperature of 890K). Unlike the first case the combustor does not have a snout. Instead each baseplate feature is fed by a pressure loss from the pre-diffuser exit. This, as well as the annuli losses were modelled using the PD element. The discharge coefficients for the baseplate features were all specified by the user. The flametube features consisted entirely of holes, which required only the simple application of the HO elements to determine the discharge coefficients. Momentum addition from the flametube holes was included in the same way as for the first isothermal annular combustor.

### **4.6.2.2 Discussion**

The overall flow and pressure splits are illustrated in Table 4.2. The inner and outer annuli dump diffuser pressure losses and mass flows compared closely as for the first annular combustor test case. The flametube exit mass flows differed slightly. The network prediction of 0.850 of the total mass flow delivered by the compressor corresponds to the actual mass flow leaving the flametube, as required by the conservation of mass. The CODAS converged solution therefore represents a mass conservation error of 1.6%. The overall combustor pressure losses were in close agreement.



	<b>CODAS</b>	<b>Network</b>
<b>Outer dump loss</b>	3.130%	3.130%
<b>Inner dump loss</b>	2.916%	2.916%
<b>Outer annulus head (fraction of inlet)</b>	0.177	0.177
<b>Inner annulus head (fraction of inlet)</b>	0.261	0.260
<b>Baseplate head (fraction of inlet)</b>	0.558	0.560
<b>Flametube exit head (fraction of inlet)</b>	0.836	0.850
<b>Overall % loss</b>	6.723%	6.770%

Table 4.2. Isothermal Annular combustor .2. pressure and mass flow splits

Figure 4.15 presents the flametube axial mass flow profiles computed by CODAS and the network solver. The network prediction of mass flow appears uniformly higher than the CODAS result except in the baseplate region. The difference in the mass flow at the exit refers to the mass error in CODAS discussed above. Figure 4.16 shows the mass flow in the annuli. These results compared closely. The difference in the mass flow axial profile in the flametube therefore appears to be a product of the lack of convergence within the flametube of the CODAS solution.

The total and static pressure comparisons are shown in Fig. 4.17 and Fig. 4.18, respectively. The trends were similar to those reported for Isothermal Annular Combustor .1. The maximum difference in the total pressure profile was 0.80%, and for the static pressure, the difference was no greater than 0.12%.

### **4.6.3 Isothermal Annular Combustor .3.**

#### **4.6.3.1 Network specification**

The network set-up for the third annular combustor case study is shown in Fig. 4.19. The airspray combustor was modelled at standard take-off conditions (compressor delivery pressure of 34 bar and temperature of 865K). This combustor included both snout and baseplate loss factors. The holes in the baseplate all required modelling, apart from the burner. The flametube walls included primary and dilution ports, effusion, Z-rings, static fed cooling rings, and static-total fed cooling rings. The small slots making up the cooling ring were modelled using DG elements, as shown by the series of elements adjacent to liner wall features in Fig 4.19. Momentum addition was included from the flametube wall flows. The isothermal flow solution was obtained for a number of variations in network set-up, all modelling the same geometry. Two of these solutions are presented below, the first includes the modelling of cooling slots, and the second ignores slot effects.

#### **4.6.3.2 Discussion**

The overall flow and pressure splits are illustrated in Table 4.3. The pressure losses in the dump region compared favourably, and the mass flow splits differed by less than 0.2%. The overall pressure losses differed by 0.16% and 0.40% for the flow without and with cooling slots, respectively. The flexibility of the network solver allows the same combustor to be modelled in slightly different ways, these modifications may reduce or increase the differences between the network results and those of CODAS. The mass flow splits and pressure losses were effected by modifying the flametube wall exit slot areas, since the momentum addition coefficient is dependent upon the ratio of slot and flametube velocities.

	CODAS	Network Without slots	Network With slots
<b>Outer dump loss</b>	3.398%	3.398%	3.398%
<b>Inner dump loss</b>	1.361%	1.361%	1.361%
<b>Outer annulus head (fraction of inlet)</b>	0.254	0.254	0.255
<b>Inner annulus head (fraction of inlet)</b>	0.487	0.486	0.487
<b>Baseplate head (fraction of inlet)</b>	0.259	0.260	0.259
<b>Flametube exit head (fraction of inlet)</b>	0.904	0.904	0.904
<b>Overall % loss</b>	5.191%	5.350%	5.591%

Table 4.3. Isothermal Annular combustor .3. pressure and mass flow splits

The first case discussed includes the effect of cooling ring slots in the network predictions. Unfortunately, the CODAS model could not directly simulate the effects of cooling slots. Figure 4.20 shows the flametube axial mass flow profile. The difference between the network predictions and CODAS results are as described before, due to the different locations taken for mass flow addition. Figure 4.21 illustrates the close tie-up in the annuli flow-splits. The flow-splits in the upstream region show the most significant difference. However, the discharge coefficients never differed by more than 3%, and typically compared within 1%.

The total pressure and static pressure profiles with the wall slots included are presented in Fig. 4.22 and Fig. 4.23. The most significant difference in pressures occurred at the flametube exit, where the difference was as high as 0.4%. This difference was attributed to the method used in modelling the slots, and the method of momentum addition used by the two codes. When slots are included there were additional pressure losses associated with each slot. The slot exit areas were significantly larger than the combined hole exit areas feeding the slots, hence including slots results in both a reduction of the momentum addition and also total pressure rise within the flametube. The latter effect is

clearly illustrated in Fig. 4.22. where although the agreement is still close, the pressure rise down the flametube in the CODAS case is noticeably higher than that in the network case.

The network prediction was repeated, but the cooling slots were simply treated as holes in the flametube walls, discharging directly into the flametube. Figure 4.24 and Fig. 4.25 show the flametube and annuli axial mass flow profiles, respectively. The agreement with CODAS was once again very close.

The total and static flametube pressures are shown in Fig. 4.26 and Fig. 4.27, respectively. The pressure-rise in this case was more similar to the CODAS result, with the exit total pressures differing by 0.16%. This clearly illustrated the effect of exit hole/slot areas on the momentum addition coefficient, effecting overall pressure rise. The smaller the hole/slot exit area the greater the discharging velocity, and hence the higher the pressure rise.

## **4.6.4 Reverse Flow Combustor**

### **4.6.4.1 *Network specification***

The reverse flow combustor network set-up is shown in Fig. 4.28. The vaporiser combustor was modelled at the standard take-off condition (compressor delivery pressure of 7 bar and temperature of 720K). The same criteria applied to the network model of this combustor, as those for the previously modelled annular combustors. The diffuser section was modelled with PD elements. Various leaks through the flametube walls were modelled with RD elements, and added to the flametube mass flow. Liner features included primary and dilution ports for controlling and sustaining combustion. Liner cooling was achieved through a series of static-fed cooling rings (both forward and reverse flowing), angled effusion patches, impingement cooling, and Z-rings. The effects

of momentum addition and radial pressure gradient were incorporated within the network model.

#### **4.6.4.2 Discussion**

The CODAS computation is unable to model reverse flow combustor geometries. The network results were compared with experimental and analytical data (Gardiner, 1995). The data was based on measured pressure drops and basic thermodynamics calculations.

The overall combustor pressure drop computed by the network was 3.13%, which compared favourably with the measured pressure loss of 3.23%. Table 4.4 compares the flametube feature flow splits predicted using the network solver, and those obtained using a combination of pressure-drop measurements and analytical calculations to obtain the mass flow. The tabulated values were normalised by the compressor delivery mass flow. The stations refer to the elements depicted in Fig. 4.28.

The flow splits presented in Table 4.4. show a good comparison, considering the assumptions made in the analytical/experimental calculations were unknown. The main primary and dilution port flows agreed within 4%. Generally the results agreed within  $\pm 5\%$ . The worst agreement, 14%, was for the Z-ring, 106. The discharge coefficient used in the network prediction was simply a specified value for a general Z-ring, not necessarily the value used in the experimental/analytical computation.

Figure 4.29, Fig. 4.30, and Fig. 4.31 show the flametube path results, from the baseplate to the flametube exit obtained using the network solver. The flametube static pressure loss was noticeably higher than on the annular combustors. The flametube curvature and change in cross-sectional area combined to produce the static pressure loss.

Feature element number	Experimental/calculated mass flow	Network mass flow
11	0.068	0.072
16	0.370	0.379
21	0.166	0.170
26	0.073	0.072
31	0.166	0.172
36	0.117	0.114
46	0.164	0.154
56	0.123	0.114
61 + 71	0.106	0.109
66	0.334	0.319
76	0.081	0.080
81	0.063	0.068
87 + 88 + 89 + 505	0.061	0.062
106	0.051	0.059
111	0.036	0.036

Table 4.4. Comparison of feature calculated flows for the reverse flow combustor

This case study required no more computational effort than the previous three annular combustors modelled, and illustrated the versatility of the network solver.

## **4.7 Conclusions**

An aerodynamic gas turbine combustor modelling procedure has been developed. The methodology was unrestricted by combustor geometry and included all the components necessary for a complete flow analysis of a combustor. Duct sections formed an accurate representation of the flametube and annuli. Pressure drop elements successfully accounted for the effect of different diffuser geometries. Liner wall features were modelled using a number of correlations for ports, holes, cooling rings, effusion patches, and transply. Momentum addition and radial pressure gradient effects were accounted for in the solution procedure.

A constrained equilibrium calculation was incorporated into the network solver to compute local adiabatic flame temperatures. Mixing and recirculation models were used to provide the equilibrium calculation with corrected local fuel/air ratios. A real gas properties model was included to account for the effects of changes in pressure, temperature and composition on the combustion system gases. The inclusion of a combustion model in the algorithm allowed for a realistic fully coupled solution procedure.

Comparisons to a proven airflow analysis code and experimental results have illustrated the ability of the network solver to accurately predict mass flow splits and pressure-drops within a combustor.

The versatility of the network approach was demonstrated by analysing three significantly different annular combustors, and a reverse flow combustor. The latter configuration is typically difficult or impossible to model using conventional one-dimensional algorithms. No additional computational effort or convergence problems were found in modelling the four combustor test cases. Converged solutions to all cases were obtained within approximately 15 seconds on a Silicon Graphics Indy Workstation with an R4400 chip operating at 150 MHz.

Multi-annular combustors, lean premixed prevaporised combustors and reheat systems have also been successfully modelled using the network algorithm. The code has demonstrated accuracy and ease of convergence in modelling both aeronautical and industrial gas turbine combustors.

A network approach has been improved and developed which may be used with confidence in calculating combustor mass flow splits and pressure drops. The successful combustor flow modelling forms a solid foundation for the development of a full conjugate heat transfer algorithm capable of resolving the combustor liner wall heat transfer characteristics.



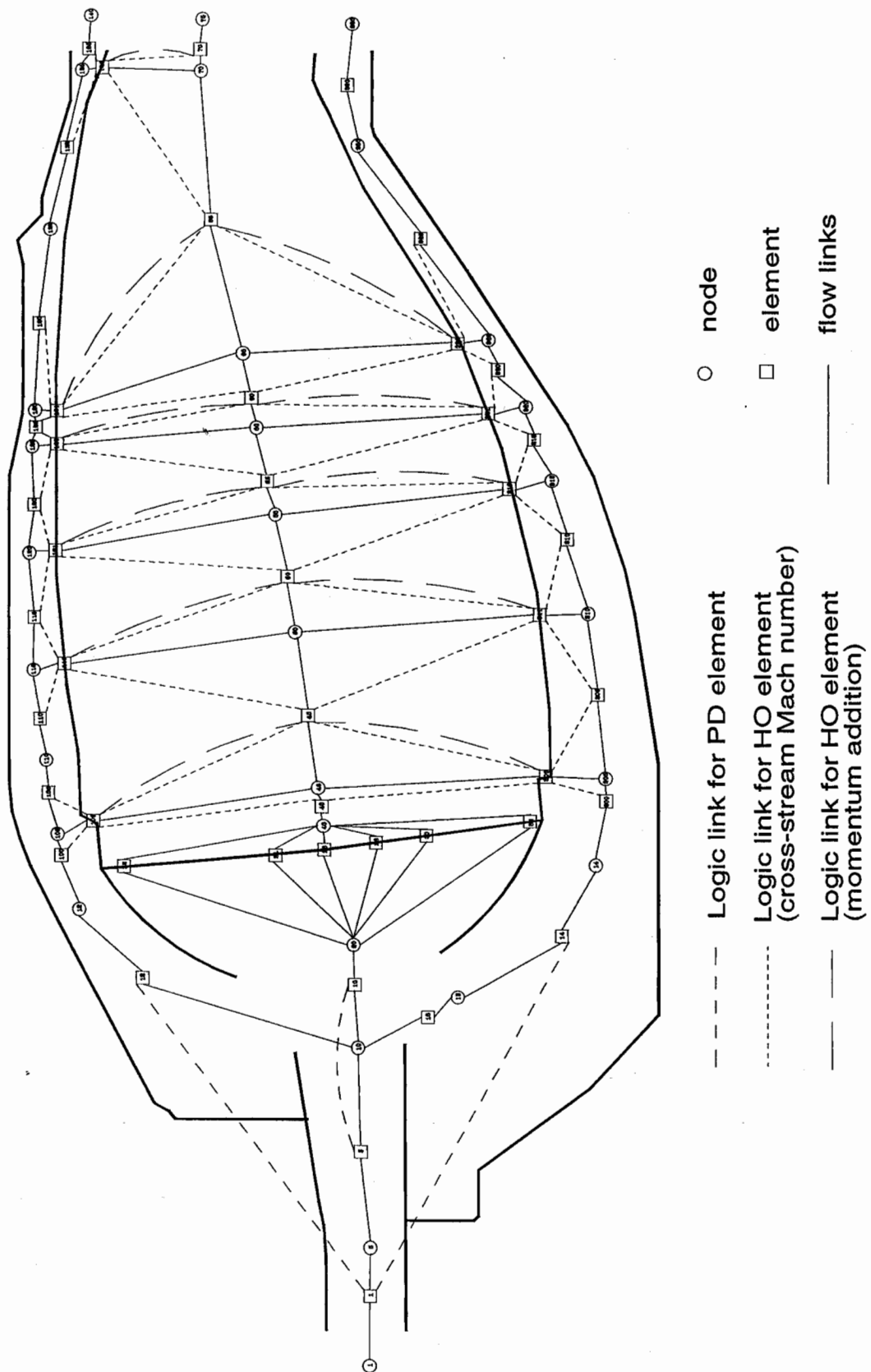


Figure 4.9. Isothermal Annular Combustor .1. network diagram

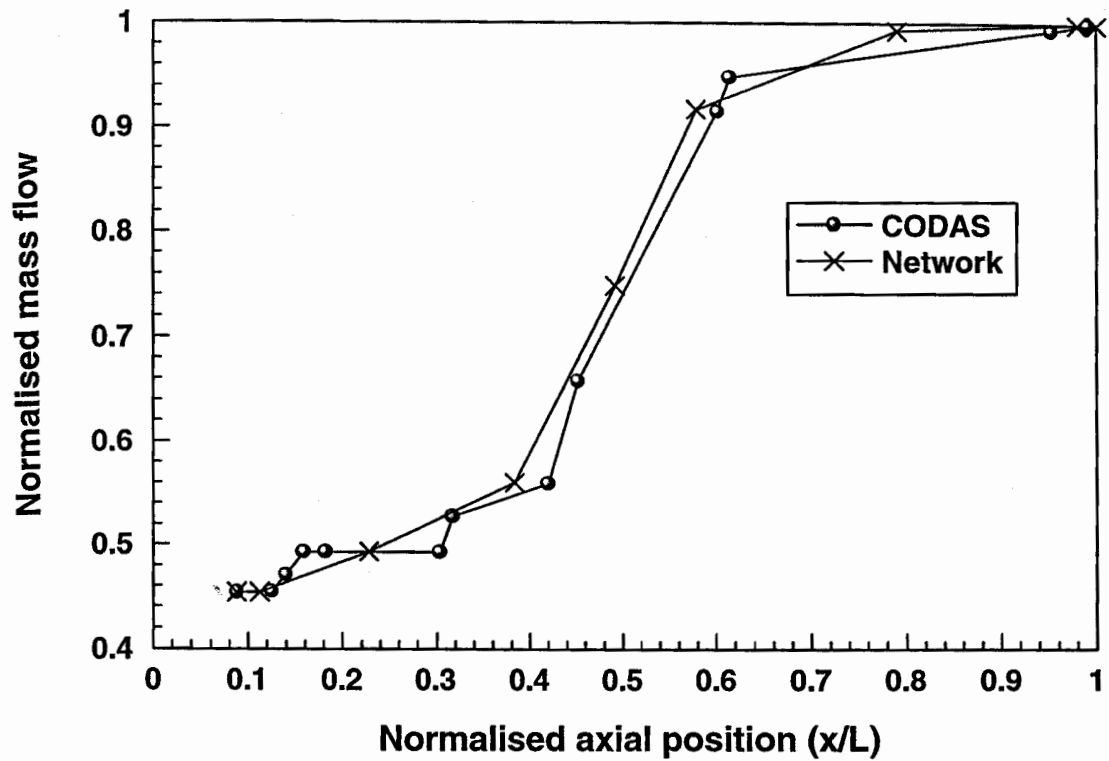


Figure 4.10. Isothermal Annular Combustor .1. flametube mass flow comparison

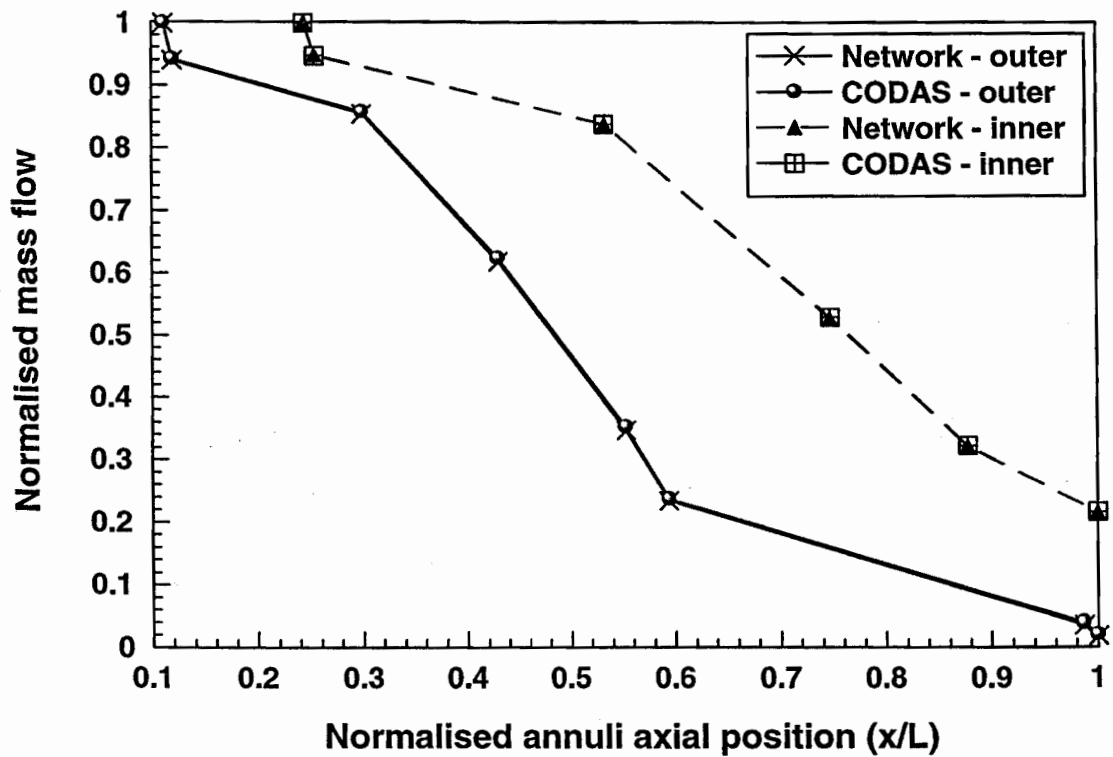


Figure 4.11. Isothermal Annular Combustor .1. annuli mass flow comparison

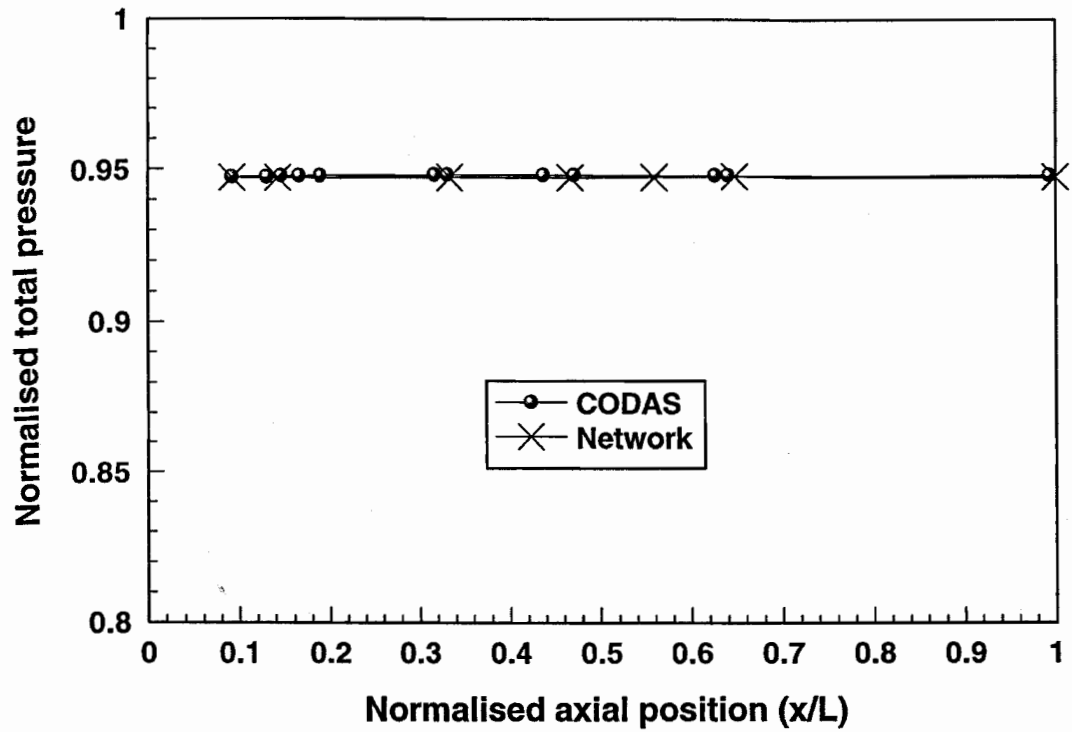


Figure 4.12. Isothermal Annular Combustor .1. flametube total pressure comparison

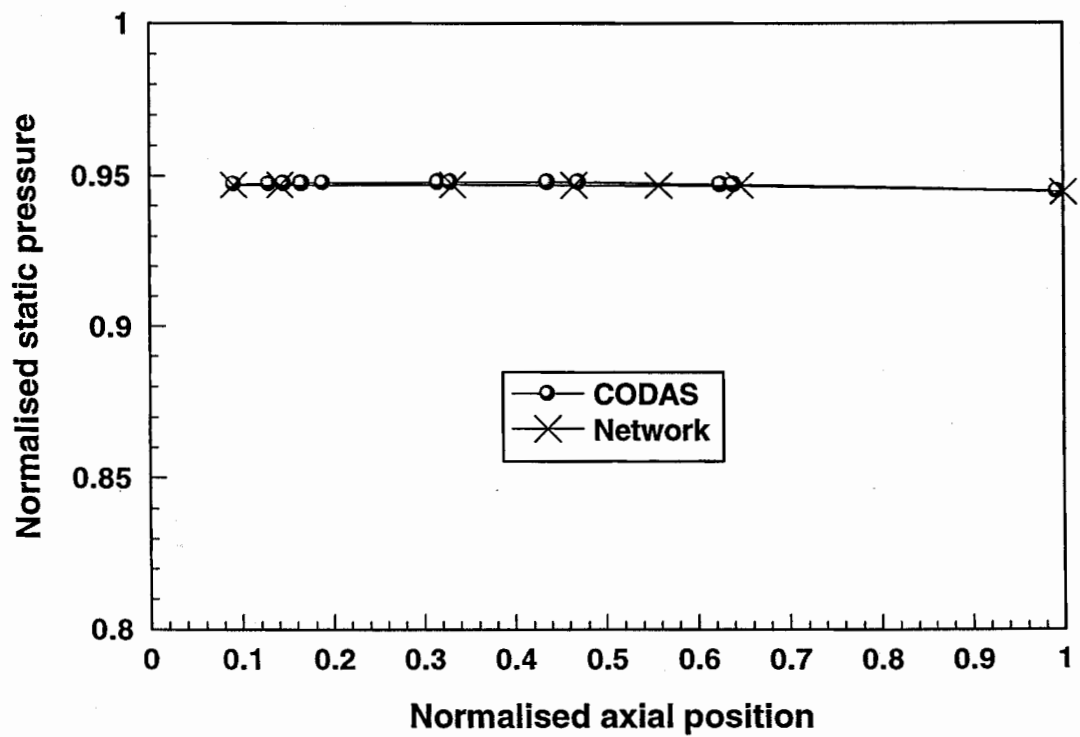


Figure 4.13. Isothermal Annular Combustor .1. flametube static pressure comparison

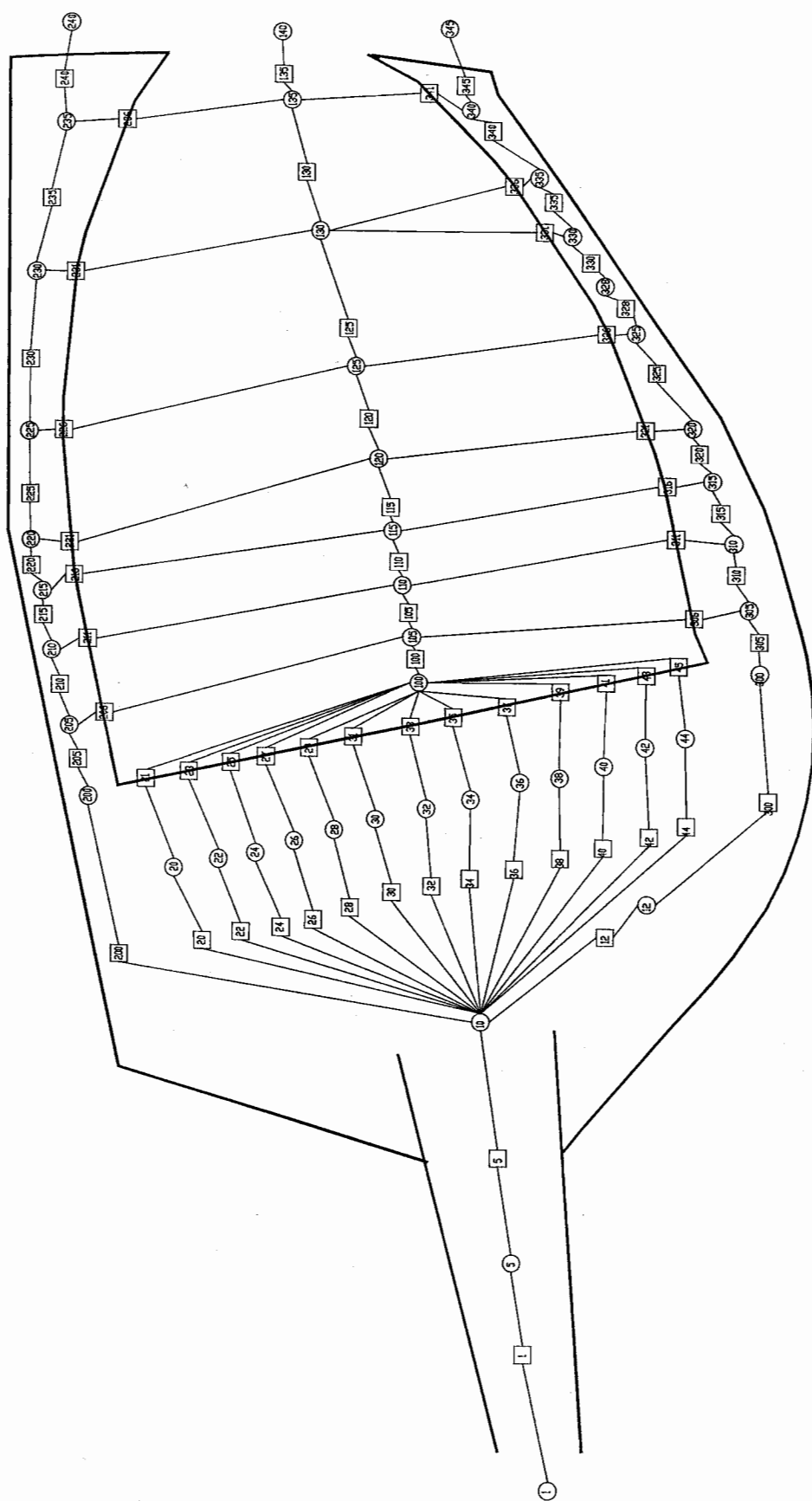


Figure 4.14. Isothermal Annular Combustor .2. network diagram

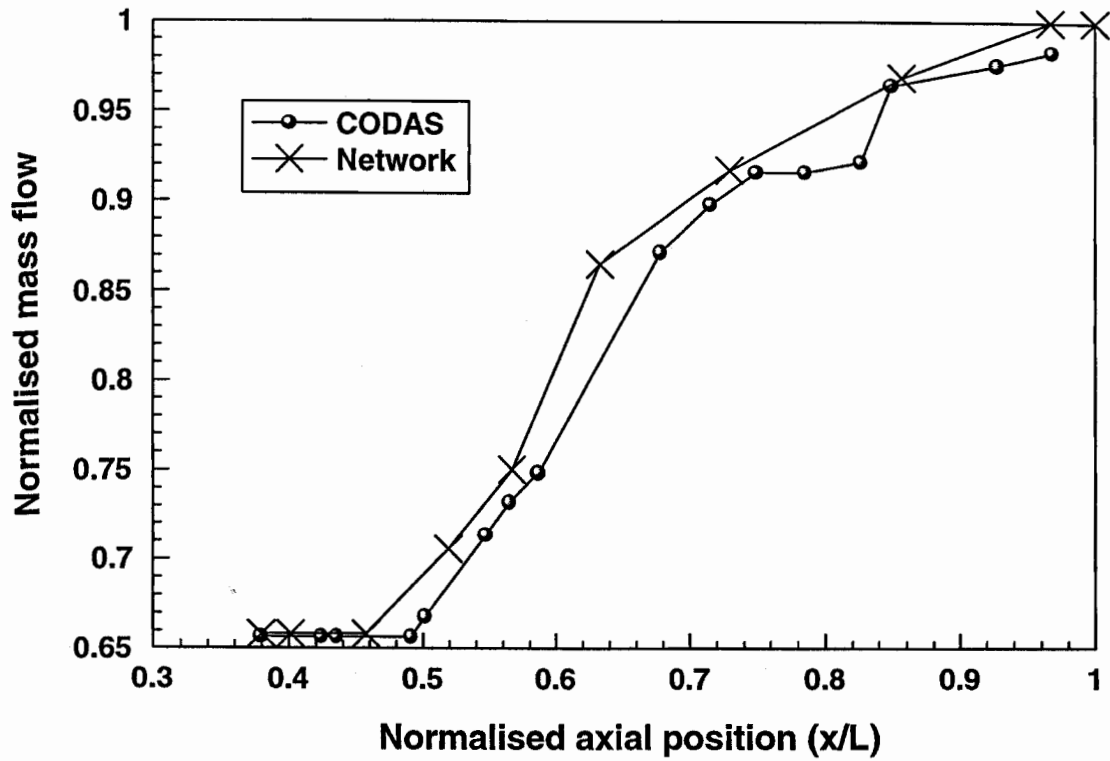


Figure 4.15. Isothermal Annular Combustor .2. flametube mass flow comparison

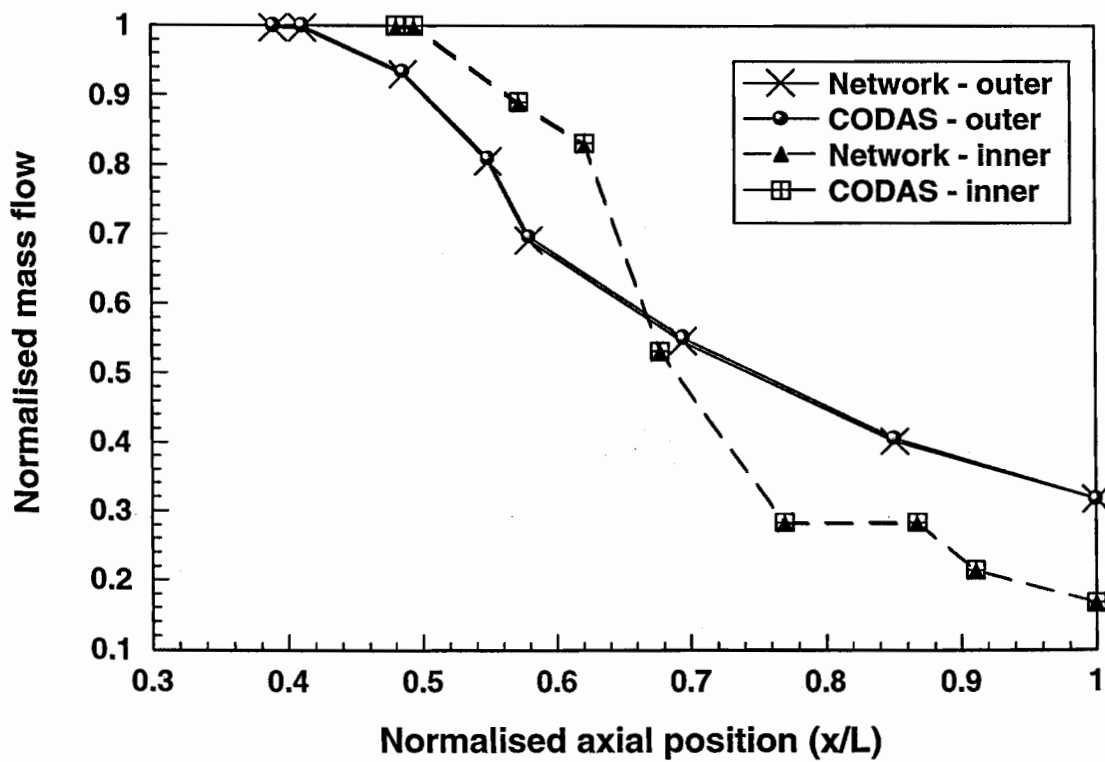


Figure 4.16. Isothermal Annular Combustor .2. annuli mass flow comparison

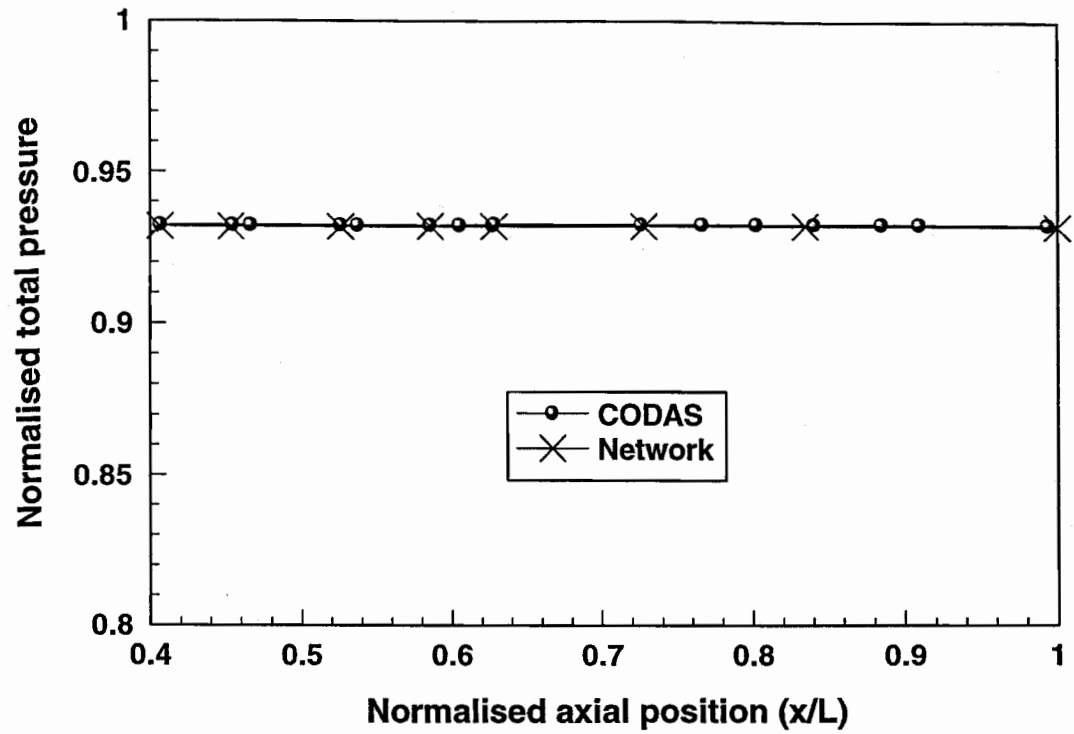


Figure 4.17. Isothermal Annular Combustor .2. flametube total pressure comparison

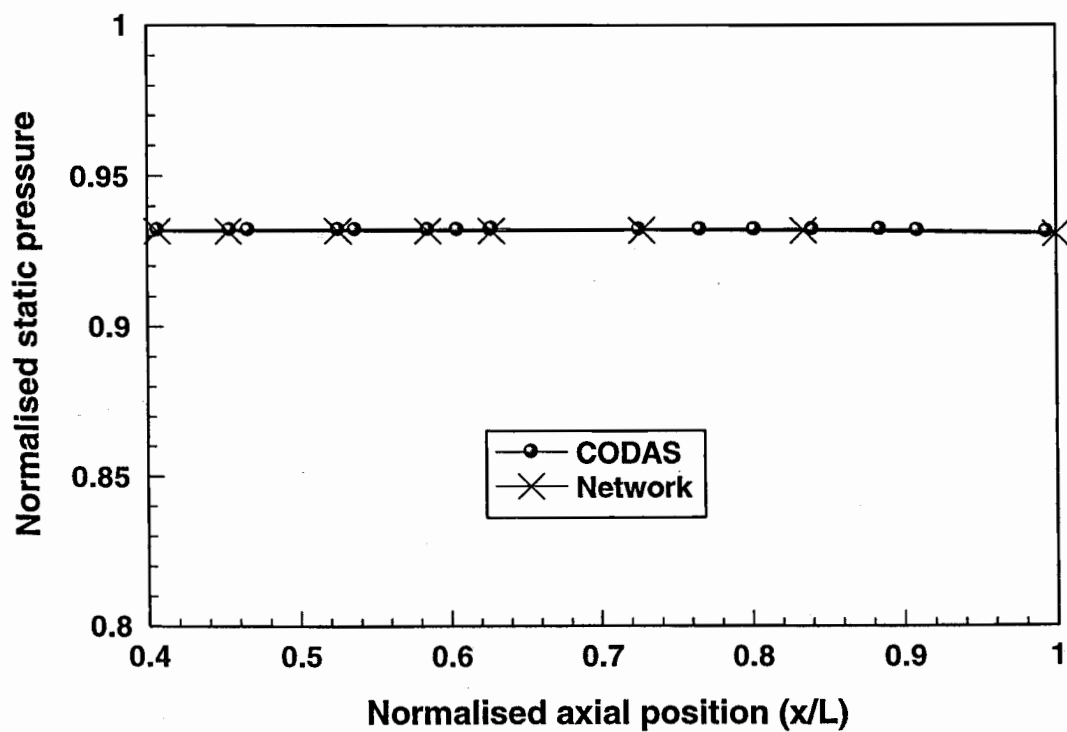


Figure 4.18. Isothermal Annular Combustor .2. flametube static pressure comparison

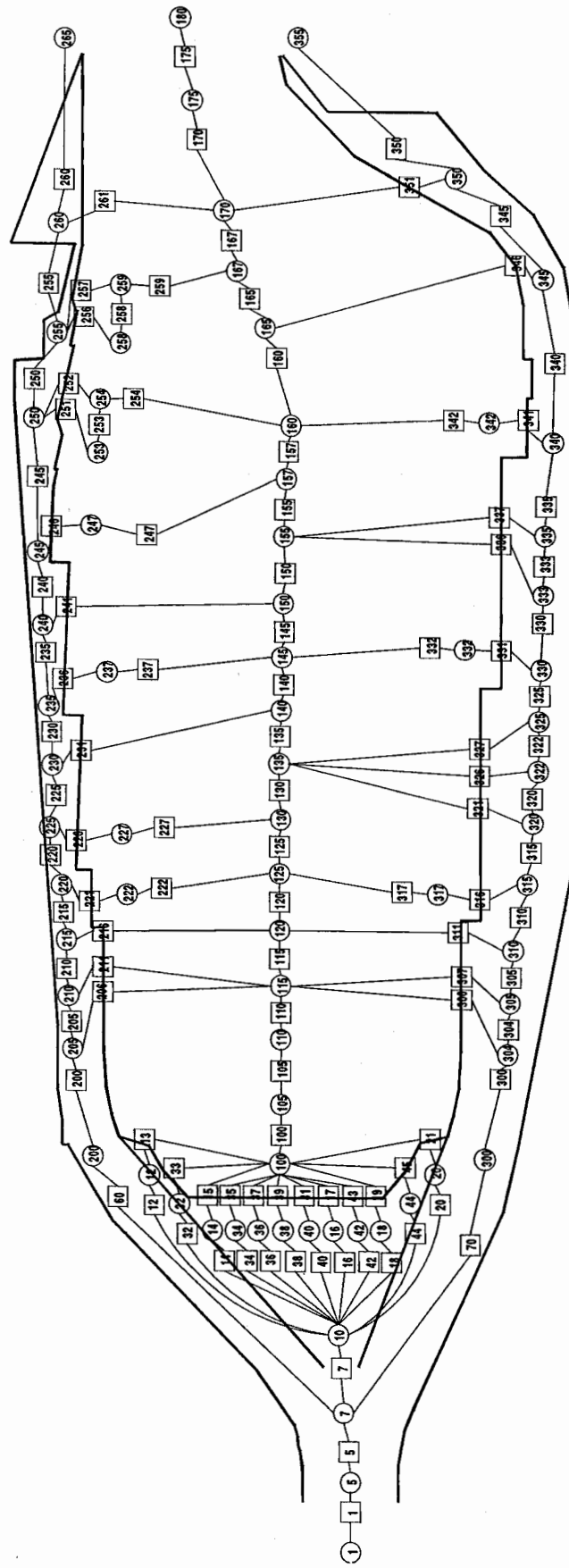


Figure 4.19. Isothermal Annular Combustor .3. network diagram

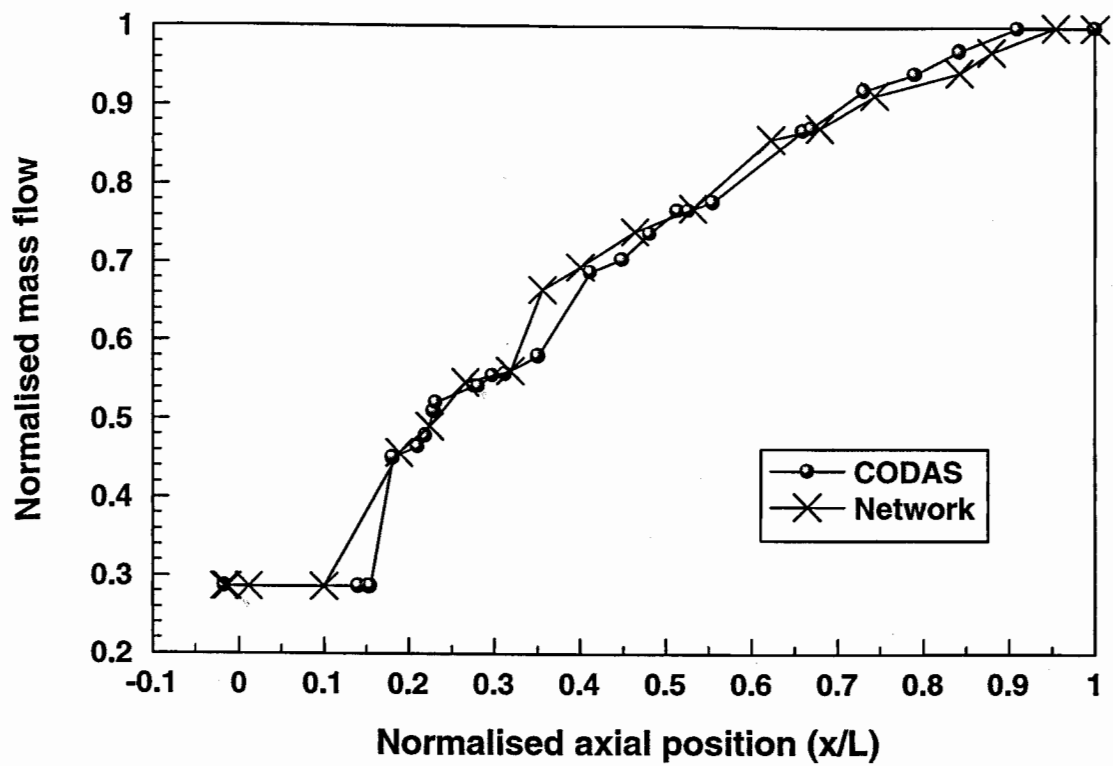


Figure 4.20. Isothermal Annular Combustor .3. flametube mass flow comparison

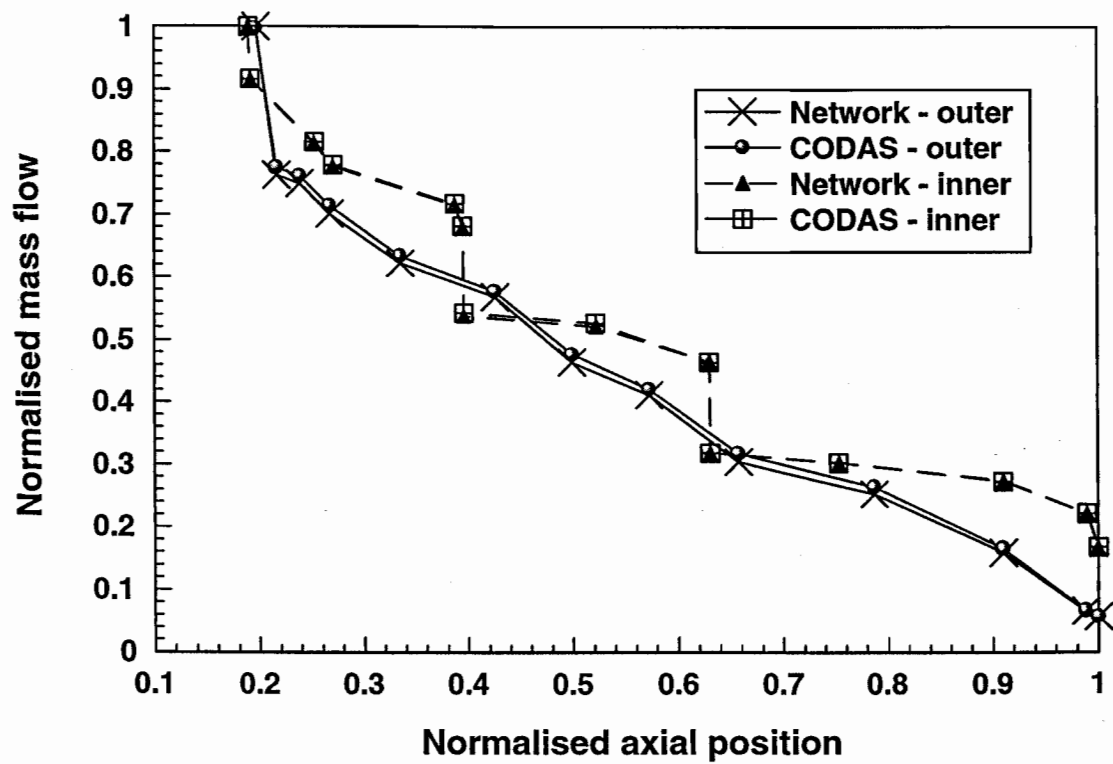


Figure 4.21. Isothermal Annular Combustor .3. annuli mass flow comparison



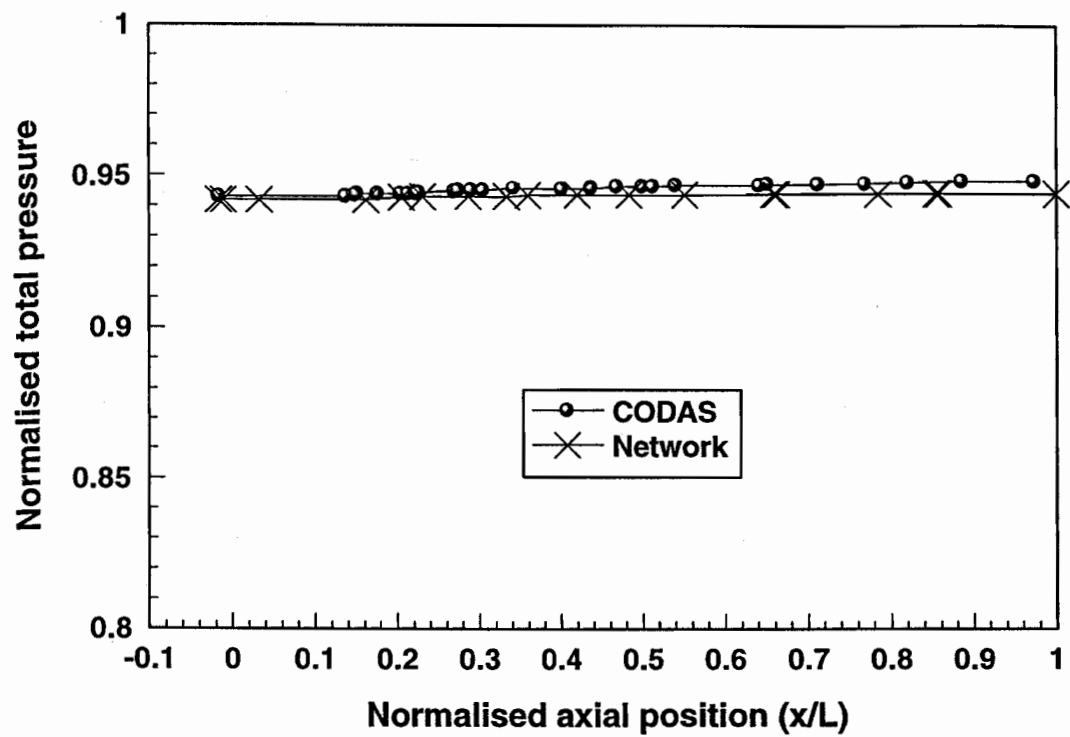


Figure 4.22. Isothermal Annular Combustor .3. flametube total pressure comparison

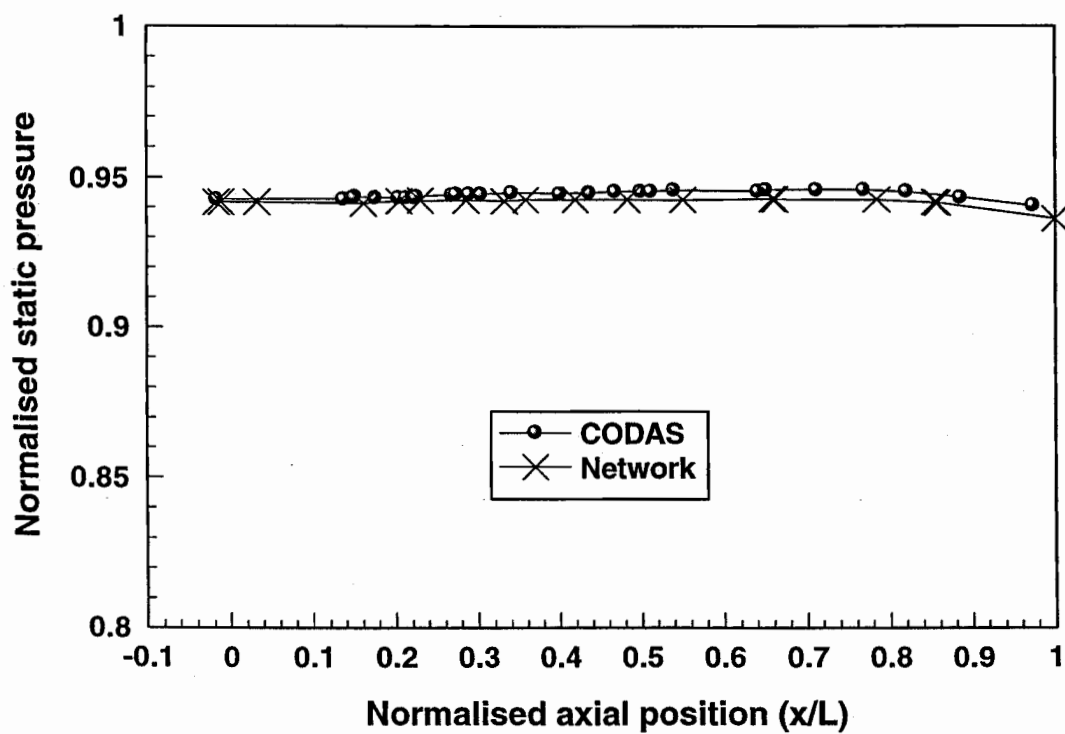


Figure 4.23. Isothermal Annular Combustor .3. flametube static pressure comparison

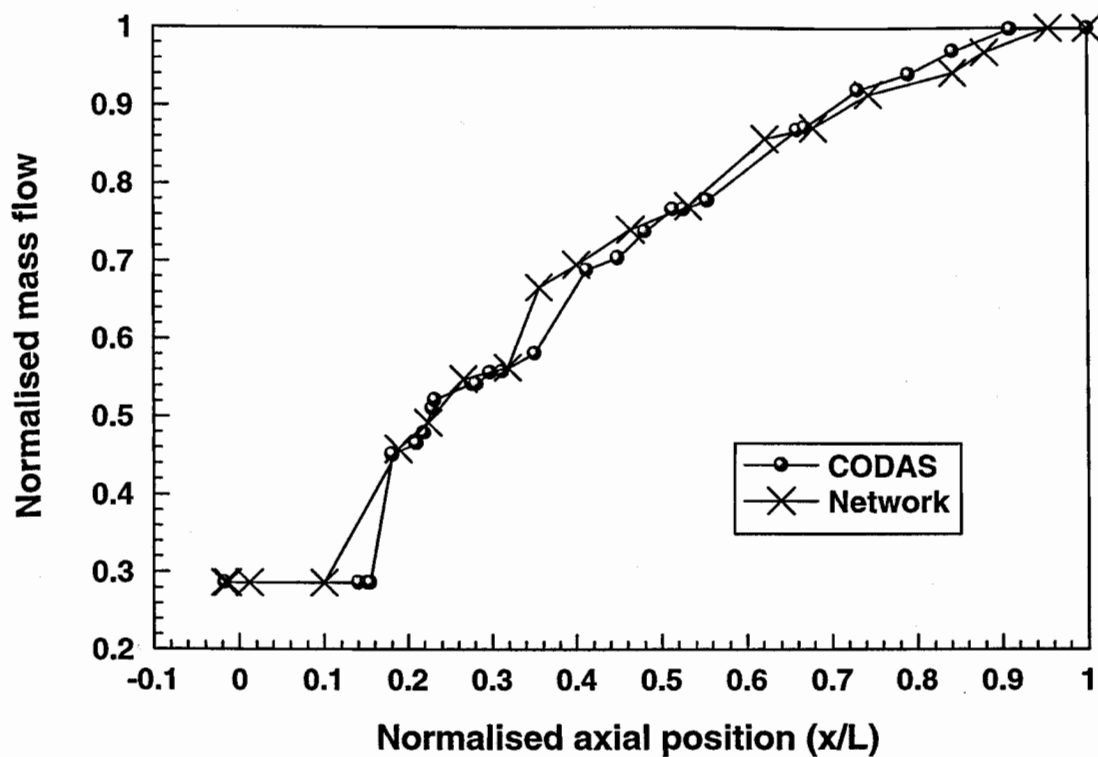


Figure 4.24. Isothermal Annular Combustor .3. flametube mass flow comparison  
(no slots)

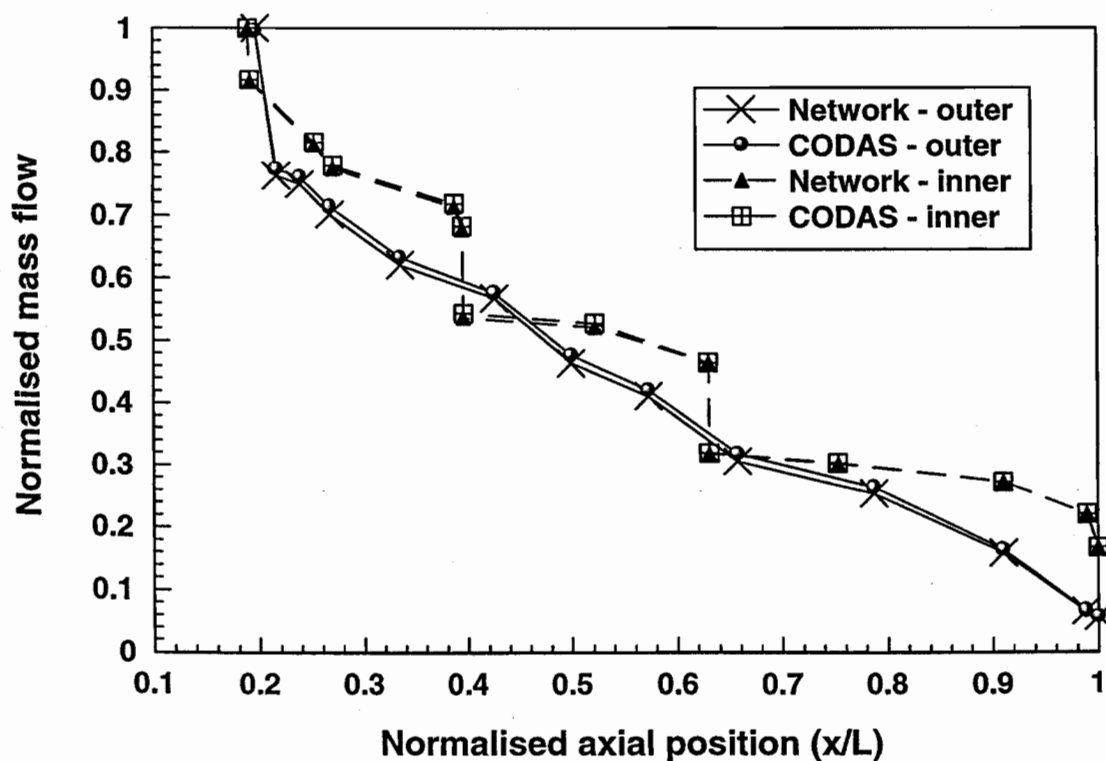


Figure 4.25. Isothermal Annular Combustor .3. annuli mass flow comparison (no slots)

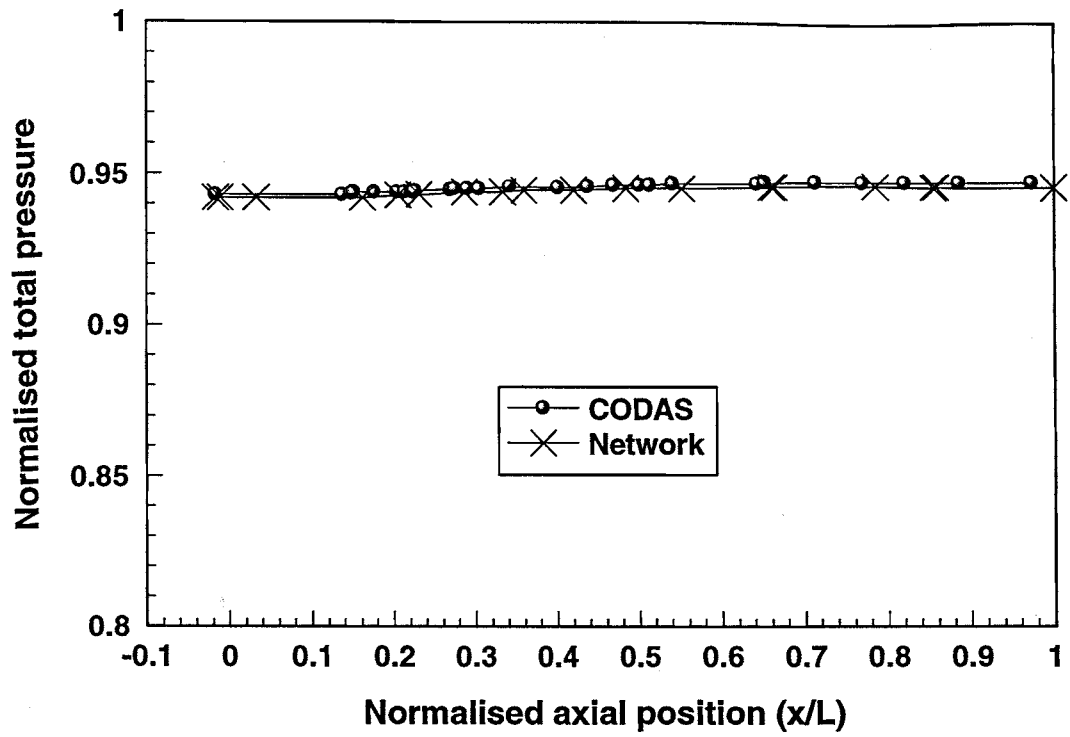


Figure 4.26. Isothermal Annular Combustor .3. flametube total pressure comparison  
(no slots)

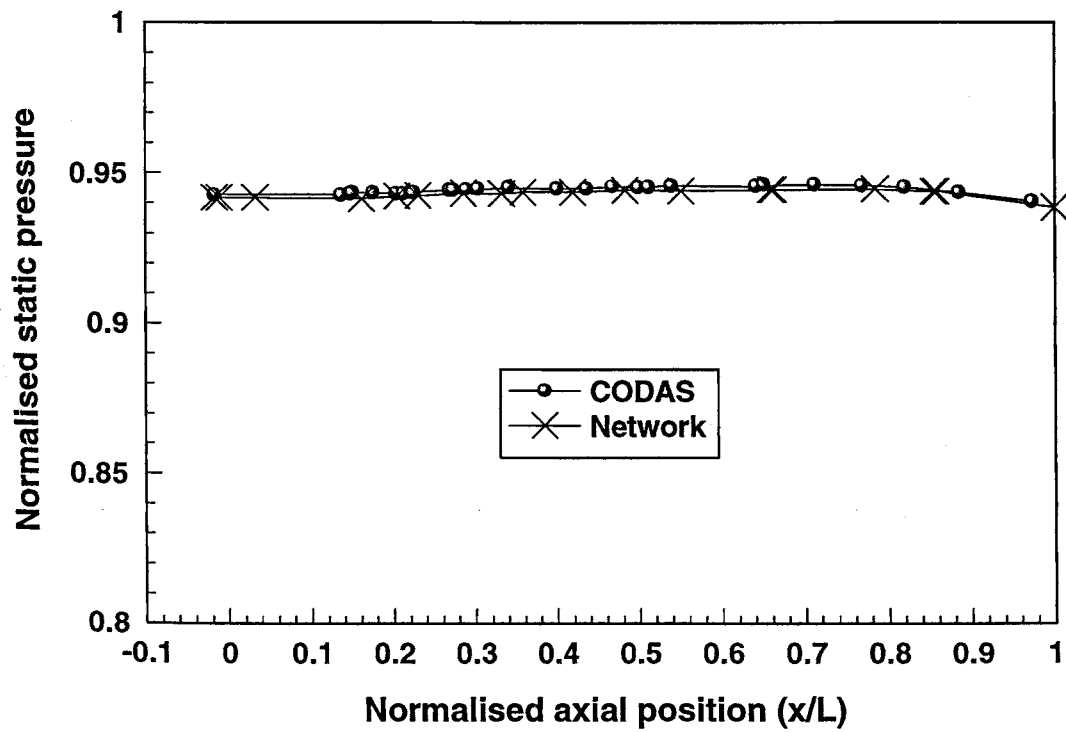


Figure 4.27. Isothermal Annular Combustor .3. flametube static pressure comparison  
(no slots)

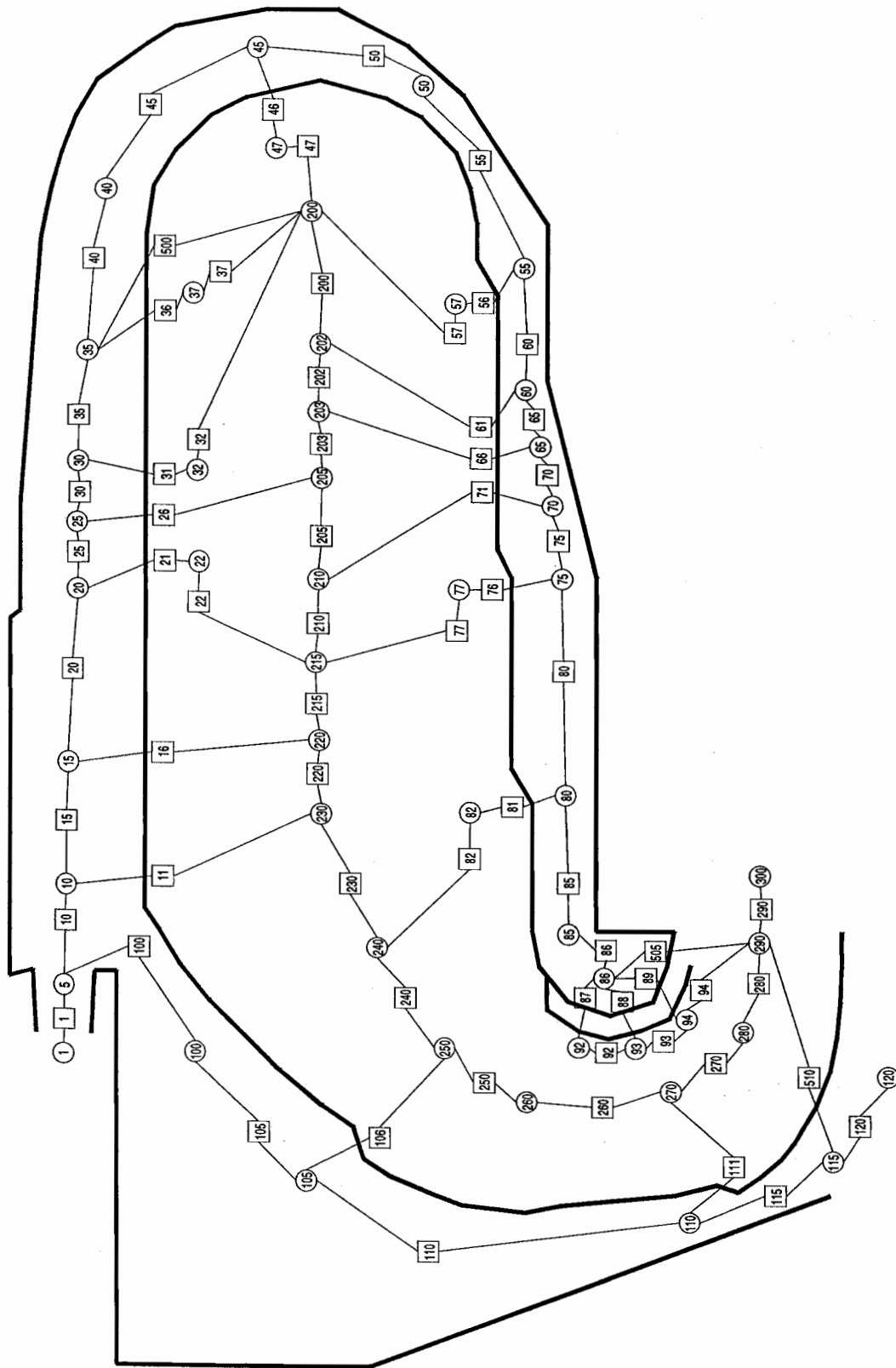


Figure 4.28. Reverse flow combustor network diagram

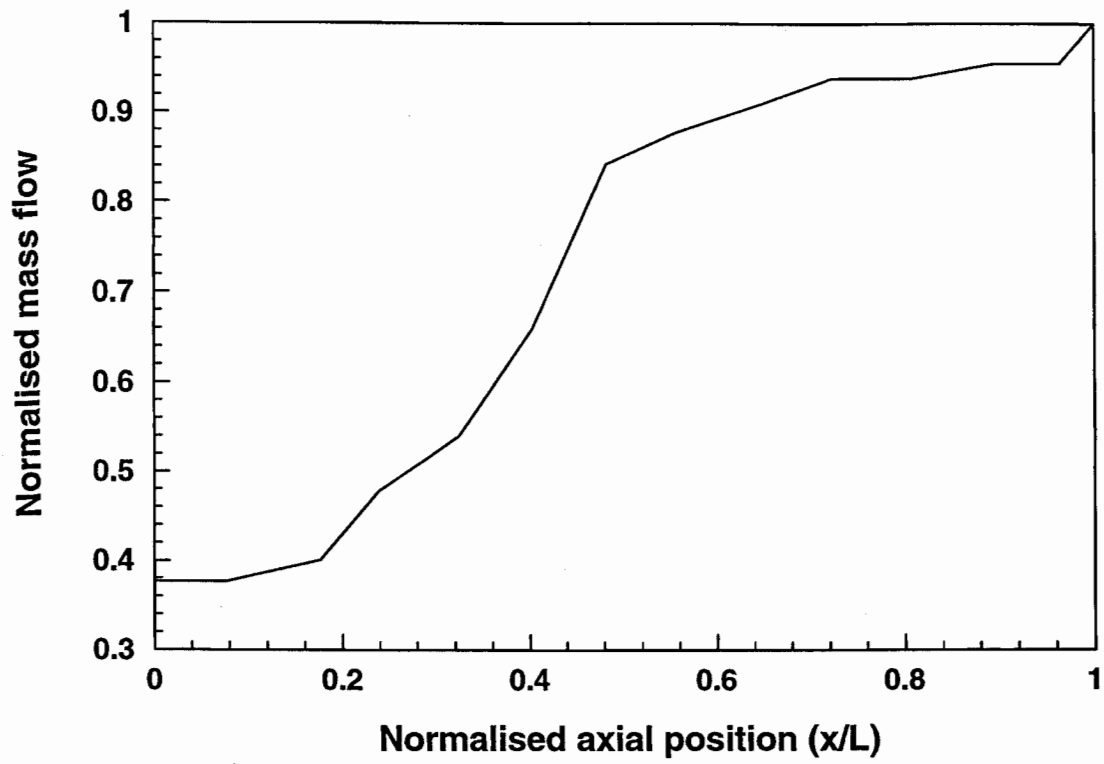


Figure 4.29. Reverse Flow Combustor flametube mass flow

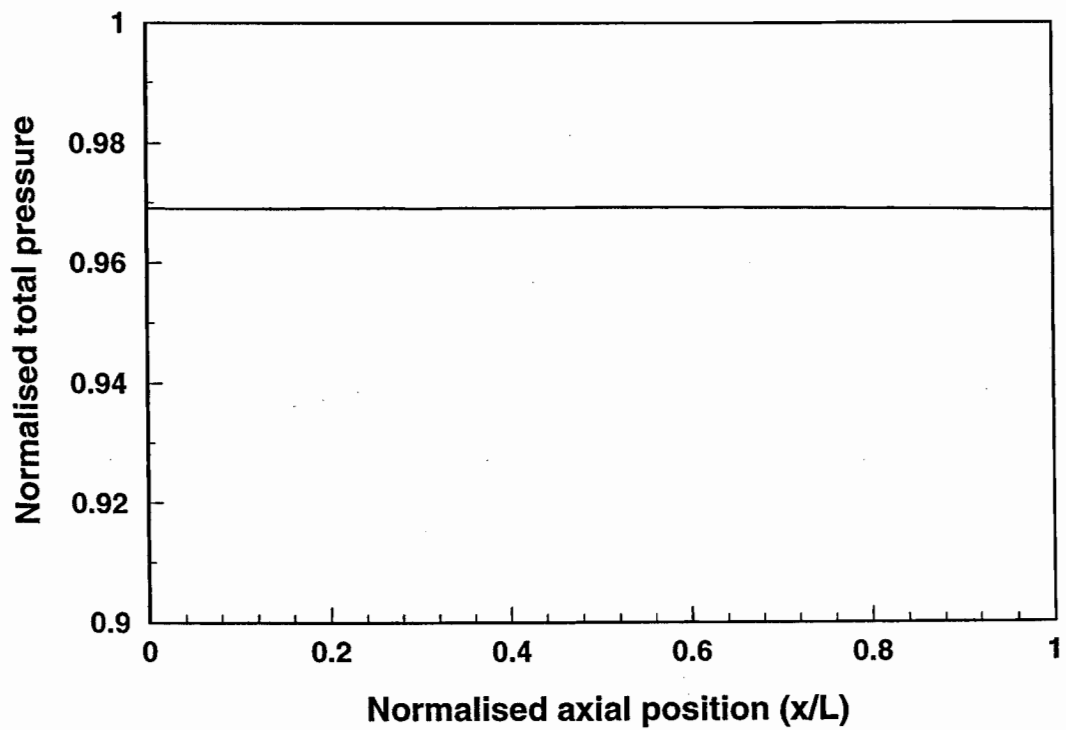


Figure 4.30. Reverse Flow Combustor flametube total pressure

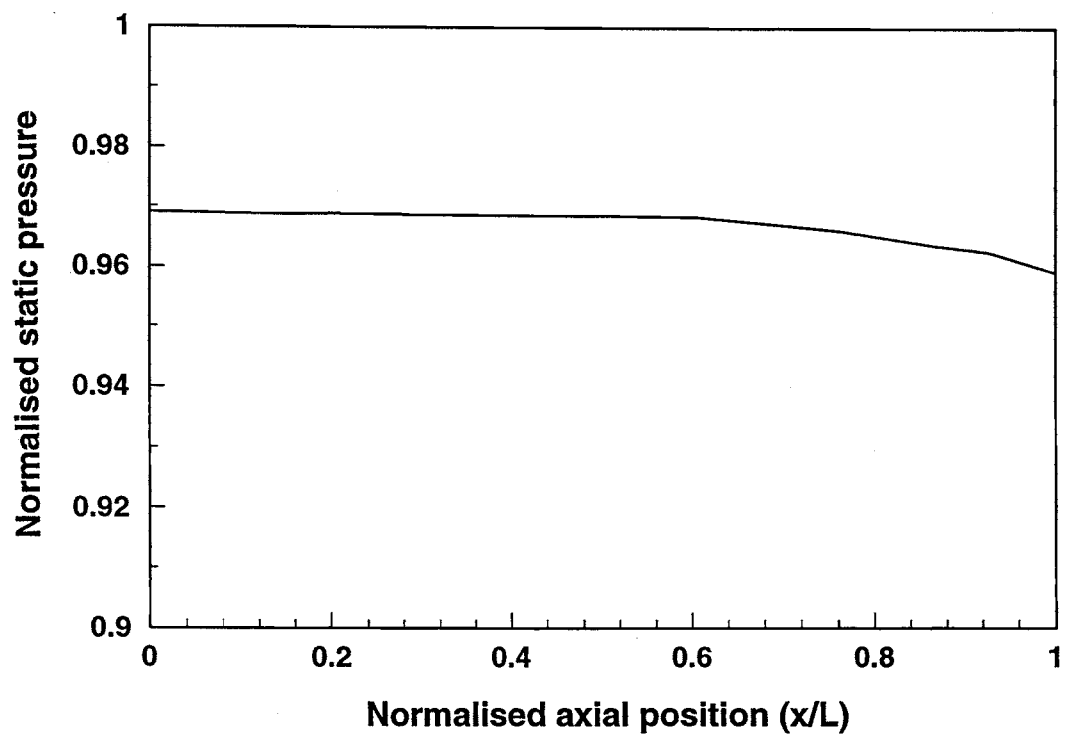


Figure 4.31. Reverse Flow Combustor flametube static pressure

## **5. Combustor heat transfer modelling**

### **5.1 Introduction**

The function of the combustor liner is to contain the burning gases within the flametube, metering the air into the flametube to achieve satisfactory combustion with the fuel and provide adequate liner wall cooling. The liner protects the structural integrity of the engine from the harsh combustion environment. The heat transfer characteristics of this critical component of the combustor are of significant importance.

Errors in the design or manufacture of the liner may result in buckling or cracking leading to failure, after a relatively short period of time. Inspection after long periods of time reveal buckling and cracking around geometrical discontinuities, such as liner holes, caused by the relatively higher residual stresses in these regions in the manufacturing process. Hot spots on the liner wall might result from distortion of the fuel spray, caused by a defective atomiser, misalignment of the atomiser, carbon build-up on the atomiser face (Lefebvre, 1983). Liner hot spots will also be caused by any non-uniformity in the liner wall which results in the breakdown of the convective cooling film adjacent to the wall, e.g. the wake region downstream of a primary port.

Generally, liner buckling occurs after extended periods of operation under conditions of high temperatures and high temperature gradients. Cracking results from low cycle fatigue caused by transient variations in the liner wall temperature (Lefebvre, 1983). These conditions are typically present in the combustor during acceleration and take-off. The liner life is thus enhanced by maintaining satisfactory temperatures and temperature gradients over the entire operating range of the combustor.

Current combustor liners are typically manufactured from nickel or cobalt based alloys which can withstand long term operation at temperatures up to 1150K (Mellor, 1990).

The flametube side of the liner wall may also be coated with a protective thermal barrier, typically zirconia based, reducing the liner cooling requirement. The liner is cooled by bleeding air from the annuli to generate convective cooling films adjacent to the liner wall. This reduces the amount of air available for combustion, and should be minimised for the best combustor efficiency.

The operating pressure of combustors has been steadily increasing over the years, and operating pressures above 40 bar are not uncommon in current production combustors. The rising pressure has increased the radiative load on the liner and has reduced the effectiveness of the liner film cooling as the compressor delivery air temperatures have increased. Thus the liner wall cooling has become increasingly critical, and as much as one third of the combustor airflow might be required for cooling purposes (Lefebvre, 1983). This corresponds to a reduction in the air available for dilution. The cooling air quenches the combustion reactions adjacent to the liner, and thus reduce combustion efficiency and increases emissions of carbon monoxide and unburned hydrocarbons. The optimisation of the liner cooling air requirement is therefore of critical importance.

A wide variety of wall cooling techniques have been developed to minimise the amount of cooling air required to maintain liner integrity ( Lefebvre, 1983 and Acosta, 1987).

The prediction of the convective and radiative heat transfer is a complex task. The effects of unusual geometric features in the liner and the generation of cooling films adds to the difficulty. Empirical correlations are coupled to the overall governing energy equations to compute the convective and radiative heat fluxes, in a similar way semi-empirical pressure-drop relationships were incorporated into the overall governing equations in the previous chapter. A wealth of convective heat transfer correlations have been developed for flow in pipes and ducts which can be adapted for use in the gas turbine combustor (Ozisik, 1985 and Bejan, 1993). These relationships take the form of Nusselt number correlations, corrected for entrance length, friction and temperature effects. Recent work has seen the development of a generalised correlation of heat transfer, unrestricted by the system geometry (Maciejewski and Anderson, 1996). Baukal and Gebhart (1996)



demonstrated the usefulness of semi-empirical correlations in problems involving flame impingement heat transfer. Correlations may offer simplicity in complex systems with only small penalties in accuracy. Care must be taken that the range of application of the correlation does not differ significantly from the range for which the formulation was developed, so as not to compromise the correlation accuracy.

Simon et al (1984) performed a full heat transfer analysis on a reverse flow combustor liner and compared calculated results with measured rig data. The semi-empirical correlations of convective and radiative heat transfer were found to give good agreement with the experimental measurements. Paskin and Mongia (1993) evaluated an empirically based design methodology to model the heat transfer on a small combustor compliant metal/ceramic wall, which used an intermediate fibre layer to moderate the differential expansion of the metal and ceramic layers. These two pieces of work demonstrated the usefulness of a liner heat transfer simulation for analysing this critical component of the gas turbine combustor.

This chapter discusses the development, implementation and usage of a conjugate heat transfer model, and provides two examples of the procedure applied to gas turbine combustors. The development of a conjugate heat transfer model allows the complete coupled flow and energy modelling of a gas turbine combustor, providing a detailed description of the liner wall heat transfer mechanism.

## 5.2 Constrained equilibrium adiabatic correction

A constrained equilibrium calculation is used to compute adiabatic flame temperatures, as discussed in the previous chapter. This computation, as the title suggests, may take no account of the heat loss from the flametube. The convective and radiative losses are treated as source terms in Eq. (3.2). The source term is calculated from

$$E = \dot{m}_{i,j} Cp (T_{fl} - T_{n,i,j}) \quad (5.1)$$

where,

$T_{fl}$  = adiabatic flame temperature from equilibrium calculation

$T_{n,i,j}$  = upstream node temperature

Assume that there is only one upstream branch to a particular node. Substituting Eq. (5.1) into Eq. (3.22) clearly results in the new node temperature only being dependent upon the calculated adiabatic flame temperature. No account is taken of the heat loss, since the temperature difference in the source term Eq. (5.1) effectively compensates for any reduction in the upstream branch temperature.

The problem is solved by tracking and accumulating any heat loss down the flametube, and correcting the source term appropriately,

$$E = \dot{m}_{i,j} Cp (T_{fl} - T_{n,i,j}) - \text{heat loss} \quad (5.2)$$

Since the adiabatic flame temperature,  $T_{fl}$ , is unaffected the combustion model is not compromised, and as far as the equilibrium model is concerned the flametube section remains adiabatic. In combustors with more than one flametube the heat loss is tracked for each combusting section and accumulated if the streams merge, as in a double annular combustor.

### 5.3 Conjugate Heat Transfer Models

A conjugate heat transfer model allows the prediction of heat transfer from a fluid, through a solid, to a fluid on the other side of the solid. Conduction models are required to account for the heat transfer within the solid. Convection and radiation models simulate the heat transfer through the fluid to the solid boundaries.

The conjugate heat transfer formulation allows the modelling of the liner wall along the entire length of the combustor. The flametube-side of the liner wall is heated by convection and radiation from the hot combusting gases. When calculating the heat transfer to the liner wall the presence of any wall cooling films must be accounted for. The annulus-side of the liner wall loses heat to the cooler annulus air flow through convection, and also through radiation to the casing. Axial and radial conduction transfers heat across and along the liner wall. Figure 5.1. illustrates this process.

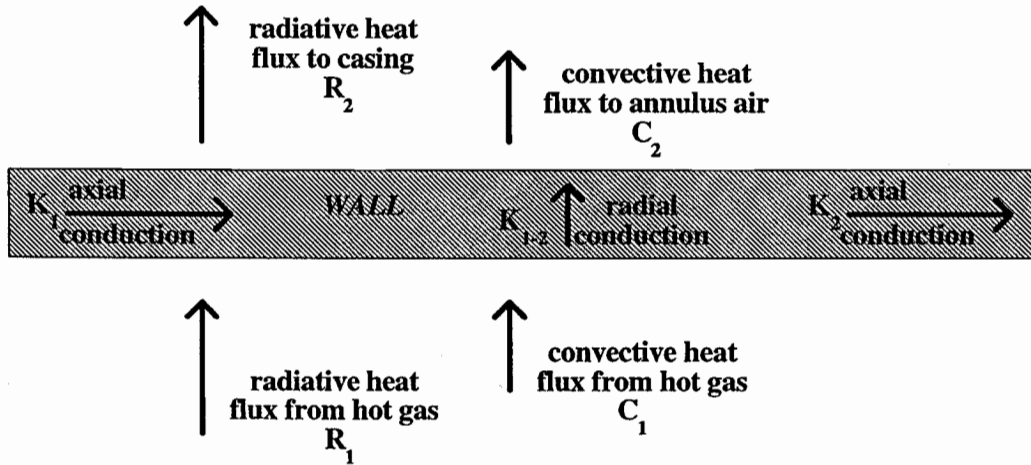


Figure 5.1. Wall conjugate heat transfer model

Mathematically, this is equivalent to the following heat balance,

$$(R_1 + C_1)\Delta A_{w1} + K_1\Delta A_{wa} = (R_2 + C_2)\Delta A_{w2} + K_2\Delta A_{wa} \quad (5.3)$$

Typically, the axial heat flux is negligible, and the liner walls very thin, so the areas are almost identical. This simplification allows the balance to be re-written as,

$$R_1 + C_1 = R_2 + C_2 = K_{1-2} \quad (5.4)$$

The derivation of each of these terms will be discussed in detail in the sections which follow.

## 5.4 Conduction (CD)

Axial, radial and circumferential conduction are present in a real combustor. Circumferential conduction and to a slightly lesser degree axial conduction (since axial variation is normally more significant than circumferential variation in the flametube flow field and the positioning of liner wall features) may be assumed negligible. Axial conduction may not be negligible in regions of liner wall features.

Assuming that the wall is very thin the radial conduction may be written as,

$$K_{1-2} = \frac{k_w}{t_w} (T_{w1} - T_{w2}) \quad (5.5)$$

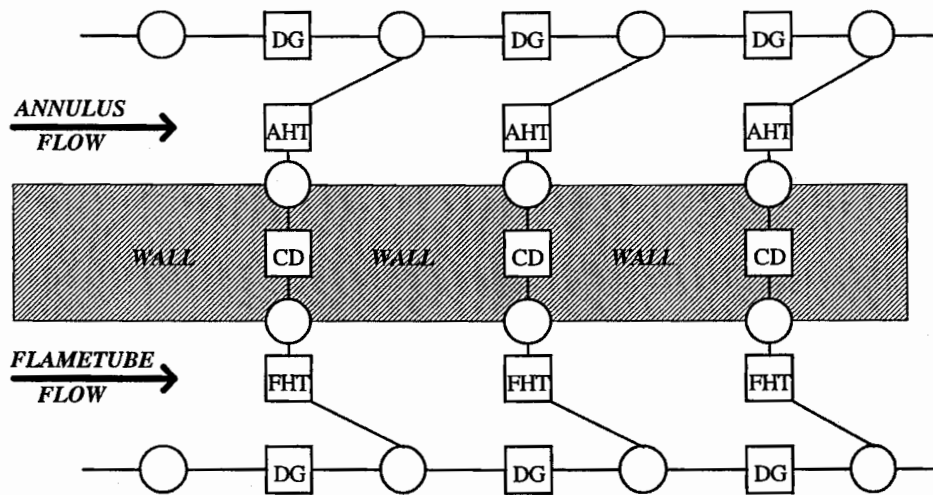


Figure 5.2. Network specification for conjugate wall heat transfer

Figure 5.2 illustrates the network set-up for a one-dimensional conjugate heat transfer analysis of the liner wall. The *DG* elements refer to duct sections, containing the working fluid. The *AHT* elements refer to the convective and radiative heat transfer to the annulus. The *CD* elements represent the conductive heat transfer through the liner wall.

The *FHT* elements refer to the convective and radiative heat transfer from the combustion gases within the flametube.

Figure 5.3. below shows a second commonly used option for modelling combustors with thermal barrier coatings.

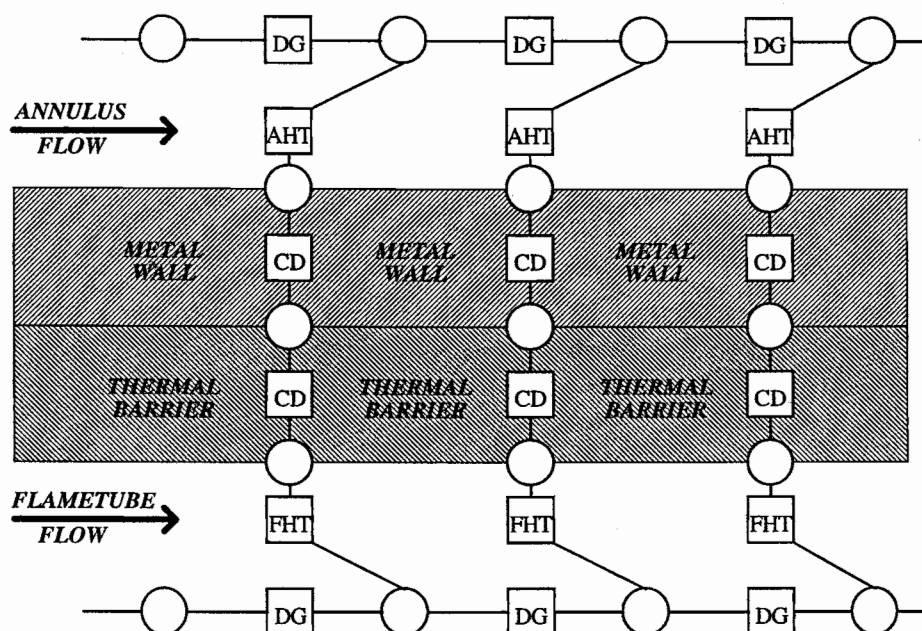


Figure 5.3. Network specification for double layer conjugate liner wall heat transfer

Although the axial conduction component is normally much smaller than the radial component, instances occur where the axial conduction may be significant.

The overall governing equation for 2D conduction is similar to that for 1D conduction. However, the conductive heat transfer coefficient,  $R$ , must be modified to account for the differing areas of heat transfer in the axial and radial direction. Since the circumferential component of surface area is common to both the axial and radial direction, the conductive heat transfer coefficient,  $R$ , need only be modified by a length component. The heat balance strategy is shown below, and refers to Fig. 5.4.

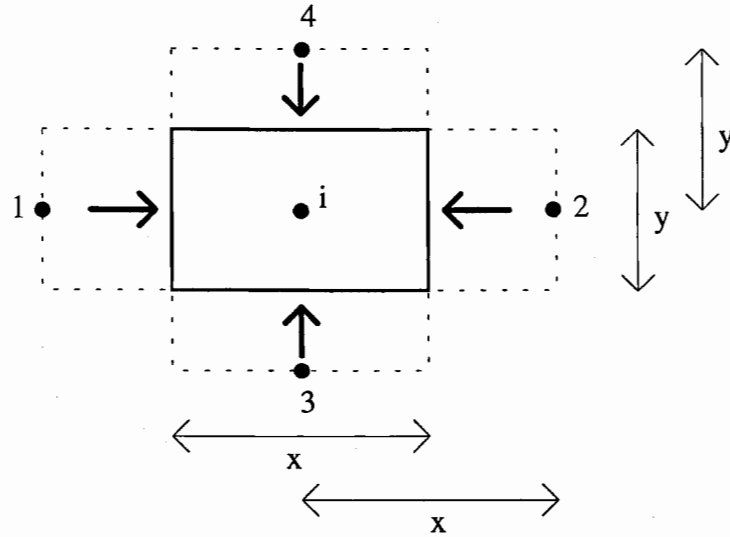


Figure 5.4. Energy balance nomenclature for two-dimensional conduction

$$Q_1 + Q_2 + Q_3 + Q_4 = 0 \quad (5.6)$$

$$\frac{k}{x}(T_i - T_1)y + \frac{k}{x}(T_i - T_2)y + \frac{k}{y}(T_i - T_3)x + \frac{k}{y}(T_i - T_4)x = 0 \quad (5.7)$$

The following network diagram (Fig 5.5) illustrates this strategy for the case of a two layered wall.

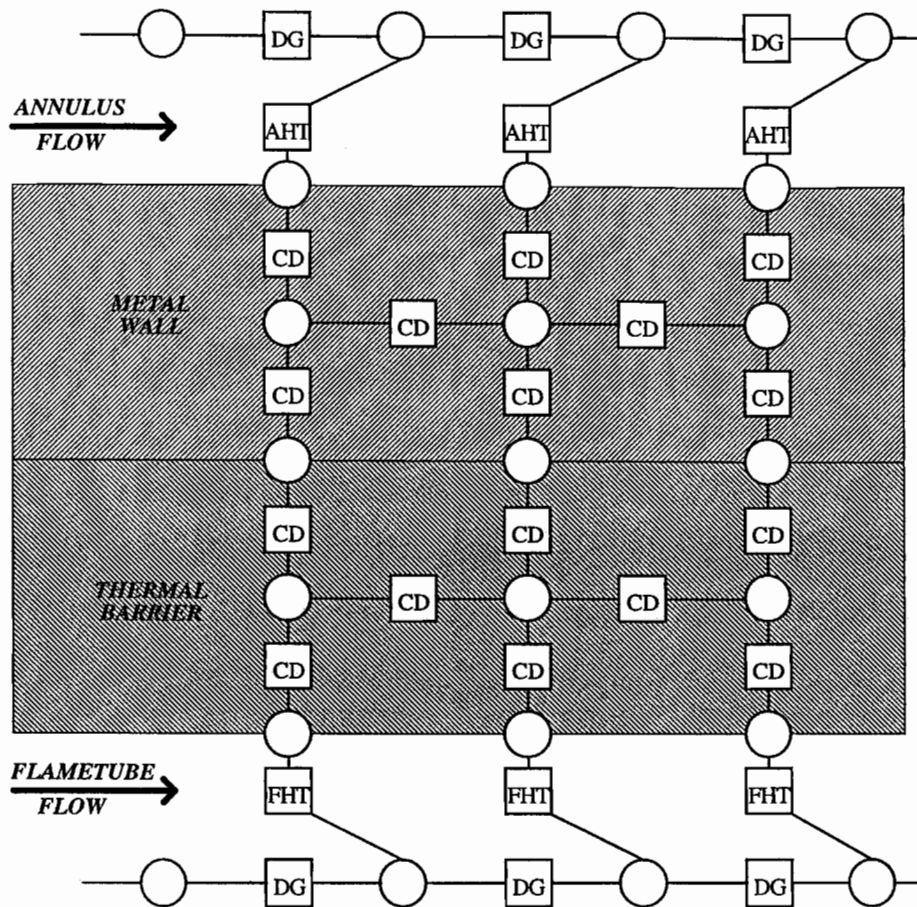


Figure 5.5. Network specification for conjugate wall heat transfer with two-dimensional (axial and radial) conduction including two wall materials

The thermal conductivity of the liner material has a significant effect on the heat transferred through the liner wall. The use of thermal barrier coatings has become a popular strategy for lowering the liner wall metal temperatures adjacent to the combustion gases.

Details of thermal barrier material properties have been provided by Calson and Stoner (1977) and Liebert (1978). Thermal barrier coatings have very low thermal conductivities, and effectively insulate the liner wall. Typical thermal barrier conductivities fall in a range from 0.5 - 2.0 W/mK. There is some uncertainty as to the precise thermal conductivities of materials such as yttria stabilised zirconia, a popular coating material, at elevated temperature. The value chosen is critical to the prediction of



the wall heat transfer mechanism, as only small variations in the value will lead to large changes in the computed heat flux.

Coalmer and Vafai (1995) performed a detailed three-dimensional finite element analysis on the liner wall conduction characteristics. The large temperature gradients associated with thermal barrier coatings were evaluated over a range representative thermal barrier conductivities. Small variations in thermal conductivity and barrier thickness were shown to have very significant effects on the heat flux transport. The yttria based zirconia was thought to have a thermal conductivity in the range from 0.8 to 1.2 W/mK at elevated temperature (Vafai, 1996). This uncertainty in the thermal conductivity corresponds to a variation of up to one third in the computed heat fluxes, highlighting the need for accurate properties information.

## 5.5 Annulus heat transfer (AHT)

### 5.5.1 Convection

The convective heat flux is predicted using Nusselt number correlations, which may be modified for entrance length, wall friction and temperature gradient effects if required. Detailed empirical analysis have been performed to produce empirical correlations in pipe and duct geometries (Notter and Sleicher, 1972, Gnielinski, 1975, and Shah and Johnson, 1981).

Assuming that fully developed turbulent flow pre-dominates, a correlation which has been used with success to simulate the external liner heat transfer is (Lefebvre, 1983),

$$C_2 = h(T_{w2} - T_{an}) \quad (5.8)$$

where,

$$h = 0.020 \frac{k_{an}}{D_{an}^{0.2}} \left( \frac{\dot{m}_{an}}{A_{an} \mu_{an}} \right)^{0.8}$$
$$D_{an} = 4 \frac{\text{cross - sectional area of flow}}{\text{wetted perimeter}}$$

The geometry on the annulus side of the liner wall is not normally continuous, with interruptions from holes, cooling features, or struts. Thus the boundary layer is often destroyed a number of times down the annuli. This has a significant effect on the convective heat transfer due to the significantly higher heat transfer effectiveness of a developing boundary layer compared to a fully-developed boundary layer. If a parameter for the developing boundary layer is included in the convection correlation this effect may be simulated by restarting the film from each point in the annuli at which it is destroyed. An alternative formulation for the heat transfer coefficient,  $h$ , in Eq. (5.8) accounting for entrance length effects is (Modest, 1990),

$$h = 0.036 \frac{k_{an}}{D_{an}} Re_{an}^{0.8} Pr^{0.33} \left( \frac{D_{an}}{L} \right)^{0.0555} \quad (5.9)$$

where,

$L$  = distance from local origin of boundary layer

Eq. (5.9) is applicable for  $10 < L/D < 400$ , for smaller ratios the entrance length term was removed from the equation.

In an analysis evaluating more recent heat transfer correlations Stuttford et al (1995) found the modified Petukhov Nusselt number correlation one of the better more modern formulations for flows in pipes,

$$Nu = \frac{Re Pr (f/2)}{1.07 + 12.7 (Pr^{2/3} - 1) (f/2)^{1/2}} \quad (5.10)$$

where,

$$\text{Nusselt number, } Nu = \frac{h D_{an}}{k_{an}}$$

$$\text{fanning friction factor, } f = [1.58 \ln(Re) - 3.28]^{-2}$$

The friction factor and Nusselt number may be corrected for wall temperature effects as follows (Shah and Johnson, 1981),

$$f = f \left( \frac{T_{w2}}{T_{an}} \right)^m \quad (5.11)$$

$$Nu = Nu \left( \frac{T_{w2}}{T_{an}} \right)^n \quad (5.12)$$

where,

for *Heating* ( $T_{wall} > T_{gas}$ )

for *Cooling* ( $T_{wall} < T_{gas}$ )

$$n = - \left[ \ln \left( \frac{T_{w2}}{T_{an}} \right) \right]^{1/4} + 0.3$$

$$m = -0.52$$

$$n = 0$$

$$m = -0.38$$

Entrance length effects may be accounted for by,

$$Nu = Nu \left[ 1 + \left( \frac{x_b}{D_{an}} \right)^{-2/3} \right] \quad (5.13)$$

Thus a correlation may be used accounting for surface friction, temperature gradient, and entrance length.

### 5.5.2 Radiation

Radiation from the liner wall to the outer casing is usually much smaller than the convective component, but becomes more significant with increasing liner wall temperature. The assumption is made that the liner and casing only exchange radiation with each other, i.e. there are no end effects. Assuming gray gas emissivities for the wall, and uniform axial temperatures in the calculation segment, the radiation may be specified as (Lefebvre, 1983),

$$R_2 = \frac{1}{A_w} \left( \frac{\sigma(T_{w2}^4 - T_{ca}^4)}{\frac{1 - \epsilon_{w2}}{\epsilon_{w2} A_w} + \frac{1}{A_w F_{wc}} + \frac{1 - \epsilon_{ca}}{\epsilon_{ca} A_{ca}}} \right) \quad (5.14)$$

where,

$F_{wc}$  = geometric shape factor = 1 for long annular sections

A simpler alternative which has been used with success is (Modest, 1990),

$$R_2 = \frac{\sigma(T_{w2}^4 - T_{ca}^4)}{\frac{1}{\epsilon_{w2}} + \frac{1}{\epsilon_{ca}} - 1} \quad (5.15)$$

## 5.6 Flametube heat transfer (FHT)

### 5.6.1 Convection

The flametube side of the liner wall is subject to extreme temperatures and is typically cooled by air films generated by liner wall features. If there is no film cooling present the same correlations for convective heat transfer used in the previous section may be applied. An example of the network set-up for heat transfer without flametube wall film cooling is shown in Fig. 5.6.

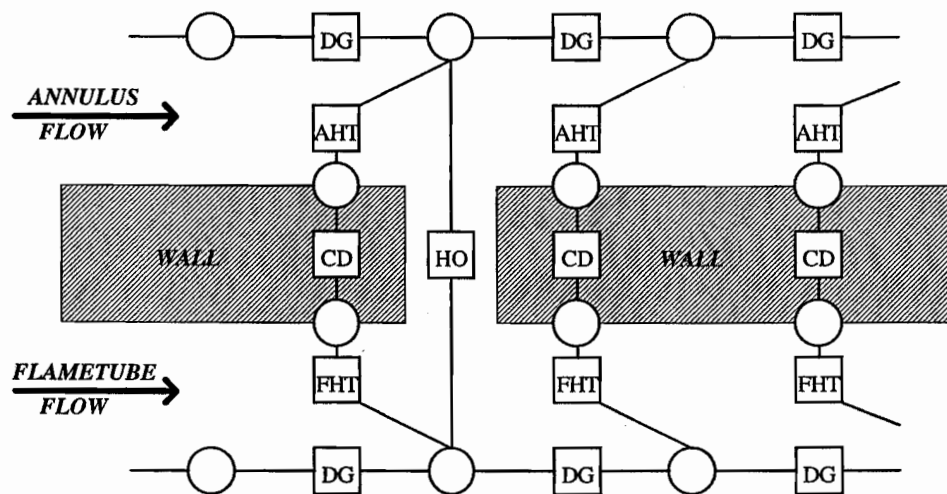


Figure 5.6. Network specification for conjugate heat transfer with no film cooling

The combustor wall temperature, in the presence of a wall cooling film, is computed as a function of heat transfer coefficient and the difference between the wall and adiabatic film temperature. The adiabatic film temperature is calculated from the film effectiveness,

$$\eta_f = \frac{T_g - T_f}{T_g - T_{fi}} \quad (5.16)$$

The film effectiveness is computed using a range of correlations for specific cooling feature types. An inversion of this equation is not used in calculating the film temperature since the rig tests used to obtain the data do not include the effects of changes in free stream conditions downstream of the film origin as found in combustors. An alternative correlation accounting for changes in downstream conditions adjacent to the films is,

$$T_f = T_{fp} \frac{\eta_f}{\eta_{fp}} + \left( 1 - \frac{\eta_f}{\eta_{fp}} \right) \frac{(T_g - T_{sp})}{2} \quad (5.17)$$

where the subscripts refer to,

$f$  = computed film value

$p$  = adjacent upstream value

$g$  = adjacent hot gas value, either the combusting gases, or for multiple film regions, the hot film adjacent the film of interest, at the same axial location

This formulation is also used in the presence of multiple films at the same axial location, such a scenario may arise in re-heat systems or regions of effusion cooling where a cooling device is placed upstream of the effusion patch to assist the growth of the film. In this case the gas temperature is taken to be the temperature of the fluid immediately adjacent to the cooling film, which may either be the bulk hot gas or another cooling film. The network solver allows the accumulation of up to three layered cooling films generated by different cooling features.

The diagram below (Fig. 5.7) illustrates how a single cooling film may be carried down the wall through succeeding FHT elements. The hole is simply represented as a HO element in this example. If a cooling slot is to be modelled the HO element would be followed by a DG element representing the slot, and the logic link would connect to the DG element in the exactly same way.

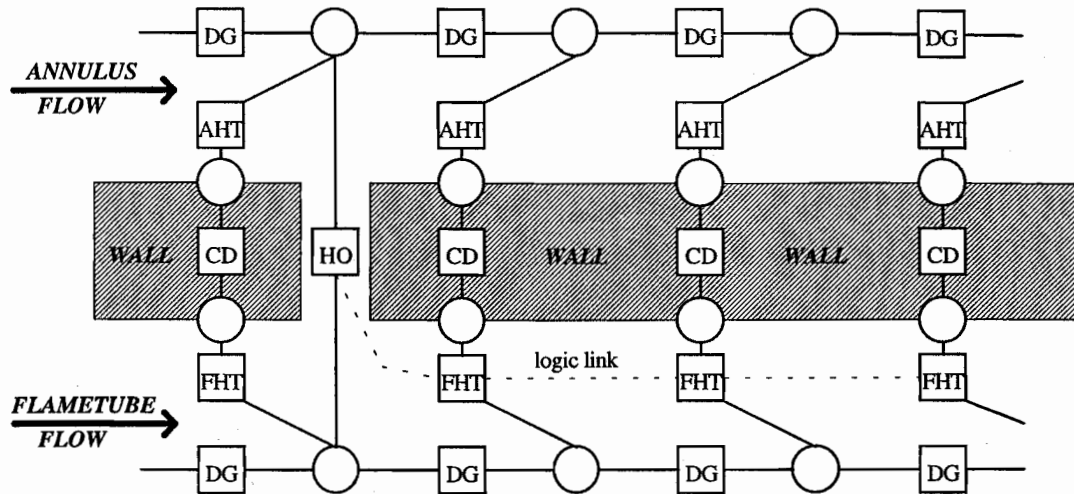


Figure 5.7. Network specification for conjugate heat transfer with one cooling film carried downstream along the wall

The film effectiveness is a function of the feature generating the film, as well as the distance downstream of the film and the free stream conditions. Each successive FHT element downstream will therefore contain a film with a reduced effectiveness in Fig. 5.7.

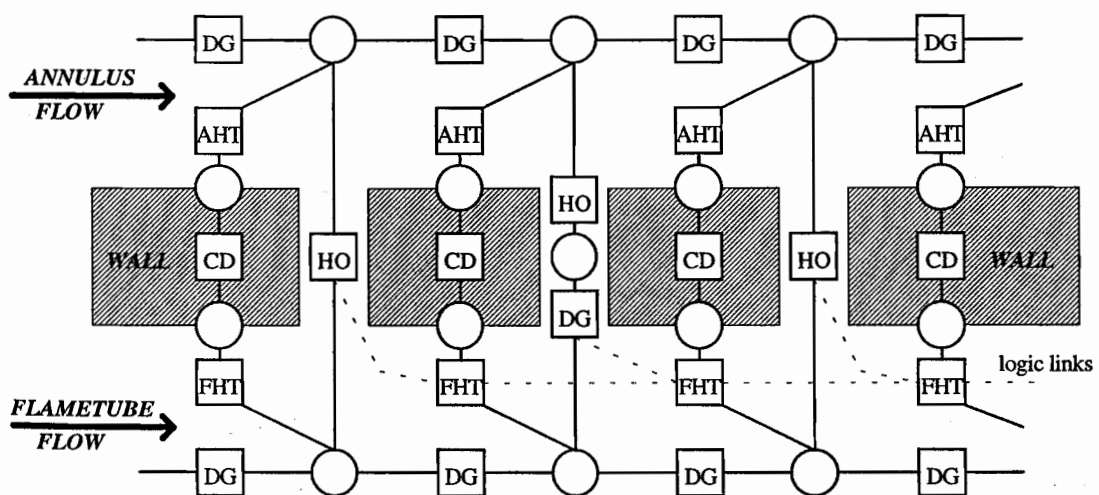


Figure 5.8. Network specification for conjugate heat transfer with three cooling films accumulated and carried downstream along the wall



Figure 5.8. shows the network layout for the case where three cooling streams are accumulated adjacent to each other and carried down the flametube. The second hole represents a cooling slot, hence the extra DG element, as described in the previous paragraph. At any given axial location the nearest upstream film cooling feature forms the inner most film adjacent to the wall.

The heat transfer in the presence of cooling films is dependent upon the device used to generate the film, and the flow conditions present. A number of correlations exist for taking into account the effect of a range of film cooling devices. The semi-empirical correlations may be either device specific, or more general, covering a range of cooling features. A large amount of data has been generated by the gas turbine industry for the purpose of predicting the film effectiveness in the flametube. The discussion below presents some of the popular correlations used to predict film cooling, and are available in the open literature.

Lefebvre (1983) described the existence of three flow regions associated with a cooling slot. The initial region within the slot designated the potential core where the wall and air temperatures are very similar, followed by a zone where the velocity profile is similar to that of a wall jet, and further downstream the flow may be represented by a turbulent boundary layer. A review of available correlations led Lefebvre (1983) to propose the following correlation for use in calculating cooling films generated by wall slots as illustrated in Fig. 5.9.

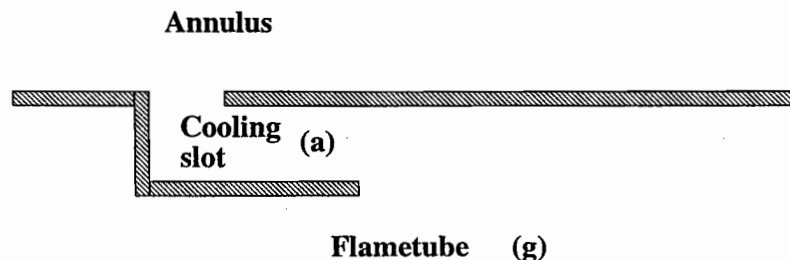


Figure 5.9. Slot nomenclature

Define the following,

$$\begin{aligned}
 m &= \frac{(\rho U)_a}{(\rho U)_g} \\
 Re_s &= \frac{\rho_a U_a S}{\mu_a} \\
 Re_x &= \frac{\rho_a U_a x}{\mu_a}
 \end{aligned} \tag{5.18}$$

where,

$S$  = depth of the cooling slot

$x$  = distance downstream of slot

For  $0.5 < m < 1.3$  a boundary layer formulation is used (Ballal and Lefebvre, 1972),

$$\begin{aligned}
 \eta &= 1.10 m^{0.65} \left( \frac{\mu_a}{\mu_g} \right)^{0.15} \left( \frac{x}{s} \right)^{-0.2} \left( \frac{t}{s} \right)^{-0.2} \\
 C_1 &= 0.069 \frac{k_a}{x} Re_x^{0.7} (T_{fi} - T_{w1})
 \end{aligned} \tag{5.19}$$

where,

$t$  = slot lip thickness

For  $m > 1.3$  a wall jet model formulation is used (Ballal and Lefebvre, 1972),

$$\begin{aligned}
 \eta &= 1.28 m^{0.65} \left( \frac{\mu_a}{\mu_g} \right)^{0.15} \left( \frac{x}{s} \right)^{-0.2} \left( \frac{t}{s} \right)^{-0.2} \\
 C_1 &= 0.10 \frac{k_a}{x} Re_x^{0.8} \left( \frac{x}{s} \right)^{-0.36} (T_{fi} - T_{w1})
 \end{aligned} \tag{5.20}$$

Simon (1986) developed a similar model which was capable of accounting for mass flow rates, turbulence levels and temperature gradients. The semi-empirical correlations were shown to predict experimental data within  $\pm 4\%$ . Equation (5.19) and Eq. (5.20) were

derived under conditions of low turbulence intensity with clean slots. A modified effectiveness accounting for blockage in machined-rings is (Sturgess, 1969),

$$\eta = 1.0 - 0.12\alpha^{0.65} \quad (5.21)$$

and for stacked-ring devices,

$$\eta = 1.0 - 0.094\alpha^{0.65} \quad (5.22)$$

where,

$$\alpha = \frac{x - x_p}{mS} \left( Re \frac{\mu_a}{\mu_g} \right)^{-0.15} \frac{A_o}{A_{eff}}$$

$x_p$  = potential core length

$A_o$  = slot outlet area

$A_{eff}$  = slot overall effective area

The turbulent mixing present in the region of the cooling film may rapidly destroy the effectiveness of the cooling film depending upon the level of turbulence. The effect may be accounted for by (Marek and Tacina, 1975),

$$\eta = \left( 1 + C \frac{x}{mS} \right)^{-1} \quad (5.23)$$

where,

$C$  = turbulent mixing coefficient, a range from 0.04 to 0.06 for turbulence intensity levels of 14% has provided representative results.

Although these empirical models ultimately provide a wall temperature based on the film effectiveness of the slot, they are less successful in evaluating competing slot designs. Sturgess (1986) and Sturgess and Pfeifer (1986) addressed this issue by developing a heuristic analysis to optimise slot configurations for particular operating conditions, providing a valuable tool to analyse the slot characteristics.

Impingement, transpiration, and effusion cooling are alternative types of wall cooling, which are very efficient in removing heat from the wall (Lefebvre, 1983). Folayan and Whitelaw (1977) evaluated the effect of impingement cooling on a combustor liner wall, and found a significant improvement in liner cooling when impingement cooling was applied to the annulus side, and slot film cooling applied to the flametube side of the liner wall. Andrews et al (1985) and Dabagh et al (1990) performed a detailed experimental and numerical study using a CFD code to produce and evaluate a heat transfer correlation for impingement cooling which may be written in terms of the Nusselt number as,

$$Nu = 1.05 Re^{0.72} \left( \frac{X}{D} \right)^{-0.72} \left( \frac{Z}{D} \right)^{-0.14} D^{0.28} Pr^{0.33} \quad (5.24)$$

where,

$X$  = hole pitch

$D$  = hole internal diameter

$Z$  = impingement gap

Transpiration cooling effectiveness typically relies on data from experiments for walls with given porosities. Smith (1966) used the following formulation for effectiveness to evaluate transpiration cooling within gas turbine combustion chambers,

$$\eta = 1 - \left[ 1 + \frac{G_c}{G_g} \frac{Re_g^{0.2}}{0.069} Pr_g^{2/3} \right]^{-3} \quad (5.25)$$

where,

$G_c$  = coolant mass flow per unit wall area

$G_g$  = hot gas mass flow per unit chamber cross-sectional area

Effusion cooling has become a popular method of lowering wall temperatures in regions of extreme thermal load. Laser drilling techniques allow very small holes to be drilled at high angles of attack to maximise the efficiency of effusion patches. Le Grives et al (1979) and Andrews et al (1986) studied the convective heat transfer within perforated

plates containing small diameter cooling holes. Features containing significant surface areas of heat transfer within the liner wall must be accounted for. Correlations were developed for evaluating the heat transfer from the liner wall to the hole surfaces within the wall. The formulation developed by Le Grives et al (1979) was,

$$Nu = \frac{0.51 Re^{0.6} Pr}{1 + 0.043(L/D)} \quad (5.26)$$

where,

$L$  = hole length

$D$  = hole diameter

The correlation of Andrews et al (1986) for effusion cooling is given by,

$$Nu = (0.27 Re^{0.476} + 0.023 Re^{0.8} C) Pr^{1/3} \quad (5.27)$$

where,

$$C = 0.13(L/D)^3 - 0.75(L/D)^2 + 1.04(L/D) + 2.24 \quad \text{for } L/D \leq 2$$

$$C = 1 - 49.3(D/L)^4 + 58.6(D/L)^3 - 26.5(D/L)^2 + 7.48(D/L) \quad \text{for } L/D > 2$$

Comparison between the two correlations developed by the two above authors was in good agreement. Dorignac and Vullierme (1995) performed an experimental analysis on effusion type injection geometries with one jet, one row of jets, and two rows of jets. A model was developed for the wall heat transfer combining a coefficient of heat transfer of the external flow with one for the injection flow, using the measured data gathered.



## 5.6.2 Radiation

Flame-side radiation is the most difficult heat flux component to estimate. Significant variations in gas composition and temperature combined with unknown concentrations of solid particles such as soot within the combustor limit the ability to compute flame radiation. The complexity of the physical process has led to approximations based upon experimental analysis.

The radiative heat transfer from a gas to a surrounding black wall is given by (Mellor, 1990),

$$R_1 = \sigma (\epsilon_g T_g^4 - \alpha_g T_{w1}^4) \quad (5.28)$$

where,

$\sigma$  = Stefan-Boltzmann constant =  $5.67 \times 10^{-8} \text{ W/(m}^2\text{K}^4)$

$\epsilon_g$  = gas emissivity at temperature  $T_g$ , relating to the emission of radiation from the gas to the wall

$\alpha_g$  = gas absorptivity at temperature  $T_w$ , relating to the absorption by the gas of radiation from the wall

In practice the wall will not be black. Typically wall emissivities are approximately 0.8 for metal liners, in which case 20% of the incident radiation will be reflected. The reflected radiation will be absorbed by the flame and any opposing wall. This effect is estimated by modifying the equation,

$$R_1 = \sigma \left( \frac{1 + \epsilon_{w1}}{2} \right) (\epsilon_g T_g^4 - \alpha_g T_{w1}^4) \quad (5.29)$$

The flame absorptivity is predicted, following an investigation over a wide range of parameters (Lefebvre, 1983), using,

$$\alpha_g = \varepsilon_g \left( \frac{T_g}{T_{w1}} \right)^{1.5} \quad (5.30)$$

In non-luminous flames, emissivity is dependent mainly upon the concentrations of water and carbon dioxide. For pressures below five atmospheres and fuel/air ratios weaker than stoichiometric the non-luminous gas emissivity may be predicted by (Lefebvre, 1983),

$$\varepsilon_g = 1 - \exp \left[ -290 P (ql_b)^{1/2} T_g^{-1.5} \right] \quad (5.31)$$

where,

$q$  = local fuel/air ratio

$l_b = 3.4 \frac{\text{volume}}{\text{surface area}}$  = effective path length across the flame (metres)

This correlation for gas emissivity has been used with some success to estimate gas emissivity at typical engine operating conditions (Mellor, 1990).

Typical jet fuels will contain soot particles, which will significantly effect the gas emissivity. A luminosity factor is introduced to account for this effect. Where the luminosity is relatively low, as in kerosene flames at low pressure, the gas emissivity may be rewritten as

$$\varepsilon_g = 1 - \exp \left[ -290 PL (ql_b)^{1/2} T_g^{-1.5} \right] \quad (5.32)$$

The luminosity factor is an empirical correction used to obtain agreement between experimental data and predicted values using the above equation. The experiments highlighted the dependency of the carbon/hydrogen mass ratio of the fuel, and to a lesser degree the combustor pressure, on the luminosity factor. A correlation that has been successfully applied is (Mellor, 1990),

$$L = 0.0691 (C/H - 1.82)^{2.71} \quad (5.33)$$



The application of simple empirical formulations to practical combustors is questionable. No account is made in the above correlations for the effects of atomisation and fuel distribution on soot formation, and hence gas radiation. A more realistic computation would require knowledge of the size, mass concentration and optical properties of the soot particles present in the flametube.

The conjugate heat transfer mechanism may be optimised for convergence knowing the form of the radiation term. Equation (3.23) becomes,

$$T_i = \frac{\left( \sum_{j=1}^J R_{i,j} T_{n_{i,j}} \right)_{\text{conduction}} + \left( \sum_{j=1}^J h_{i,j} T_{n_{i,j}} \right)_{\text{convection}} + \left( \sum_{j=1}^J r_{i,j} T_{n_{i,j}}^{2.5} \right)_{\text{radiation}}}{\left( \sum_{j=1}^J R_{i,j} \right)_{\text{conduction}} + \left( \sum_{j=1}^J h_{i,j} \right)_{\text{convection}} + \left( \sum_{j=1}^J r_{i,j} T_i^{1.5} \right)_{\text{radiation}}} \quad (5.34)$$

where,

$r_{i,j}$  = radiative heat transfer coefficient terms

## **5.7 Gas Turbine Combustor Case Studies**

### **5.7.1 Reverse Flow Combustor**

The reverse flow combustor was selected for the analysis because of the availability of experimental thermal paint data, and its unusual geometry, including reversing flow, extensive thermal barrier coating and double skin regions.

The network diagram is shown in Fig. 5.11. The dark outline is a not to scale representation of the combustor general features. The solid network of elements and nodes refers to the flow computational cells in which the flow and energy equations are solved. The dashed network represents the heat transfer sequence of elements and nodes required to model the overall heat transfer from the flametube through the liner to the annuli. Convection and radiation within the annulus and flametube was modelled using the AHT and FHT elements, respectively, as described in this chapter. The liner wall conduction was modelled using the CD elements.

The mass flow splits and pressure-drops for this combustor have been previously analysed in detail using the network solver (see Chapter 4). The heat transfer models allow for the effects of mixing, film cooling, thermal barrier coatings, and liner hole heat pick-up. The conjugate heat transfer through the double skin regions was also computed.

The normalised flametube bulk hot gas temperature is shown in Fig. 5.13. The profile was calculated using the constrained equilibrium model, constrained for CO and CO<sub>2</sub>. Efficiency curves for the vaporiser type combustor were used in computing these constraints. The mixing model was used to compute the fuel/air ratio used in the equilibrium calculation.

Figure 5.14 shows the temperature rise of the annulus air. The starting point for both curves is the pre-diffuser exit location (see Fig. 5.11). From this position the profiles are plotted in the clockwise and anti-clockwise directions (see Fig. 5.11 for directions).

The liner wall temperatures were computed throughout the combustor, and comparisons made to experimental thermal paint data (Gardiner, 1995). A sample section of the thermal paint is shown in Fig. 5.12. The different colour bands (shown as changes in shading here) were obtained by painting the annulus-side of the liner with a temperature sensitive paint. The paint changes colour as the temperature rises, and each colour band may be correlated to a mean wall temperature. Referring to Fig. 5.12, the region below the areas marked 'G' corresponds to the diffuser exit plane. The clockwise annulus is in the upward direction. The thermal paint photographs were used to generate the temperature band plots shown in Fig. 5.15 and Fig. 5.16.

External wall temperatures obtained from thermal paint photographs were compared to the temperatures calculated by the network solver (see Fig. 5.15). The solid line represents the computed values and the shaded region represents the temperature bands of the thermal paint data. The diagram shows reasonable agreement between the calculated and measured temperatures. Impingement of combustion gases on the upper liner wall from the primary ports (element '66' in Fig. 5.11) results in a rapid degradation of the film cooling layer developed by the static ring (elements '22' and '23' in Fig. 5.11). The dilution ports (element '16' in Fig. 5.11) destroyed any of the remaining film cooling downstream of the ports. These two effects increased the wall temperature in this region, and appear to be captured by the network solver. The hot spot on the forward/reverse flow cooling ring (element '26' in Fig. 5.11) was also captured by the network solver.

The effects of the static fed slot film cooling, effusion cooling and double skins were resolved by the network solver. The accuracy of the computation at the head of the flametube was limited by the range of validity of the heat transfer correlations.

The thermal paint data extended only as far as element '71' in Fig. 5.11. The effects of film cooling would become more pronounced as the heat transfer network 'density' increases. The resolution could be easily manipulated should more detailed information be required. The predicted metal temperatures reached a peak in the final section of the double skinned annulus region. This region is typically the most difficult to cool in a reverse flow combustor, as the pressure gradient adjacent to the flametube side of the liner wall will not allow a cooling film to be sustained adjacent to the wall.

The anti-clockwise annulus was cooled by Z-rings and thermal barrier coated. The results of a comparison for this section are shown in Fig. 5.16. Once again the comparison appeared reasonable between experimental and computational results.

The growth of the thermal boundary layer may have a significant effect on the efficiency of heat transport, and hence wall temperature. This effect was included in the analysis by explicitly specifying cooling lengths in some regions of the combustor.

Predicted wall temperatures varied with flametube gas temperature, and hence with the recirculation and mixing predicted within the network model. This proved significant in the treatment of the primary port recirculation. The amount of recirculation was simply estimated based upon knowledge of the combustor.

The broad bands of the thermal paint data limits the usefulness of the data in assessing the accuracy of the computed results. However, the effects of the various cooling features were captured by the network algorithm.

## 5.7.2 Annular Combustor

The second combustor analysed was a more conventional annular geometry. However, the wall cooling relies almost entirely on effusion. The mass flow split and pressure-drop characteristics of this combustor were analysed in detail using the network solver previously (see Chapter 4).

A network diagram of the combustor set-up is shown in Fig. 5.17. The nomenclature follows that of the previous combustor discussed. The network was set-up in such a way that corresponding numbers of elements appear in the flametube and annuli. This allows uniformity in computed surface area of heat transfer between the two regions. The effusion was broken into sections along the liner wall, and the heat transfer across each patch was computed. Z-rings at the head of the flametube carried their films over the downstream effusion patches on both the inner and outer liner walls.

The axial bulk flametube gas temperature is shown in Fig. 5.18. This temperature was computed using the mixing and recirculation models as well as efficiency curves for a spray type combustor.

The outer and inner annulus air temperature rise is plotted in Fig. 5.19. A higher temperature rise was observed in the outer annulus. Most of this temperature rise occurred toward the combustor exit where the mass flow in the outer annulus was significantly lower than that in the inner annulus, explaining the relatively rapid rise in temperature in the outer annulus.

The predicted outer annulus liner wall temperatures were compared to experimentally obtained thermal paint bands, as shown in Fig. 5.20 (Lowe, 1995). The hot-side predictions fell for the most part within the bands of the thermal paint data. The cold-side computed temperatures appear slightly high for the 2.5mm thick liner wall. This indicates that the heat pick-up terms may be too low within the wall.

The inner annulus liner wall temperature comparisons are shown in Fig. 5.21. The hot-side wall temperatures fell within the range of the thermal paint, apart from two peaks. Once again the temperature difference across the wall was slightly lower than that predicted by the thermal paint data.

The development of the thermal boundary layer was taken to be impeded along the length of the effusion patch, as air was being constantly bled from the boundary layer by the effusion holes. This retarding of boundary layer development significantly effects the cold-side wall temperature since the effectiveness of the heat transfer mechanism is far superior in developing flows compared to developed flows.

The comparison indicated the network solver to be over predicting the liner wall temperatures, with the temperature gradient through the wall being slightly under-predicted. The simulation illustrated the need for film cooling effectiveness correlations for modelling large effusion patches. The ability of the current model, which employs a modified transpiration sub-model, to capture effusion heat transfer effects appears limited.

A further limitation of the conjugate heat transfer computation is the simplicity of the radiation model. Bulk gas emissivities based upon bulk fuel/air ratio, bulk pressure, bulk temperature, mean beam length and a soot luminosity factor represent a gross simplification of the physical process, with no account for radial or circumferential variation of the properties.

## **5.8 Conclusions**

A conjugate heat transfer scheme was developed and incorporated into the combustor network solver. The adiabatic flame temperature calculation was corrected to include the effects of heat loss. A one-dimensional and two-dimensional conduction model was developed for calculating either radial or combined radial and axial heat fluxes. The accurate specification of thermal conductivities was found to be critical in calculations including materials of low thermal conductivity such as thermal barrier coatings. Semi-empirical models for convection and radiation were included to compute the heat transfer from the liner walls to the annuli.

The combined effects of convection and radiation were included in the conjugate heat transfer mechanism on the flametube side of the liner wall. Film cooling effects were included in the flametube convection calculation. Up to three adjacent films, generated by similar or different liner features could be included in the calculation. Cooling films generated by slots, lipped-rings, Z-rings, transpiration patches, and effusion patches were included in the calculation. Internal liner wall heat pick-up through convection in features with significant areas of heat transfer, such as effusion patches, were included in the computation. The radiation calculation within the flametube made use of a simple semi-empirical model to account for the effects of soot at elevated pressures and temperatures.

Simulations within reverse flow and annular combustors illustrated the versatility of the heat transfer scheme in modelling double skin regions, film cooling, and multi-layered liner walls. Converged solutions were obtained in less than one minute, in both cases, on the Silicon Graphics Indy Workstation.

The wall temperature predictions were compared to experimentally obtained thermal paint data for a reverse flow and annular combustor. The network solver was able to predict the wall temperatures and their trends with reasonable accuracy, although further

improvements to the code should enhance this ability. The effects of various cooling features and flow conditions in predicting the wall temperatures were captured by the solver.

Thermal paint data is limited in its usefulness as a validation tool. The wide ranges of the temperature bands only provide a general basis for wall temperature comparisons. Unfortunately, obtaining a higher resolution of wall temperature is a difficult and costly task. The use of thermocouples on the cold side of the liner wall would nevertheless provide a more reliable basis for wall temperature comparisons. The measurement of hot-side flametube wall temperatures is currently limited to the use of thermal paint due to the extreme operating conditions within this environment.

The accuracy of the conjugate heat transfer scheme was limited by the sub-models employed. The radiation component of heat flux was significant within the combustor flametube region. The sub-model for the radiative flux prediction was based on a simple empirical relationship. The accuracy of such a formulation at the elevated pressures of modern gas turbine combustors is questionable. The relationship also makes limiting assumptions on the simplicity of the flametube geometry. A more accurate radiation scheme should improve the predicted radiative flux, and hence wall temperature.



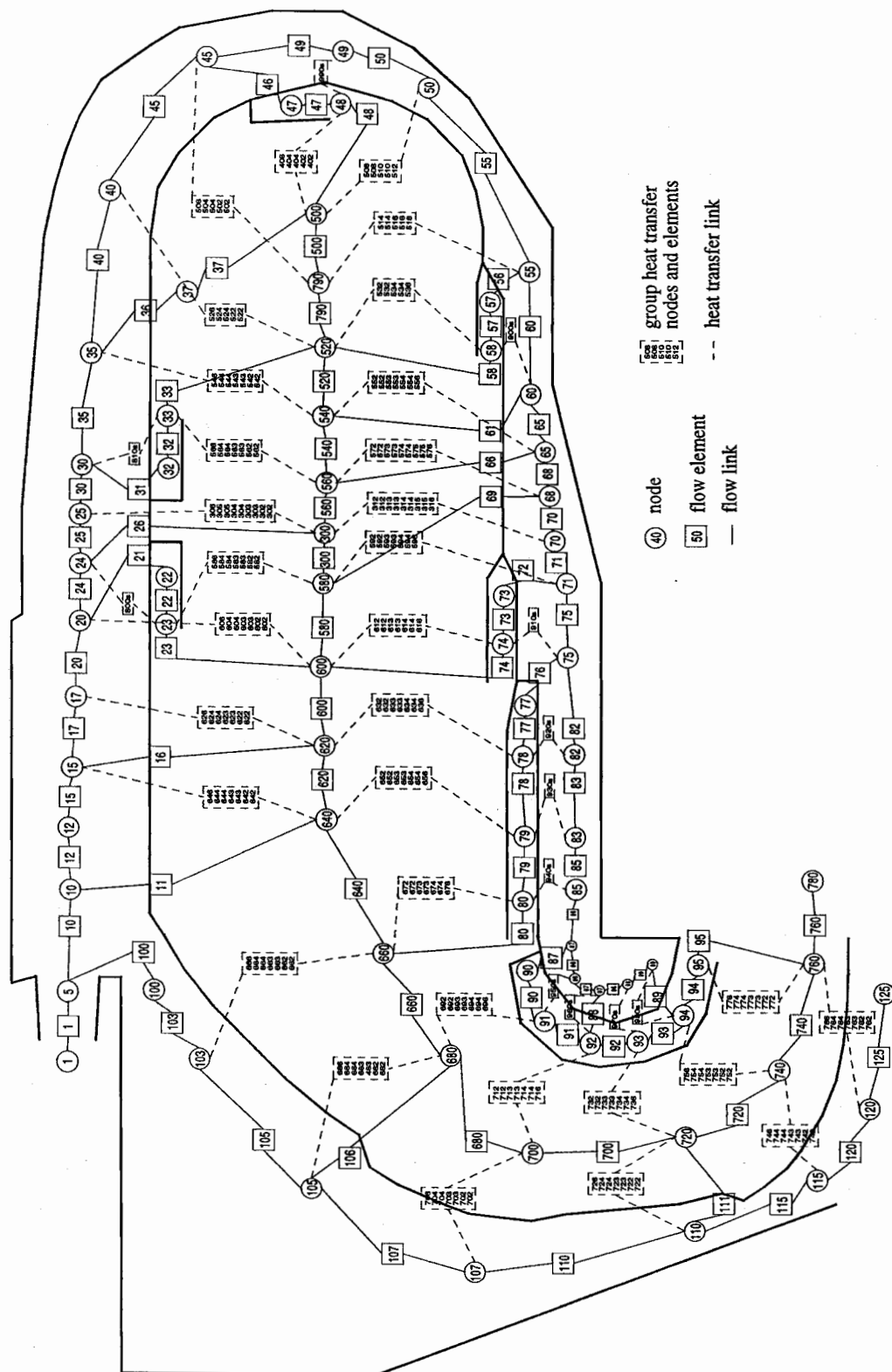


Figure 5.11. Network diagram for reverse flow combustor, including heat transfer elements

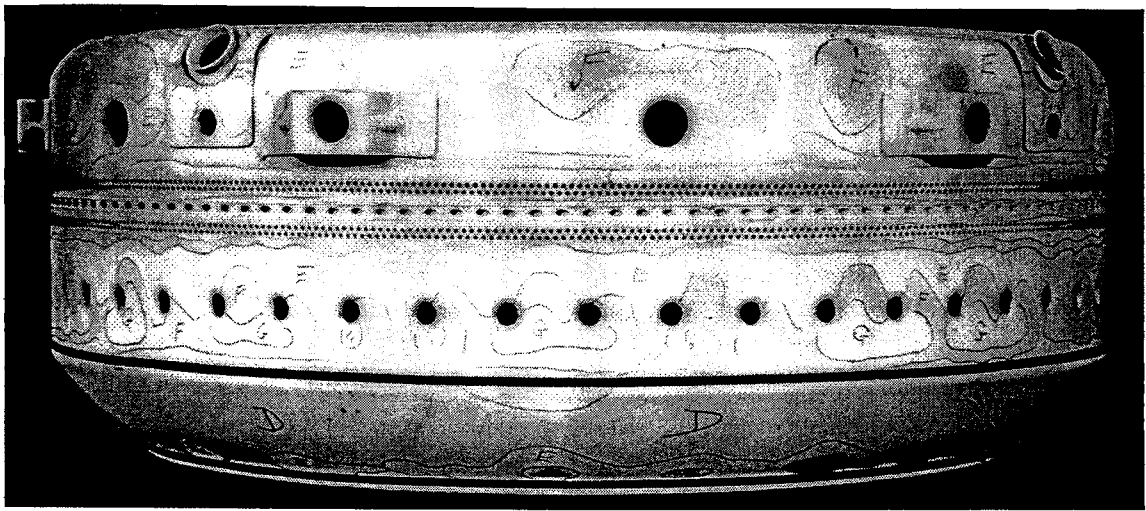


Figure 5.12. Sample experimental thermal paint results for the reverse flow combustor

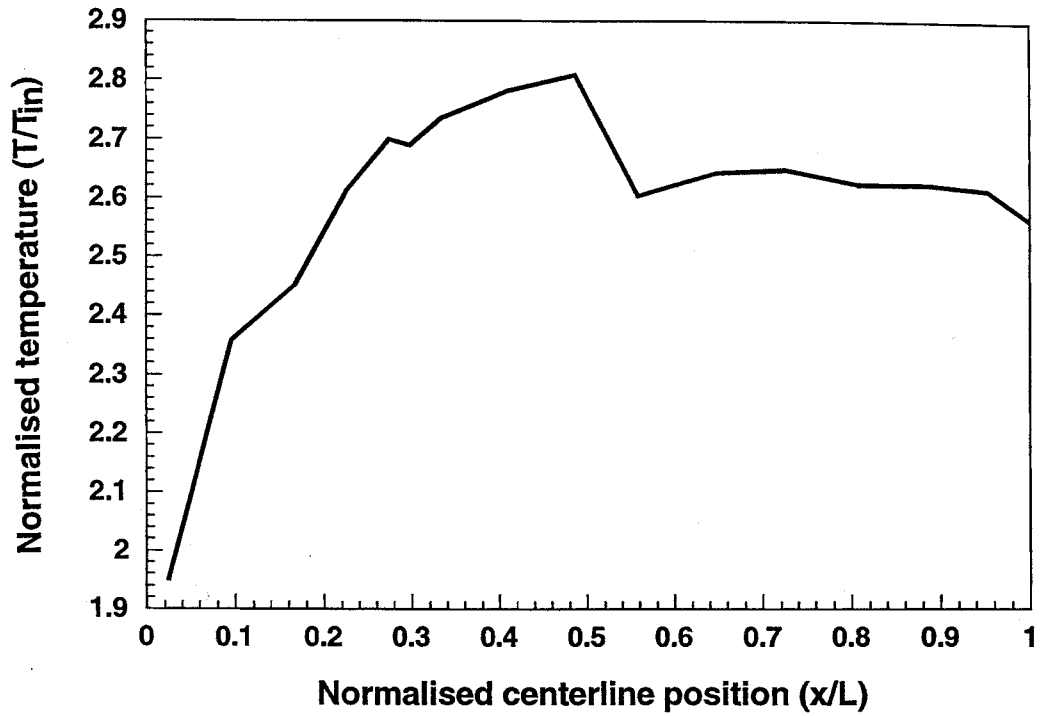


Figure 5.13. Reverse flow combustor flametube axial bulk gas temperature

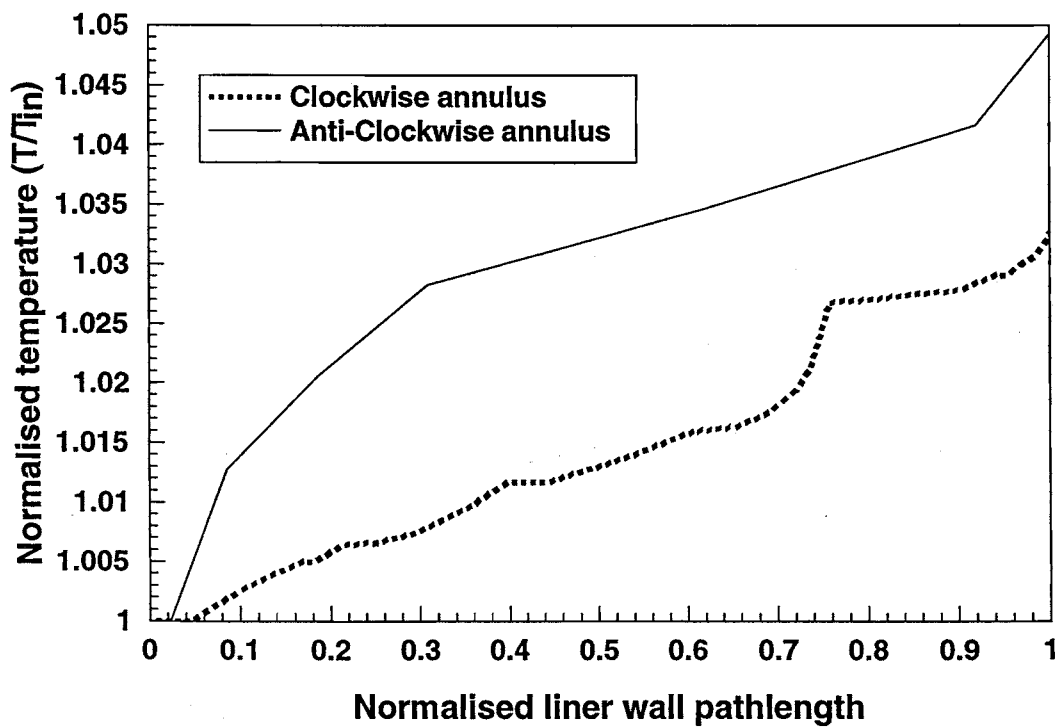


Figure 5.14. Reverse flow combustor clockwise and anti-clockwise annuli bulk air temperature

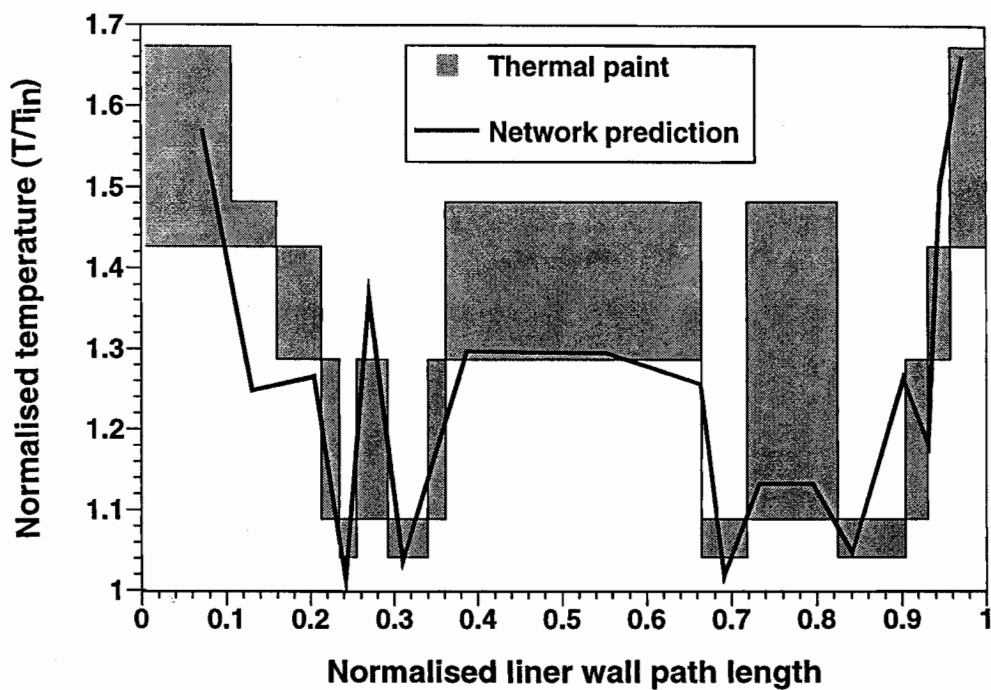


Figure 5.15. Reverse flow combustor clockwise cold-side liner wall experimental and predicted temperature comparison

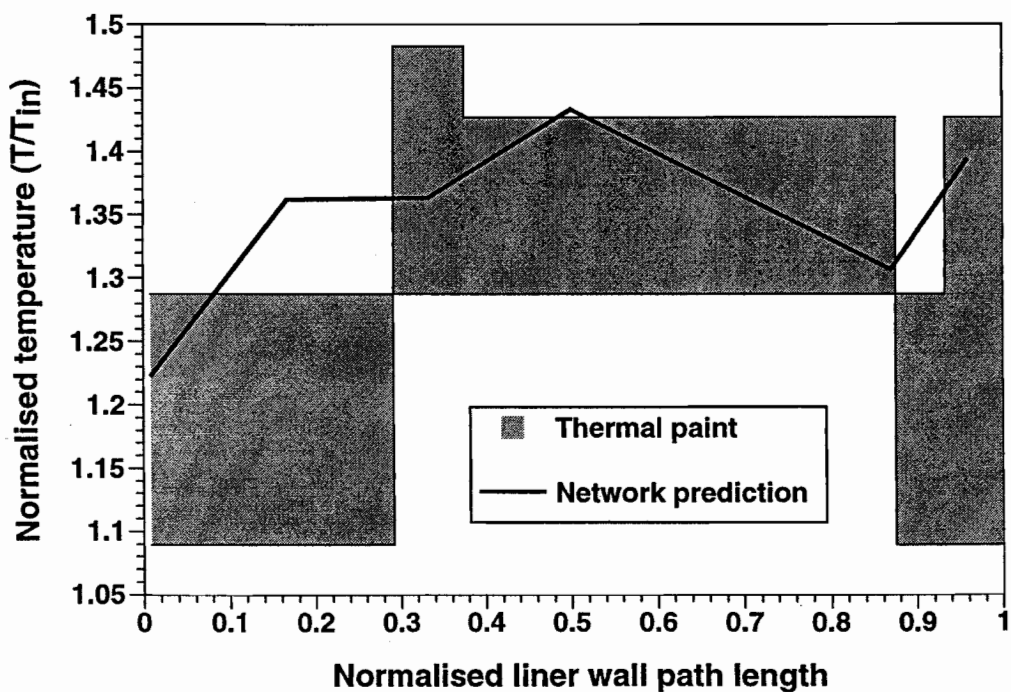


Figure 5.16. Reverse flow combustor anti-clockwise cold-side liner wall experimental and predicted temperature comparison

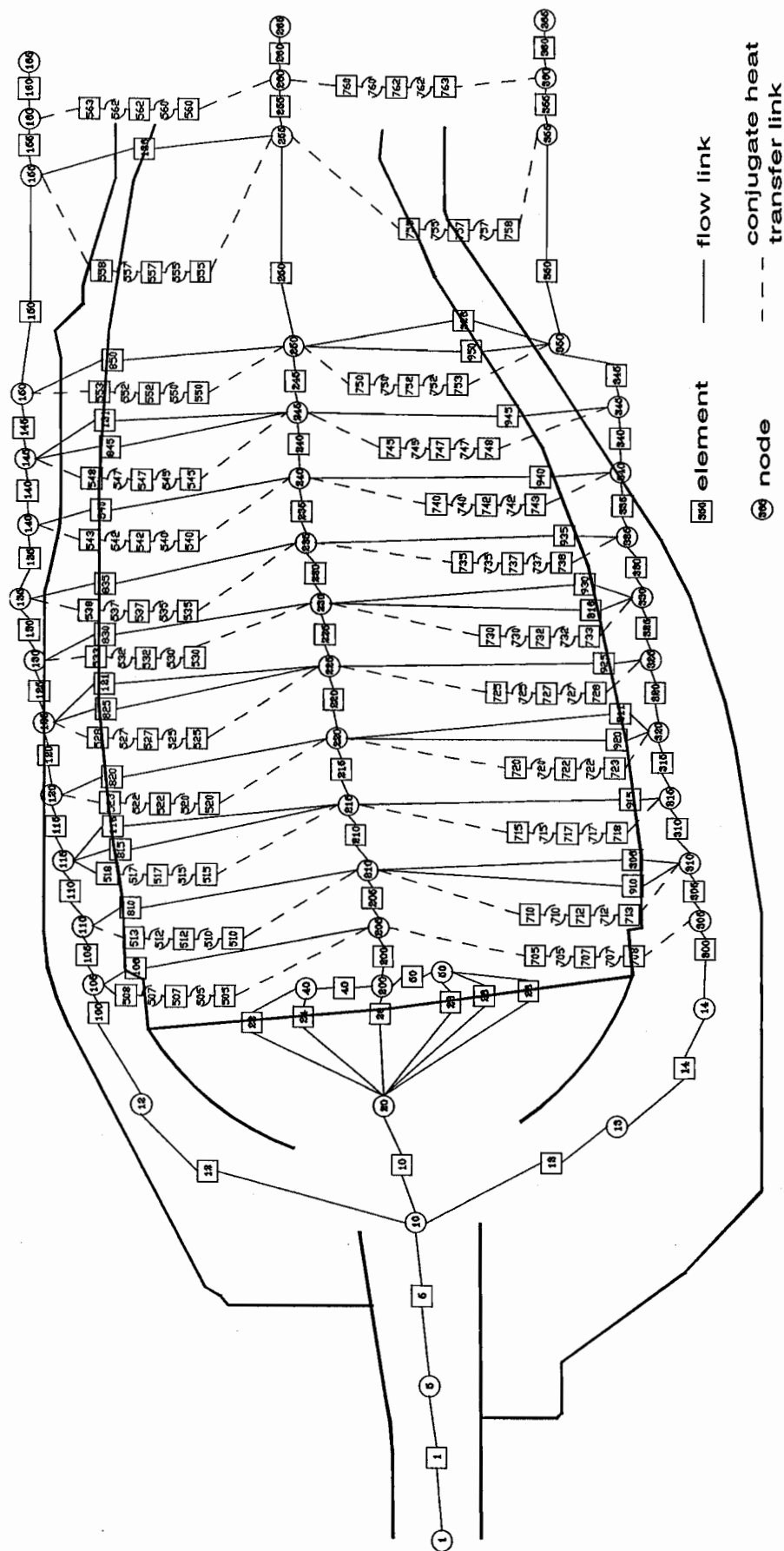


Figure 5.17. Annular combustor network diagram including heat transfer network

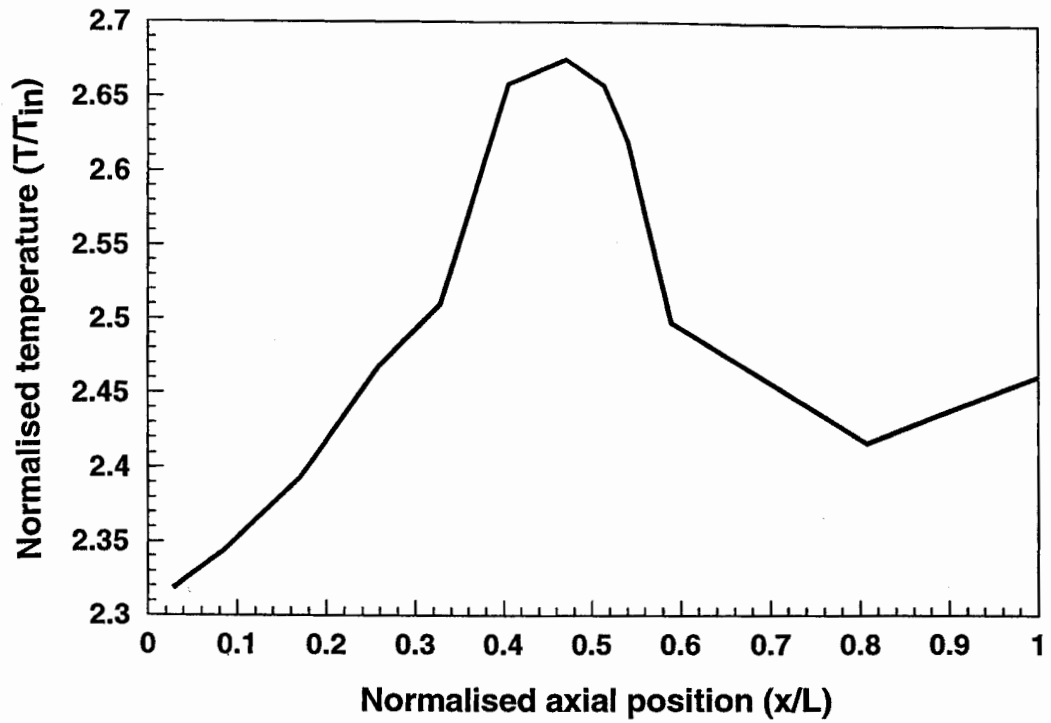


Figure 5.18. Annular combustor flametube axial bulk gas temperature

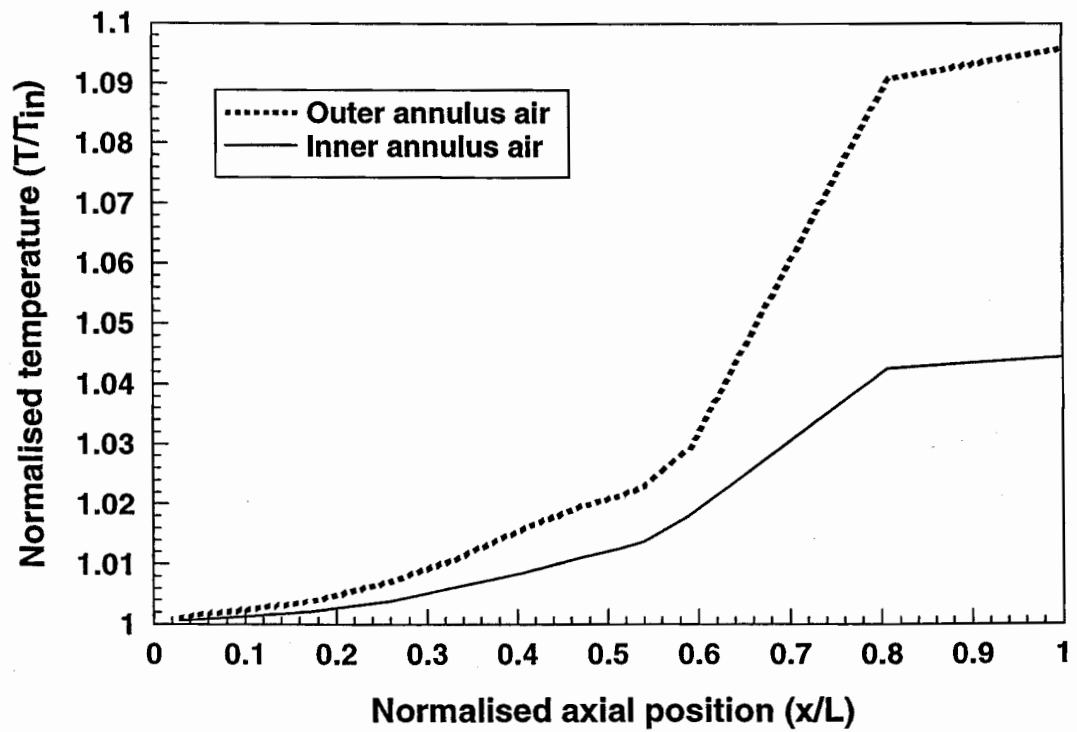


Figure 5.19. Annular combustor annuli axial bulk air temperature

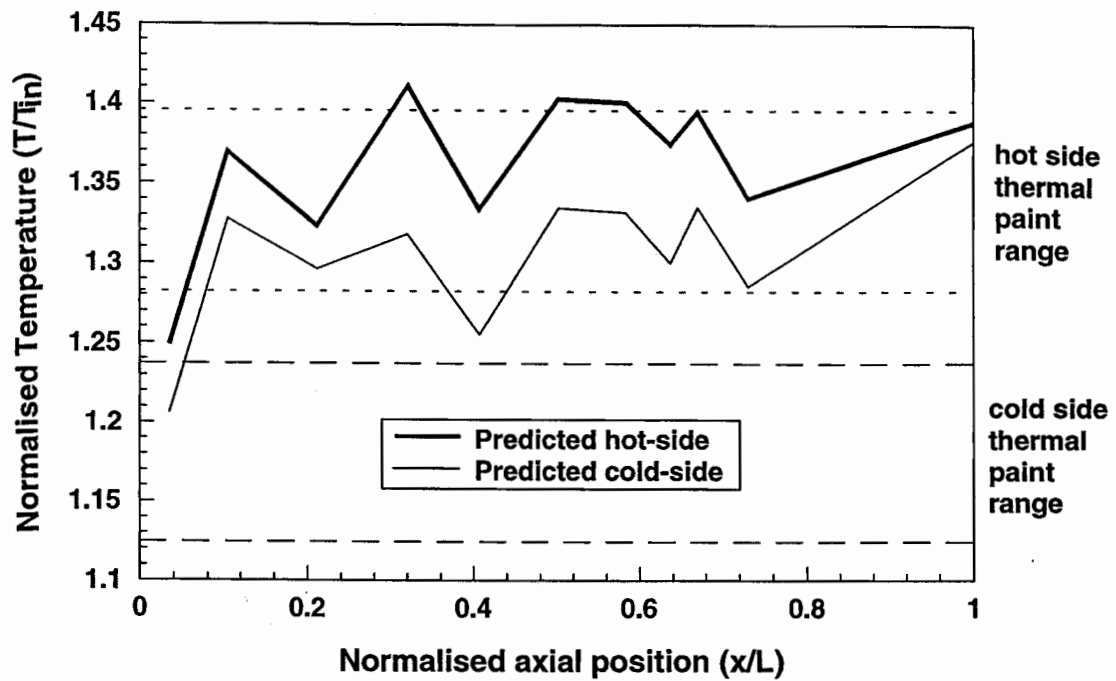


Figure 5.20. Annular combustor outer annulus liner wall hot and cold side temperatures

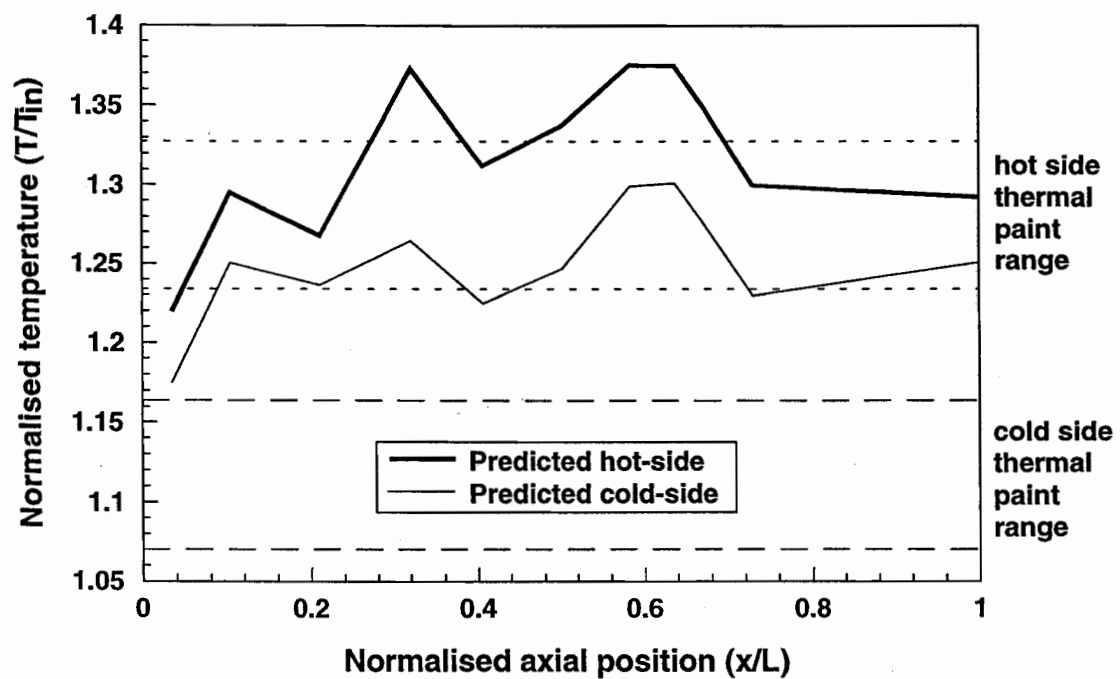


Figure 5.21. Annular combustor inner annulus liner wall hot and cold side temperatures

## **6. Combustor Radiation Modelling**

### **6.1 Introduction**

Previous comparisons with experimental results in a reverse flow and annular geometry have shown qualitative agreement (see Chapter 5) but highlighted the need for a more broadly applicable radiation procedure. An effort is made to extend the predictive radiative capability of the code beyond simple conventional empirical radiation correlations, improving the flexibility and accuracy of the radiation calculation to that of the underlying network solver.

Radiation is the most complex mode of heat transfer to model. It is governed by a complex integrodifferential equation, which must be simplified to solve economically. Radiative heat transfer from the flame and combustion products to the surrounding walls may be computed given knowledge of the radiative properties and temperature distributions within the medium. However, these requirements are generally unknown and therefore the total energy and radiative energy conservation equations must be coupled.

A number of solution strategies exist for radiative heat transfer. The simplest make use of semi-empirical correlations to simulate the radiation in a one-dimensional domain (see Chapter 5). The application of these models require sweeping assumptions concerning system geometry, gas temperature and radiative properties. The accuracy of the correlations is limited within complex geometries and at elevated pressures, regimes beyond those used to originally formulate the relationships.

More complex models take direct account of the geometry. A number of models have been developed over the past 40 years. Ultimately, they all provide a similar result. However, the various models present significantly different numerical requirements. A



balance must be made between solution accuracy and solution economy. An informative and extensive discussion of these techniques is presented in Siegel and Howell, 1992 and Modest, 1993. A brief description of these methods is presented below.

Statistical methods such as the Monte Carlo scheme provide solutions approaching those of the exact solution (Viskanta and Menguc, 1987). The method has been successfully employed in complex geometries and accounts for spectral effects. Since random number generators are a key feature, statistical errors and the lack of guaranteed convergence may cause problems. However, the key factor limiting the use of this method is the excessive computational time required for practical engineering calculations.

The zonal method has been widely used for solutions to practical problems. The surface and volume of the domain are divided into a number of zones, each containing an isothermal gas with constant properties. Direct exchange area factors between the surface and volume elements must be computed, and the total exchange area calculated. This becomes a time consuming task as the geometry increases in complexity. A further difficulty arises for an absorbing and emitting medium as the attenuation of radiation along a path connecting area elements must be accounted for in the calculation of exchange areas. Nevertheless, radiative transfer by the zonal method has been used extensively in the past as solution times were relatively fast compared to alternative methods (Viskanta and Menguc, 1987). An advantage of this form of algorithm is the ease with which it may be represented in a network notation (Oppenheim, 1954), in a way similar to the set-up of the existing network solver.

Radiation intensity is dependent upon location, the direction of radiation propagation, and wavelength. The problem is complicated by the angular dependence of the intensity. If the assumption is made that the intensity is uniform over specified solid angles the problem may be simplified, and the integrodifferential radiative transfer equation is reduced to a series of coupled linear differential equations. This procedure forms the basis of the flux methods (Viskanta and Menguc, 1987). They include multiflux models, moment methods, spherical harmonics ( $P_N$ ) approximations, and discrete-ordinate

models. Essentially, they only differ in the derivation of weighting coefficients for the intensities in each direction. Although these methods provide accuracy with computational economy they involve mathematical complexity.

Hybrid solution strategies combine the best of existing models. The discrete transfer method is such a model, combining elements of the zonal, Monte Carlo, and discrete ordinate methods (Viskanta and Menguc, 1987). The discrete transfer method has been selected to solve for the radiative transfer in this analysis, and will be discussed in detail in the sections which follow.

## **6.2 Radiation Modelling in Gas Turbine Combustors**

A large proportion of the heat transferred to the liner wall from the hot combusting gases and particles within the combustor flametube is by radiation. It follows therefore that an accurate liner heat balance may only be performed with the assistance of a reliable radiation model. A further advantage of an accurate radiation model is the improvement in the prediction of gas temperature, a necessity for evaluating pollutant emissions.

The radiation is made up of two components. The first is the non-luminous radiation emitted by gases. Typically, the radiation emitted by  $\text{CO}_2$  and  $\text{H}_2\text{O}$  dominate the other gas species up to approximately 3000K (Lefebvre, 1984), thus allowing a simplification in the number of species represented in the radiation calculation.

The second component of radiation is the luminous radiation emitted by particles of soot within the flame. The contribution to radiation of the soot is dependent upon the size and concentration of particles in the domain. Typically, significant amounts of soot are produced in the fuel-rich regions of the flame within the primary zone. At the elevated pressures present in modern gas turbine combustors soot particles attain a sufficient size to radiate as black bodies.

Accurate predictions of radiative flux are dependent upon the distribution of temperature and radiative properties, and any useful model must take these distributions into account. A number of examples exist of the implementation of radiation models to compute radiative flux in gas turbine combustors. Rizk and Mongia, 1991, were able to achieve satisfactory wall temperature results using simple semi-empirical correlations for radiative transfer in a gas turbine combustor. The correlations were implemented as part of a three-dimensional analysis. Kapat and Yang (1992) performed a detailed analysis on the heat loss through the gas turbine combustor liner using a zonal model to account for non-luminous radiation. Menguc et al, 1985 successfully employed a spherical harmonics ( $P_1$  and  $P_3$ ) model on a cylindrical enclosure at gas turbine combustor conditions. It was

necessary to make some assumptions in obtaining a soot concentration profile, allowing the effects of differing profiles to be evaluated.

Carvalho et al, 1985, presented a three-dimensional model of a 'can' combustion chamber. The discrete transfer method was employed to model the radiative transfer within the can. However, the procedure was not validated with experimental or existing numerical data. A similar piece of work on a 'can' combustor (Carvalho and Coelho, 1989) used the discrete transfer method to examine the effect of pressure on radiative fluxes. A simple conjugate heat transfer scheme was coupled to the CFD solution to directly calculate wall temperatures from the computed internal heat fluxes. However, the accuracy of the results was not evaluated.

Bai and Fuchs, 1995, performed a sensitivity study of different models for the interaction between turbulence and combustion, within gas turbine combustors. The discrete transfer method was used to compute the radiative heat source terms. This followed from earlier work (Bai and Fuchs, 1994) in which the effect of radiation on mean gas temperature was evaluated using DT. The mean temperature profile exhibited errors of up to 10% when the effects of radiation were neglected. The effect of turbulent temperature fluctuations in the heat radiation were also evaluated. As expected the turbulent fluctuations were significant where there were very large amplitude fluctuations. The mean values of temperature presented a reasonable approximation when the levels of temperature fluctuation were globally low.

## **6.3 Discrete Transfer Radiation Model**

### **6.3.1 Introduction**

The discrete transfer (DT) method combines the advantages of other radiation procedures to provide a numerically exact and flexible solution algorithm. It allows for simple coupling to the existing overall flow and heat transfer solver. A further important advantage is the ease with which radiation properties models can be incorporated into the DT calculation.

DT involves tracing representative rays from one surface to another through the region of interest. An intensity distribution is calculated along each ray as it passes through the domain. The intensities of the individual rays are summed at the various wall locations to give the net radiative heat flux. The accuracy of the calculation will obviously depend upon the number of rays projected at each point. The more complex the geometry and flowfield within the domain, the more rays that will be required to describe the radiative transfer through the domain. A disadvantage of the DT method is that too few rays may miss important information within the domain or on the boundary geometry. This is known as the 'ray effect'. Large numbers of rays may be required to accurately predict the radiative transfer in complex domains.

### **6.3.2 Numerical Algorithm**

The method involves tracing representative rays from one surface to another in the domain. The nature of radiation requires that this be a three-dimensional procedure. The intensity distribution along each ray is computed by solving a discretisation of the equation of radiative transfer. The transfer equation for thermal radiation along a ray in a direction  $s$  may be written as, (Lockwood and Shah, 1981),

$$\frac{dI}{ds} = -(k_a + k_s)I + k_a \frac{E_g}{\pi} + \frac{k_s}{4\pi} \int_{4\pi} P(\Omega, \Omega') I(\Omega') d\Omega' \quad (6.1)$$

where,

$I$  = radiant intensity in the direction  $\Omega$

$s$  = distance in the  $\Omega$  direction

$E = \sigma T_g^4$  = black body emissive power of the gas at temperature  $T_g$

$\sigma$  = Stefan-Boltzman constant

$k_a$  = gas absorption coefficient

$k_s$  = gas scattering coefficient

$P(\Omega, \Omega')$  = probability that the incident radiation in the direction  $\Omega'$  will  
scattered into the increment of solid angle  $d\Omega$  about  $\Omega$

In the case of infrared radiation from flames, the radiation wavelength is generally greater than the soot particle diameter, and the scattering of radiation by soot particles may be assumed negligible (De Ris, 1979). Diameters of soot particles in hydrocarbon flames typically range in diameter between approximately 0.005 $\mu\text{m}$  and 0.3 $\mu\text{m}$  (Siegel and Howell, 1992). Soot particles may take the form of spherical particles, or conglomerate into large masses and strings. The properties of such large and non-uniform shapes differs significantly from those of simple spheres, and the emission from cylindrical type particles is significantly higher than that from spheres (Tien and Lee, 1982). Using Mie theory (Siegel and Howell, 1992) the scattering cross section is a function of  $(\pi D/\lambda)^4$  and the absorption cross section is dependent upon  $(\pi D/\lambda)$ . At the temperatures typical of a combustion system the radiation is generally of a wavelength,  $\lambda$ , of 1 $\mu\text{m}$  or higher. Hence, for small diameter,  $D$ , particles the scattering will be negligible compared to the absorption coefficient. For larger agglomerates and chains of particles this is not necessarily true. It is not currently feasible to predict the size, shape and properties of such particles. The assumption is made that the soot is made up of small spherical particles in this study, and so scattering is neglected.

If scattering is assumed negligible the scattering term in Eq. (6.1) may be removed, making the calculation more economical. The formulation then reduces to,

$$\frac{dI}{ds} = -k_a I + \frac{k_a \sigma T_g^4}{\pi} \quad (6.2)$$

Given a representative ray the intensity distribution can be calculated along it. This equation can be integrated to give the recurrence relationship,

$$I_{n+1} = \frac{\sigma T_g^4}{\pi} (1 - e^{-k_a \Delta s}) + I_n e^{-k_a \Delta s} \quad (6.3)$$

where,

$I_n$  = ray intensity entering control volume

$I_{n+1}$  = ray intensity leaving control volume

$\Delta s$  = distance travelled along ray in the control volume

Thus the intensity may be calculated stepwise as the ray passes through successive control volumes within the domain. The initial intensity is calculated assuming that the surface is a gray, Lambert, one,

$$I_0 = \frac{q_+}{\pi} = (1 - \varepsilon_w) \frac{q_-}{\pi} + \varepsilon_w \frac{\sigma T_w^4}{\pi} \quad (6.4)$$

where,

$q_+$  = energy flux outgoing

$q_-$  = energy flux incident

$\varepsilon_w$  = surface emissivity

$T_w$  = surface temperature

Then at any given point on the boundary the incoming heat flux due to radiation is,

$$q_- = \int_{2\pi} I_w(\Omega) \cos \theta d\Omega \quad (6.5)$$

where,

$I_w$  = incident intensity

$\theta$  = angle between the ray direction  $s$  and the normal to the surface

$d\Omega$  = associated solid angle

Clearly,  $q_-$  may only be calculated given knowledge of the initial intensity of the ray impinging on the surface of interest. Thus the process is iterative with updated initial ray intensities used at the beginning of each new iteration loop.

The net wall radiative heat flux is simply the difference between the energy flux away from the surface and towards the surface,

$$q_w = q_- - q_+ \quad (6.6)$$

The net radiation energy change in a control volume must be accounted for in the overall flow solution procedure's energy conservation equations. A source term is used to represent this change in energy. Once the ray intensities have been resolved the calculation of the source terms follow with relative ease. The radiation source to a particular control volume for a single ray may be expressed as,

$$S = dA \cos \theta \Delta \Omega (I_{n+1} - I_n) \quad (6.7)$$

where,

$dA$  = the surface area associated with the ray launch point

The contribution of each ray passing through the control volume must be summed to produce the overall control volume source term.



The convergence in the solution of the energy equation is improved by modifying Eq. (3.23) to minimise the numerator as follows,

$$T_i = \frac{\left[ \sum_{j=1}^J R_{i,j} T_{n_{i,j}} \right]_{\text{conduction}} + \left[ \sum_{j=1}^J h_{i,j} T_{n_{i,j}} \right]_{\text{convection}} + \left[ (\epsilon q_-)_i \right]_{\text{radiation}}}{\left[ \sum_{j=1}^J R_{i,j} \right]_{\text{conduction}} + \left[ \sum_{j=1}^J h_{i,j} \right]_{\text{convection}} + \left[ (\epsilon \sigma T^3)_i \right]_{\text{radiation}}} \quad (6.8)$$

### 6.3.3 Quadrature Formulation

The integral in Eq. (6.5) is replaced by a numerical quadrature in the application of the DT algorithm. In this way Eq. (6.5) is rewritten as,

$$q_- = \sum I_w(\Omega) \cos \theta \Delta \Omega \quad (6.9)$$

The discretisation of the solid angle in Eq. (6.9) over a hemisphere has been addressed by a number of authors. Conventionally the solid angle hemisphere is discretised by equal division of polar and azimuthal angles (Shah, 1979), and Eq. (6.9) becomes,

$$q_- = \sum_{i=1}^{N_\theta} \sum_{j=1}^{N_\phi} I_w(\theta_i, \phi_j) (\cos \theta_i) (\sin \theta_i) (\sin \Delta \theta) \Delta \phi \quad (6.10)$$

where,

$\theta$  = polar angle

$\phi$  = azimuthal angle

$N_\theta$  = number of rays in the  $\theta$  direction, over the range  $0 < \theta < \pi/2$

$N_\phi$  = number of rays in the  $\phi$  direction, over the range  $0 < \phi < 2\pi$

$\Delta \theta$  = solid angle increment in the  $\theta$  direction

$\Delta \phi$  = solid angle increment in the  $\phi$  direction

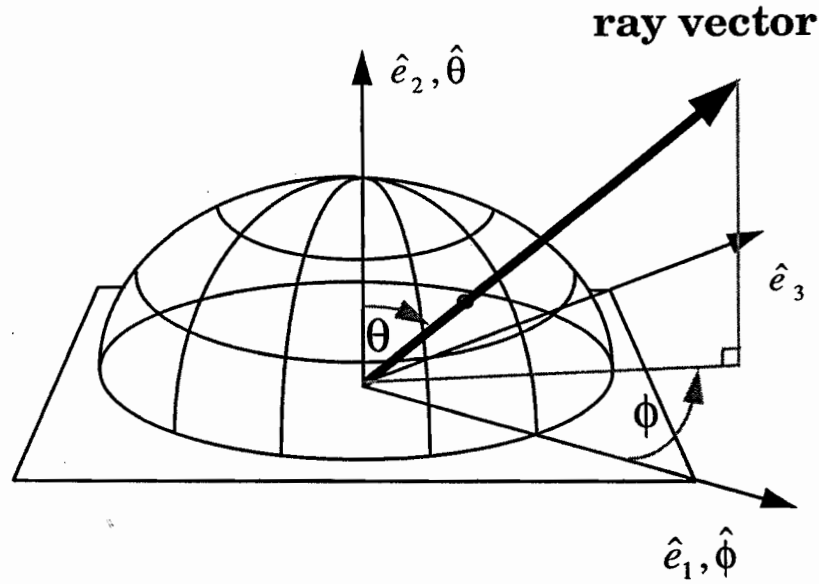


Figure 6.1. The discretisation of a solid angle hemisphere with equal divisions of polar and azimuthal angles

For constant  $\Delta\theta$  and  $\Delta\phi$  in Eq. (6.10) the weightings are proportional to  $\sin 2\theta$  which produces a bias to rays closest to  $\theta = \pi/4$ . A further limitation is that rays at an angle close to the surface have the same weighting as rays close to the normal direction from the surface. Improvements can be made by ensuring a more even distribution of ray directions.

The discretisation of the solid angle was addressed by Cumber, 1995. Cumber presented two alternative quadrature formula. The first, Newton-Cotes type formula, assumed that the incident intensity is evaluated at the corners of each hemispherical element, with a bilinear intensity distribution. A second, Gaussian type quadrature, integrated intensity distributions which were quadratic in  $\phi$  and cubic in  $\theta$ . For a limited number of rays Cumber was able to show an improvement on results obtained using Eq. (6.10).

A more detailed analysis has been performed by Bressloff et al (1995), who compared results over a range of ray numbers. A more uniform distribution of ray directions was

obtained by realigning the co-ordinate axis, moving the poles away from the surface normal, and discretising the solid angle hemisphere to give approximately equal areas. The more uniform distribution of ray directions was obtained through the following formulation,

$$q_- = \sum_{i=1}^{N_\theta} \sum_{j=1}^{N_\phi} I_w(\theta_i, \phi_j) \left( \sin \frac{\Delta\phi}{2} \right) \cos \phi_j \left[ \Delta\phi - (\sin \Delta\theta) (\cos 2\theta_i) \right] \quad (6.11)$$

A shortcoming of both these discretisations is the inability to launch a ray normal to the surface. An additional discretisation was formulated (Bressloff et al, 1995) to account for a ray launched along the surface normal, using the original co-ordinate system as shown in Fig. 6.1,

$$q_- = \pi I_w(\theta_i, \phi_j) \sin(\Delta\phi)^2 \quad (6.12)$$

### 6.3.4 Ray Tracing

The most complicated part of the DT calculation is in the ray tracing. The lengths of every segment of each ray through the control volumes making up the domain must be computed before any intensity calculation can be performed. The ray tracing calculation must account for the control volume geometry typical of the solver being used. Although the calculation is complex and time consuming it need only be performed once prior to the main solution procedures.

Ideally, the ray tracing procedure developed in this work should be compatible with the network solver for which it was developed. The flametube geometry of the network solver consists of a series of duct sections which combine to describe the complete flametube. The advantage of the network solver is that all these duct sections are independent of each other. Unfortunately, this presents a problem when it comes to

radiation since for a radiation calculation the geometry and position of the duct sections is crucial to the radiative transfer. In effect every part of the flametube will 'see' every other part of the flametube, requiring a large amount of information to be transferred between all the independent duct sections.

The problem is overcome by assuming each duct surface may be described by an equation. A further simplifying assumption of axisymmetry significantly reduces the amount of information that need be specified by the user. In this way each duct section requires the specification of only a single surface. Most combustors of interest match the requirement of axisymmetry. However, it should be noted that non-axisymmetric geometries can be modelled using the procedure developed here by implementing some simple extensions to the underlying logic.

A final assumption is that all the surfaces of each duct are flat with no curvature, allowing the flametube to be described by a series of equations of planes, cylinders, and cones. This assumption may also be removed by including equations for toroidal sections if required at a later time.

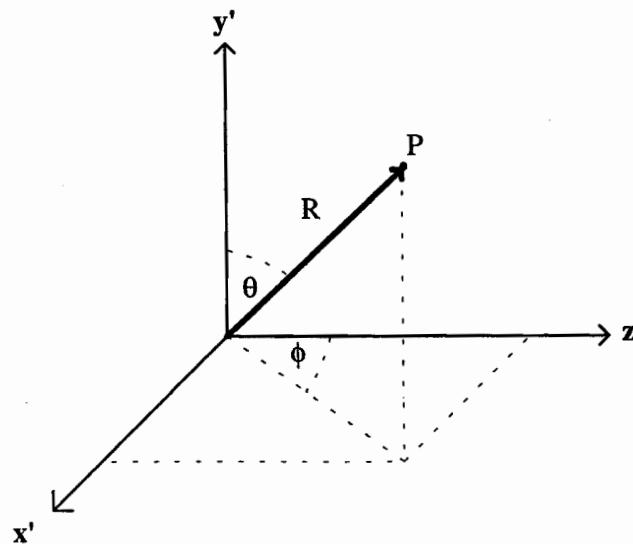


Figure 6.2. Description of transformation from spherical to rectangular co-ordinate system

Rays are launched from the axial midpoint of every boundary surface. The number of rays launched is user defined. The equations describing the rays are generated in spherical co-ordinates about the midpoint, which is specified as the origin of the local frame of reference (see Fig. 6.2).

The equations may be transformed from spherical to Cartesian co-ordinates as follows (Kindle, 1950),

$$\begin{aligned}x' &= R \sin \theta \sin \phi \\y' &= R \cos \theta \\z' &= R \sin \theta \cos \phi\end{aligned}\tag{6.13}$$

where the ray is represented by the length  $R$  from the origin to point  $P$ . The local co-ordinate system is then translated and rotated into the global co-ordinate system, see Fig. 6.3 below. In this way all the rays and surfaces are described in the exact same global Cartesian co-ordinate system.

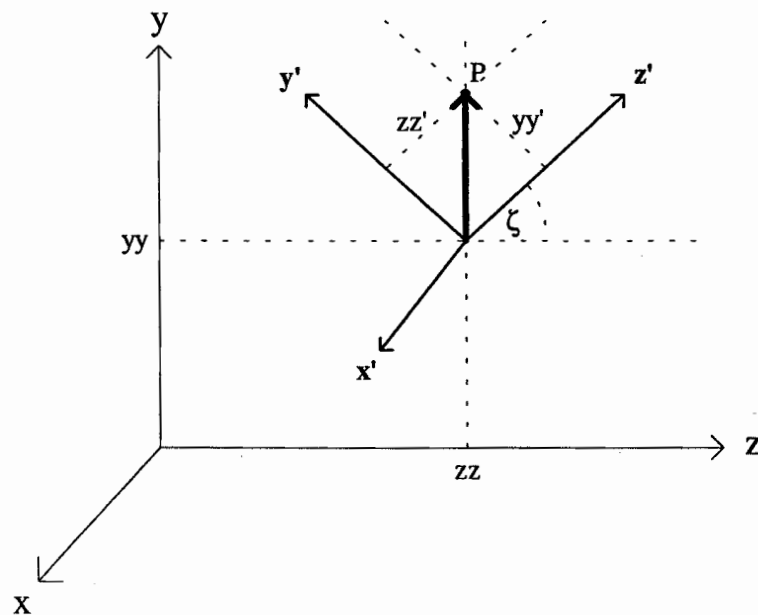


Figure 6.3. Description of rotation and translation from local to global co-ordinate system

The translation and rotation is represented as,

$$\begin{aligned}x &= x' \\y &= yy + yy' \cos \zeta + zz' \sin \zeta \\z &= zz + zz' \cos \zeta - yy' \sin \zeta\end{aligned}\tag{6.14}$$

The equations describing the ray are now solved by simple substitution, and the result, written in parametric form in the global co-ordinate frame is,

$$\begin{aligned}x &= (\sin \theta \sin \phi)t \\y &= yy + (\sin \theta \cos \phi \sin \zeta + \cos \theta \cos \zeta)t \\z &= zz + (\sin \theta \cos \phi \cos \zeta - \cos \theta \sin \zeta)t\end{aligned}\tag{6.15}$$

Thus a simple description of the ray is obtained dependent only upon its origin (the boundary surface mid-points) and the user specified polar and azimuthal angles.

The boundary surfaces must also be described by equations in the global Cartesian co-ordinate frame of reference. The equations describing a plane, cylinder and cone may be written as follows, with the axis of symmetry falling on the z-axis,

Equation of a plane:

$$z = \text{constant}\tag{6.16}$$

Equation of a cylinder:

$$x^2 + y^2 = a^2\tag{6.17}$$

where,

$a$  = radius of the cylinder

Equation of a cone:

$$x^2 + y^2 = a^2 \left( \frac{z-L}{L} \right)^2 \quad (6.18)$$

where,

$a$  = radius at intersection with xy-plane at origin of z-axis

$L$  = distance along z-axis from origin to vertex of cone

Equations have been presented for the description of each element of the ray tracing procedure. The information is used to calculate the positions of the intersects between rays and planes, cylinders, and cones. Each intersect must be checked to ensure it meets the conditions of validity, i.e. the intersect is within the domain, and the ray never passes outside the domain. Knowing the intersects of each ray, the ray path length across each control volume is finally obtained.

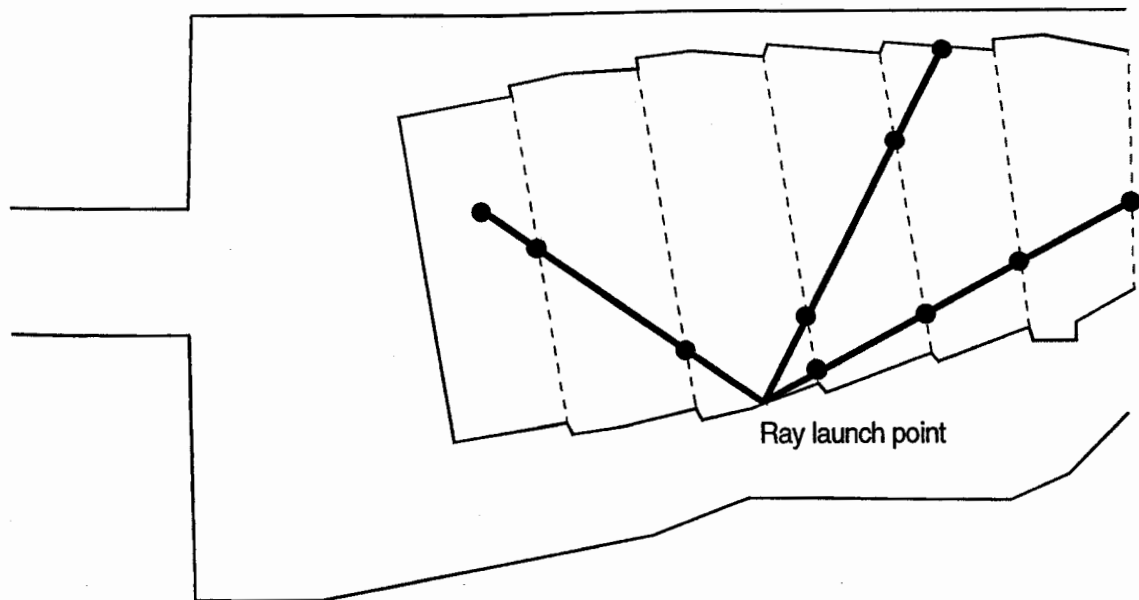


Figure 6.4. Ray tracing in a typical annular gas turbine combustor

Fig. 6.4 above illustrates the ray-tracing in a typical annular combustor. The rays are launched from the mid-point of a bounding wall. The rays travel three dimensionally up,

down and across the flametube until striking a boundary. Each intersection (control volume boundary) must be computed, and the distance travelled by the ray across each control volume calculated. Assuming each control volume to be at a specified temperature and absorption coefficient the DT calculation uses the computed ray pathlength across each control volume to obtain the change in intensity of the ray as it passes through a control volume.

The ray tracing procedure is further complicated in meeting the requirement that regions containing individual duct sections may be 'pasted' together with rays passing freely between them, a requirement to model double annular combustors for example.



## **6.4 Properties Modelling**

### **6.4.1 Introduction**

Radiative properties of combustion gases present the most difficult obstacle to performing an accurate, reliable radiation calculation. The radiative properties are dependent upon temperature, pressure, composition, wavelength, and path length. The concentrations of the constituent species must first be predicted. This initial step typically introduces the largest errors into the calculation. The radiative properties of the constituents of each control volume are then calculated, which may include gross approximations especially in the soot properties calculation. The only alternative to performing these calculations is to match measured absorption coefficients to the combustor of interest, obviously greatly limiting the predictive capabilities of the code. The aim of the models developed in this work is to offer the user the capability of either specifying or computing the radiative properties.

Enormous amounts of experimental work have addressed this subject, resulting in a number of different correlations and solution procedures. The sections below address the problems inherent in modelling the properties of gases and particulates, and finally presents a strategy for simulating their combined effects.

### **6.4.2 Gas Properties**

The radiative transfer from an opaque wall can often be represented by a simple model of gray (having radiative properties which do not vary with wavelength) emission, absorption and reflection. Unfortunately, the same assumption cannot be made about a molecular gas, since the radiative properties vary significantly across the gas spectrum, and are strongly dependent upon wavelength.

Gases release energy as a result of the transitions between vibrational and rotational energy levels within the molecules. This results in radiation concentrated in spectral lines and bands. Absorption occurs over small frequency intervals due to the broadening of the absorption lines (Tien and Lee, 1982). The total gas radiation is a function of the absorption of these individual lines, and the line radiation is effected by the line profile. A broadened spectral line profile is dependent upon temperature, pressure, optical pathlength, as well as the intrinsic properties of the radiating gas.

A number of models exist for predicting gas absorption-emission ranging from the relatively simple to the extremely complex. A compromise between accuracy and simplicity must be made, bearing in mind the overall accuracy of the radiation procedure. A detailed discussion and comparison of methods has been performed by Bressloff et al, 1996.

The most accurate, and computationally intensive models are the line-by-line methods. High resolution spectral data is used to compute integrated line intensities and spectral absorptivities. Narrow and Wide Band models are able to calculate mean band parameters using line-by-line and experimental data with a significant saving in computational time while maintaining good accuracy. Faster models rely on curve fitting strategies to spectrally calculated total properties. The weighted-sum-of-gray-gas model is such a model which has become popular due to its accuracy, efficiency, and flexibility (Modest, 1991, and Denison and Webb, 1995). A similar method is that of using curve fits to the total absorptivity-emissivity of the gas volumes. These too offer speed and accuracy, and are generally sufficient for practical engineering applications (Modest, 1993).

When selecting an empirically based model the range of applicability of the models must be carefully considered. The operating environment of a gas turbine combustor at elevated pressure severely restricts the selection of a gas properties model. Most of the work in this area has been performed at atmospheric pressure, or at least an order of

magnitude lower pressure than that found in a typical gas turbine combustor. Unfortunately the effects of pressure broadening cannot be ignored, and models which account for them must rely on extrapolation.

In a system containing combustion gases the emission from the molecules of  $\text{H}_2\text{O}$  and  $\text{CO}_2$  dominate, and the effects of the remaining constituents are small enough to be assumed negligible. Hottel (1954) and Hottel and Sarofim (1967) generated the first extensive charts for the calculation of total emissivity, based upon experimental measurements, for water vapour and carbon dioxide. The charts have proven accurate over a wide range of conditions but have been shown to be inaccurate in regions where the data was extrapolated.

More recent work based on the integration of spectral data has improved the accuracy of such charts (Leckner, 1972). Modak (1979) developed a simple accurate method for calculating emissivities and absorptivities of  $\text{CO}_2$ ,  $\text{H}_2\text{O}$  and soot. The inclusion of soot is of obvious interest, as this is the most important component in gas turbine combustor properties calculations. Further discussion on the subject appears in the next section. The only limitation of the work is that it was performed at atmospheric pressure. Farag (1982) developed approximate emissivity models with slight improvements on the predictions of Leckner over a limited range for atmospheric pressure. Docherty (1982) presented a review of techniques used in solving the gas emissivity and recommended Leckner's model over a wide range of conditions. In the case where the emissivity of a mixture of a greater number of gases than  $\text{H}_2\text{O}$  and  $\text{CO}_2$  is required the exponential wide band model of Edwards and Balakrishnan (1973) was selected as it includes the correction necessary to account for band overlap of the gas constituents. Steward and Kocaeffe (1986) developed algebraic models for the total properties of  $\text{H}_2\text{O}$  and  $\text{CO}_2$  and their mixtures, based upon band emission data. The results compared well with those of Leckner and Modak at atmospheric pressure.

A key issue in the calculation of radiative properties is the system pressure. Edwards and Matavosian (1984) developed scaling rules for calculating the emissivity of gases at

elevated pressures, and presented data for particular gas mixtures. Lukash (1970) presented an analysis, based upon a just overlapping spectral line model, for predicting gas properties at elevated temperature and pressure.

The discussion presented above illustrates the amount of work performed on this topic. The successful models eventually all provide the same results over their range of applicability. Leckner's (1972) model is selected for use here as it has the advantage of simplicity, efficiency, and is applicable over a wide range of operating conditions, including those of a gas turbine combustor.

Modest (1993) recommended the use of Leckner's model and presented a clear and precise layout of the procedure, which is summarised below. The model is presented in greater detail in the original work of Leckner (1972). Leckner's formulation has a maximum error of 5% for water vapour, and 10% for carbon dioxide compared with the spectrally integrated intensities, for temperatures above 400 K.

First, a zero-partial-pressure emissivity is defined,

$$\varepsilon_0 = \exp \left[ \sum_{i=0}^M \sum_{j=0}^N c_{ji} \left( \frac{T}{T_0} \right)^j \left( \log_{10} \frac{p_a L}{(p_a L)_0} \right)^i \right] \quad (6.19)$$

where,

$T$  = gas temperature

$T_0 = 1000$  K

$p_a$  = gas partial pressure

$L$  = path length

$(p_a L)_0 = 1$  bar cm

$c_{ji}$  = correlation constants shown in Tables 1 and 2 below

The emissivity for different pressure conditions is given by,

$$\frac{\varepsilon}{\varepsilon_0} = 1 - \frac{(a-1)(1-P_E)}{a+b-1+P_E} \exp \left[ -c \left( \log_{10} \frac{(p_a L)_m}{p_a L} \right)^2 \right] \quad (6.20)$$

where,

$P_E$  = effective pressure (defined in Tables 1 and 2)

$a, b, c, (p_a L)_m$  = correlation parameters given in Tables 1 and 2

In mixtures containing both  $\text{CO}_2$  and  $\text{H}_2\text{O}$  the bands partially overlap, and a correction factor is introduced to account for this effect,

$$\Delta\varepsilon = \left[ \frac{\zeta}{10.7 + 101\zeta} - 0.0089\zeta^{10.4} \right] \left[ \log_{10} \frac{(p_{\text{H}_2\text{O}} + p_{\text{CO}_2})L}{(p_a L)_0} \right]^{2.76} \quad (6.21)$$

where,

$$\zeta = \frac{p_{\text{H}_2\text{O}}}{p_{\text{H}_2\text{O}} + p_{\text{CO}_2}}$$

Then the total emissivity of a gas mixture of  $\text{H}_2\text{O}$  and  $\text{CO}_2$  is,

$$\varepsilon_{\text{H}_2\text{O}+\text{CO}_2} = \varepsilon_{\text{H}_2\text{O}} + \varepsilon_{\text{CO}_2} - \Delta\varepsilon \quad (6.22)$$

$M, N$	2,2
$c_{00} \dots c_{0M}$	-2.2118      -1.1987      0.035596
$\vdots \quad \quad \vdots$	0.85667      0.93048      -0.14391
$c_{N0} \dots c_{NM}$	-0.10838      -0.17156      0.045915
$P_E$	$\frac{1}{p_0} \left( p + \frac{2.56 p_a}{\sqrt{t}} \right)$
$\frac{(p_a L)_m}{(p_a L)_0}$	$13.2 t^2$
$a$	$2.479$ $t < 0.75$ $1.888 - 2.053 \log_{10} t$ $t > 0.75$
$b$	$1.10 t^{-1.4}$
$c$	0.5
$T_0 = 1000 \text{ K}, \quad p_0 = 1 \text{ bar}, \quad t = \frac{T}{T_0}, \quad (p_a L)_0 = 1 \text{ bar cm}$	

Table .1. Correlation parameters for calculating the total emissivity of water vapour

$M,N$	2,3			
$c_{00} \dots c_{0M}$	-3.9893	-2.7669	-2.1081	0.39163
$\vdots \quad \quad \quad \vdots$	1.2710	1.1090	1.0195	-0.21897
$c_{N0} \dots c_{NM}$	-0.23678	0.19731	-0.19544	0.044644
$P_E$	$\frac{1}{p_0}(p+0.28p_a)$			
$\frac{(p_aL)_m}{(p_aL)_0}$	$0.054t^{-2}$		$t < 0.7$	
	$0.225t^2$		$t > 0.7$	
$a$	$1+0.1t^{-1.45}$			
$b$	0.23			
$c$	1.47			
$T_0 = 1000 \text{ K}, \quad p_0 = 1 \text{ bar}, \quad t = \frac{T}{T_0}, \quad (p_aL)_0 = 1 \text{ bar cm}$				

Table .2. Correlation parameters for calculating the total emissivity of carbon dioxide

### 6.4.3 Soot Properties

The luminous component of radiation may far outweigh the non-luminous radiation in some areas of the combustor flametube, especially in the fuel rich pockets within the primary zone. At the high pressures present within the gas turbine combustor the soot particles attain sufficient size to radiate as black bodies (Lefebvre, 1984). When a parallel beam of radiation passes through a domain of particles the strength of the beam decreases exponentially as follows (Lefebvre, 1984),

$$\frac{I_{n+1}}{I_n} = \exp(-K\Delta s) \quad (6.23)$$

Assuming as previously (in formulation of DT) that the scattering is negligible,  $K$  is equivalent to the absorption coefficient. If the emissivity is equal to the absorptivity, the emissivity may be defined as (Lefebvre, 1984),

$$\varepsilon_s = \frac{I_n - I_{n+1}}{I_n} \quad (6.24)$$

Substituting from Eq. (6.23) the formulation may be rewritten as,

$$\varepsilon_s = 1 - \exp(-K\Delta s) \quad (6.25)$$

where,

$$K = C_0 \frac{f_v}{\lambda} \quad (6.26)$$

$$C_0 = \frac{36\pi nk}{(n^2 - k^2 + 2)^2 + 4n^2 k^2}$$

$f_v$  = soot volume fraction

$n, k$  = infrared-average optical constants of soot particles



The constant  $C_0$  depends only on the soot index of refraction. Using this simple  $1/\lambda$  wavelength dependence the Planck-mean and Rosseland-mean extinction coefficients may be calculated as (Modest, 1993),

$$K_P = \frac{3.83 f_v C_0 T}{C_2}, \quad K_R = \frac{3.60 f_v C_0 T}{C_2} \quad (6.27)$$

where,

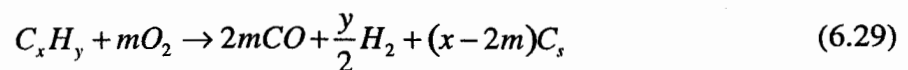
$$C_2 = \text{Planck's second constant} = 0.0143879 \text{ mK}$$

The Planck mean coefficient, for optically thin situations, differs less than 6% with the Rosseland-mean value, for optically thick situations. The use of an average has been suggested for all optical regimes (Modest, 1993),

$$K_R = \frac{3.72 f_v C_0 T}{C_2} \quad (6.28)$$

The above formulation is only applicable to situations where very small soot particles exist. The extinction coefficient will increase with increasing particle sizes. The value of  $C_0$  is taken to be 7.0 (Menguc et al, 1985). Values range from 3 to 10 (Siegal and Howell, 1992) depending on the fuel type and test conditions.

The only parameter not yet considered is the soot volume fraction. The process of soot formation and oxidation is extremely complex. Quantitatively accurate methods for calculating soot production within the operating regimes of a gas turbine combustor have yet to be developed. Soot is not an equilibrium product of combustion (Srivasta, 1982). It depends upon physical processes such as atomisation, evaporation and turbulent mixing as much as the chemical kinetics. Soot appears in regions of the combustor where there is insufficient oxygen to oxidise the fuel to CO and H<sub>2</sub> (Lefebvre, 1984),

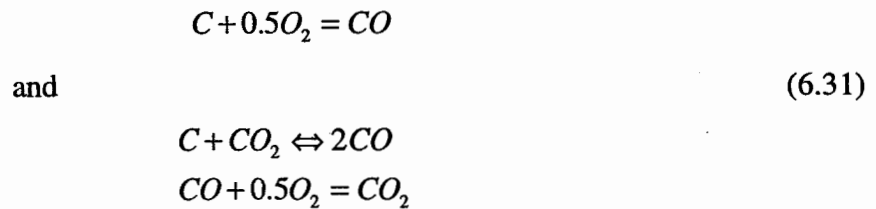


Soot will form when  $x \geq 2m$ , i.e. when the atomic C-O ratio is unity. However, since soot formation is a non-equilibrium process soot is found at C-O ratios much less than unity at temperatures below 2000K, and also at ratios greater than unity at higher temperatures.

The process of soot formation occurs in three stages: soot-particle nucleation, agglomeration and surface growth, and coagulation. The first step is the one least understood. Quasi-global models have been developed to describe the process of soot formation. Najjar and Goodger (1981a) developed a successful model after studying soot formation in a gas turbine combustor burning kerosene and gas oil. The formulation developed for kerosene is,

$$\frac{dC_s}{dt} = 4.4 \times 10^{14} C_F \exp\left(-\frac{12100}{T}\right) - 3.0 \times 10^9 C_{O_2} \exp\left(-\frac{7800}{T}\right) \quad (6.30)$$

Soot oxidation tends to dominate in the regions downstream of the primary zone, at lower fuel/air ratios, and correspondingly higher temperatures. Temperatures greater than 1400K and the presence of oxygen is necessary for the combustion of soot. In this way a significant amount of soot formed in the primary zone is consumed in the regions immediately downstream. In fuel lean flames the oxidation progresses through the following reactions,



A successful formulation developed by Najjar and Goodger (1981b), using an adaptation of the Nagle and Strickland-Constable (1962) model, has the overall specific surface reaction given by,

$$w = 12 \left[ \frac{\psi K_A p_{O_2}}{1 + K_Z p_{O_2}} + K_B p_{O_2} (1 - \psi) \right] \text{ g cm}^{-2} \text{ s}^{-1} \quad (6.32)$$

where,

$$\psi = \left( 1 + \frac{K_T}{p_{O_2} K_B} \right)$$

$$K_B = 4.46 \times 10^{-2} \exp\left(-\frac{63596.8}{RT}\right)$$

$$K_T = 1.15 \times 10^5 \exp\left(-\frac{251040}{RT}\right)$$

and for temperatures greater than 1800K,

$$K_A = 380 \exp\left(-\frac{12552}{RT}\right)$$

$$K_Z = 5000 \exp\left(-\frac{20920}{RT}\right)$$

and for temperatures less than 1800K,

$$K_A = 2300 \exp\left(-\frac{125520}{RT}\right)$$

$$K_Z = 2.13 \exp\left(-\frac{17154.4}{RT}\right)$$

Lefebvre (1984) recommends this formulation as it has shown satisfactory agreement with exhaust smoke concentrations, over a range of combustor operating conditions. The constants derived in this work were taken from experiments made at representative gas turbine combustor conditions.

Mongia (1994) and Rizk and Mongia (1991) presented an alternative approach, supplementing empirical data into multi-dimensional calculations to predict the sooting process of formation and oxidation respectively, within a gas turbine combustor,

$$\begin{aligned}
S_F &= 0.1773 P^2 (18 - H)^{1.5} \left[ \frac{(F/A) m_B}{T m_A T_u^{0.25}} \right]_{ijk} \\
S_O &= 0.042 \frac{P^2}{V} \left( \frac{F/A}{T} \right)_{pz} (18 - H)^{1.5} \left[ \frac{V \exp(0.0011T)}{m_A (F/A)} \right]_{ijk} \quad [\text{mg/kg}] \quad (6.33)
\end{aligned}$$

where,

$P$  = liner inlet pressure (kPa)

$F/A$  = fuel/air ratio

$T$  = gas temperature

$H$  = hydrogen content of fuel

$pz$  = refers to primary zone values

$m_A$  = air flow rate

$m_B$  = fuel fraction burned within sub-volume

$V$  = volume

$ijk$  = refers to sub-volume values

$T_u = \left[ \frac{\rho k^{3.5}}{\epsilon^2} \right]_{ijk}$  = mixing rate parameter

$\rho$  = gas density

$k$  = kinetic energy of turbulence

$\epsilon$  = rate of dissipation of kinetic energy of turbulence

Sudarev and Antonovsky (1990) developed a formulation for soot concentration based on a detailed experimental study of a class of combustors. The derivation is based upon empirical data gathered on a test rig, and extrapolated for elevated pressure. A functional relationship between fuel burn-out and pressure was developed to improve the quality of this extrapolation. The formulation for the soot concentration is,

$$C_s = 4.57(C/H)^2 \frac{\bar{P}}{\alpha T} \left[ \bar{L} + \frac{355}{L_0} \bar{L}^{0.5} \left( 1 - \bar{L}^{0.04 \frac{\bar{P}}{\alpha}} \right) \right] \quad [\text{g/m}^3] \quad (6.34)$$

where,

$C/H$  = carbon hydrogen ratio of the fuel

$\alpha$  = air excess ratio in the flame cross-section

$T$  = gas temperature

$L_0$  = theoretical quantity of air to burnout 1 kg of fuel

$\bar{P} = \frac{P}{P_a} = \frac{\text{pressure at flow cross - section}}{\text{atmospheric pressure}}$

$\bar{L} = \frac{L}{L^*} = \frac{\text{distance of flow cross - section from the atomizer (baseplate)}}{\text{length of flame burn - out (distance over which the completeness of fuel combustion goes from 0 - 99%)}}$

Once the soot and gas emissivities have been computed the effective total emissivity may be obtained from the following,

$$\epsilon_T = \epsilon_g + \epsilon_s - \epsilon_g \epsilon_s \quad (6.35)$$

The total emissivity calculated using Eq. (6.35) has been found to give good agreement with values computed using a more detailed non-gray analysis (Lefebvre, 1984).

Although a net emissivity has been found for a gas soot mixture, an absorption coefficient is required for the DT calculation, see Eq. (6.3). The absorption coefficient is,

$$k_a = -\frac{\ln(1 - \epsilon_T)}{\Delta s} \quad (6.36)$$

This formulation makes the assumption that the constituents of the traversed control volume are gray. Although this is true for the soot, it is not so for the gas. The only alternative is to perform a banded intensity calculation (Bressloff, et al, 1996) significantly increasing the computational effort required. The data required for such

models has only been derived at pressures well below the operating conditions of a typical combustor. The effect of soot on the emissivity will generally swamp out the gas effects. Thus the effect of errors introduced through the use of Eq. (6.36) will be small. In regions of high soot concentrations the contribution of the gas emissivity may become negligible.

## 6.5 Profiles/Templates

From the description of the DT method given in the previous sections it is clear that the ray tracing calculation is three-dimensional, but the calculation is being constrained to axisymmetric geometries. However, the flowfield used in the calculation, obtained from the network solver is only one-dimensional. This is a severe limitation when computing radiative transfer, as radial variations in temperature and property profiles might significantly affect the radiation in real situations.

User specified profiles allow the DT calculation to be performed taking into account the radial variations in the gas. The radial profiles may be either absolute values or non-dimensional values about the computed mean obtained from the network solver. This is done on the premise that even a very rough profile will give a more accurate result than a simple flat one. The profiles may be derived from two sources, either user defined based on experience, or from experimental and CFD (computational fluid dynamics) analysis of a particular combustor. The overall profiles within the combustor should remain relatively similar over a complete range of operating conditions

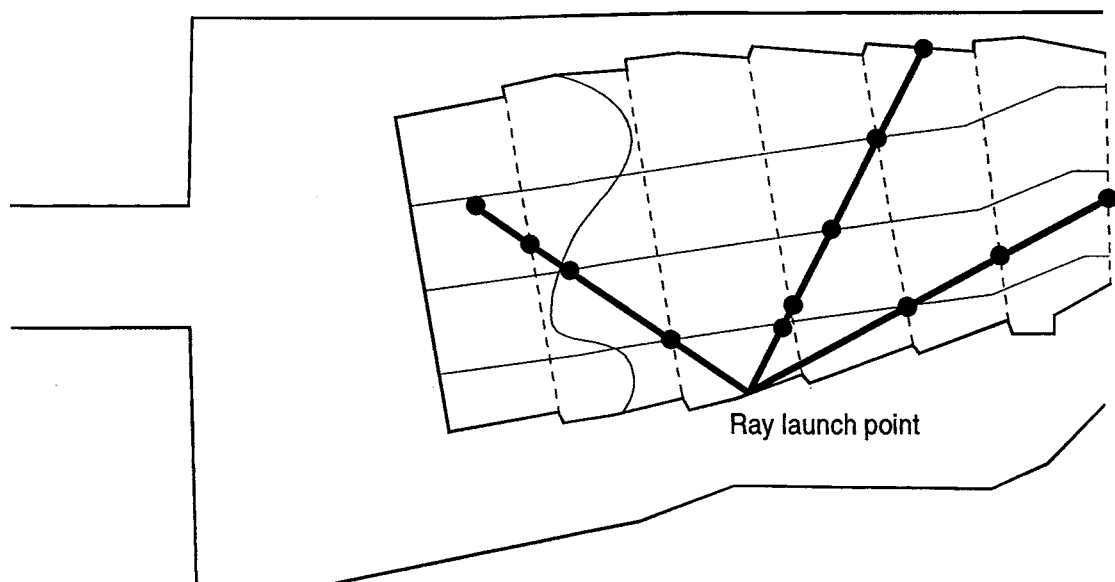


Figure 6.5. Ray tracing in a typical annular gas turbine combustor with radial profiles

Fig. 6.5 represents a simple extension of concept from Fig. 6.4. A circumferentially averaged radial profile (represented by the curve in Fig. 6.5) is now included in the combustor, breaking the control volumes into radial segments in which the gas properties may vary. The ray-tracing procedure must now compute the intersections with the control volume boundaries as well as the radial segment boundaries generated by the profile. The profiles are assumed to be of constant radius over a particular control volume. Thus ray pathlengths are obtained for each volume of constant properties, and the change in intensity across each volume may be readily computed. Any number of radial boundaries may be specified in the form of a profile. The greater the number of such boundaries the greater the computational effort, as each set of new intersects must be computed.



## **6.6 Results and Discussion**

### **6.6.1 Validation of DT method for simple geometries**

A wide range of radiation calculations have been performed in simple geometries. Three representative cases were selected to compare the current solution methodology with that of proven results.

The first comparison was performed on a finite cylinder with black walls (Shah, 1979). The geometry is illustrated in Fig. 6.6. The walls are at a constant temperature of 773K, and contain a gas at a temperature of 1000K. The enclosed gas is assumed to have a uniform absorption coefficient of  $0.25\text{m}^{-1}$ . The exact solution compared closely with that of the DT calculation using 128 rays. Increasing the number of rays improved the accuracy of the calculation. The selected number of rays provided sufficient accuracy. The improvement in computational accuracy using large numbers of rays is offset by the penalties in computational efficiency.

Malalasekera and James (1996) performed radiation calculations in three-dimensional complex geometries using the DT method. The accuracy of their model was successfully evaluated using the results of Chui et al (1993). The geometry used is shown in Figure 15.2. The cylindrical enclosure is 6m long and 2m in diameter. The walls are black at a constant uniform temperature of 500K. The gas temperature varied axially along the cylinder, as shown in Fig. 6.7. Results were obtained for three different absorption coefficients, using an exact calculation, and the finite volume method of Chui et al (1993). The comparison is shown in Fig. 6.8. The results compared well in all three cases.

The final validation case presented a radial variation in temperature and properties, allowing a DT calculation with a radial profile to be evaluated. The geometry considered (Shah, 1979) consisted of a finite cylinder 5m long and 2m in diameter. The walls are at a

temperature of 773K and an emissivity of 0.8. The gas contains a hot region at a temperature of 1700K and an absorption coefficient of  $0.6\text{m}^{-1}$ . The remainder of the cylinder is at a temperature of 1100K and an absorption coefficient of  $0.05\text{m}^{-1}$ , as shown in Fig. 6.9. Comparisons were made between a detailed accurate Monte Carlo calculation and the DT calculation using 8, 64, and 128 rays (see Fig. 6.10). The importance of using a sufficient number of rays is clearly illustrated. If too few rays are used the calculation suffers from the 'ray effect'. The number of representative rays used must capture variations in the gas temperature and properties. This may lead to problems in gases with steep gradients as the rays may completely 'miss' a peak value, and hence the 'ray effect'. In this case the DT calculation with 128 rays was shown to provide a sufficiently accurate result.

## 6.6.2 Combustor simulations

An annular combustor was selected for the analysis using the new discrete transfer radiation model. Three variations of the combustor were modelled, and the results were compared with experimental thermal paint data in all three cases (Metcalf, 1996). The three combustors were designated Annular Combustor .1. (AC1), Annular Combustor .2. (AC2), and Annular Combustor .3. (AC3). Network diagrams of the three combustors are shown in Fig. 6.11, Fig. 6.12, and Fig. 6.13. The overall geometries are the same in all cases. The combustors rely on a series of lipped cooling rings to generate liner cooling films, supplemented by effusion patches in regions of high thermal load. The liner features sizes vary in each case, and additional effusion cooling was specified in AC2 and AC3. The dashed network shows the dedicated conjugate heat transfer links. The heat transfer through the lipped cooling rings is modelled, and these regions are treated as double skin regions with heat transfer from all surfaces. The flametube was coated with a thermal barrier in all three cases.

Radial profiles of soot (Brocklehurst et al, 1997) and gas temperature (Boyce, 1996) were used to evaluate the effect of profiles on the combustor radiative and total heat fluxes. The absolute temperature profile was obtained from a CFD prediction of this specific combustor type. The soot profiles were obtained from a similar annular combustor type, and so the relevance of the profiles were limited in combustors of the type analysed here. The soot predictions differed by approximately an order of magnitude or more with the measurements (Brocklehurst et al, 1997), and the profile shapes were significantly different. The predictions were reduced by an order of magnitude, in line with the measured values, and then linearly scaled upwards to the operating pressure of the combustors under consideration. Although the soot profiles may differ significantly from the true values, they were nevertheless useful in evaluating the effects of soot on the radiative heat transfer within the combustor.

The combustors were analysed at the conditions used to obtain the thermal paint data. The thermal paint data (Metcalf, 1996) was provided as a single mean value at specific axial locations along the liner walls. The thermal paint measurements were made on the hot side of the liner thermal barrier coating. The width of the thermal paint bands used to obtain the wall temperatures were approximately (Metcalf, 1996):

$$\pm 20\text{K for } T_{\text{wall}} > 1173\text{K}$$

$$\pm 50\text{K for } 1173\text{K} > T_{\text{wall}} > 1073\text{K}$$

$$\pm 100\text{K for } T_{\text{wall}} < 1073\text{K}$$

These do not include the effects of sector variation, which might account for a further temperature variation of  $\pm 30\text{K}$ .

The number of rays required to accurately model the radiative transfer in the combustors under investigation was evaluated for AC1. Profiles of temperature and soot dividing the flametube into 28 radial sections were used in the calculation. The variation of the net radiative flux on the inner liner wall is shown in Fig. 6.14. Results for 64, 128 and 260 rays are presented. The variation between all three cases was small. Although the solution with 64 rays was least accurate, it was still adequate for representing the radiative transfer. The effect these slight differences had on the hot-side wall temperature was very small, as shown in Fig. 6.15. The number of rays required for a particular combustor might vary depending on the nature of the profiles used. It is recommended that the sensitivity of the number of rays used be evaluated to avoid the possibility of 'ray effects'.

Comparisons between predicted and experimental hot-side liner wall temperatures for AC1 are shown in Fig. 6.16 and Fig. 6.17. The 'Semi-empirical' prediction relies on a semi-empirical radiative flux calculation based upon bulk temperature, pressure and  $C/H$  ratio, as described in Chapter 5.

The 'DT - soot1' prediction involves a full discrete transfer radiation model of the combustor flametube. The soot volume fractions in this case used a model incorporating measurements in a confined turbulent jet flame (Brocklehurst et al, 1997). The model

does not correctly compute the oxidation of soot and hence the soot concentrations are one or two orders of magnitude higher than measured values.

The 'DT - soot2' prediction uses the same temperature profile as the previous prediction but the soot profile is derived from a model incorporating detailed reaction kinetics (Brocklehurst et al, 1997). The soot volume fractions in this case compared more closely with the measured data.

The peak thermal paint temperatures fall in the narrowest thermal paint band range (i.e.  $\pm 20\text{K}$ ). The 'soot2' prediction provided a moderately better comparison with wall temperatures than the 'soot1' calculation. The maximum difference between the 'soot2' prediction and the thermal paint measurements was 100K, within the primary zone. However, the difference was much less than this over most of the inner and outer annulus liner walls. The trends of the prediction closely matched those of the measurements. The large difference in the primary zone indicates the soot concentrations are not representative of the true levels. The maximum soot volume fraction in the primary zone profile was approximately  $5 \times 10^{-6}$ . The wall temperatures were strongly dependent on both the soot volume fraction and the gas temperature. The largest uncertainty was in the soot volume fraction profiles.

Figure 6.18 and Fig. 6.19 shows the differences in the predicted net radiative heat flux along the outer and inner liner walls respectively. The dip in the primary zone flux at location 0.2 on the outer liner was a result of the combined effects of a strong cooling film combined with profile effects. This becomes more clear in the results which follow. The primary zone fluxes were the highest, although higher values might be expected, in relation to downstream levels.

A similar wall temperature comparison was performed on AC2. The results are shown in Fig. 6.20 and Fig. 6.21. The outer annulus thermal paint data compared very well with the 'DT - soot2' calculation. While the peak wall temperatures on the inner and outer liners were similar in the calculated values, the thermal paint data specified an inner liner

temperature 65K higher than the outer liner. The largest difference between the thermal paint and 'DT - soot2' occurred on the inner liner in the primary zone, and was 80K. The axial location of the thermal paint data points between the minimum and maximum values, in a particular bay, were not always clearly defined in comparison to the calculated results. The discrepancies in these intermediate temperatures is therefore not cause for concern. Further, the error bands in the thermal paint data was 100K in this region. The effects of the effusion patches at the flametube exit on the outer liner are clearly illustrated with a significant reduction in temperature compared to AC1 in this region.

The wall temperature results of the final combustor modelled, AC3, are shown in Fig. 6.22 and Fig. 6.23. The thermal paint temperatures on this combustor were significantly higher than on the previous two combustors modelled. It is therefore not surprising that the differences between the predictions and measurements is larger in this case, as exactly the same soot and temperature profiles were used. The minimum thermal paint temperatures should not be used as a basis for comparison, as they were simply set to approximately compressor delivery temperature in this non-critical region adjacent to the lipped cooling ring exits. The maximum difference with the 'DT - soot2' calculation of 200K in temperature occurred in the primary zone, within the first bay. Downstream of this region the differences reduced. The effects of additional effusion on the outer liner were clearly captured by the calculation on the outer liner. The thermal paint predictions on the inner liner were not satisfactorily resolved within the effusion patches.

When designing a combustor it is unlikely that sufficient information will be available to generate temperature and soot profiles within the flametube. The sensitivity of the profiles in calculating the radiative and total fluxes should therefore be evaluated. AC1 was selected for performing the analysis at three different orders of magnitude of soot volume fraction. The 'soot2' profile was used in the evaluation as it was thought to be more representative of the real profile shape than 'soot1'.

Figure 6.24 shows a wall heat flux comparison on the outer liner. The dark lines, designated '2' represent the calculation performed using the 'soot2' profile, with a maximum soot volume fraction of  $1 \times 10^{-6}$ . The values with designation '1' use bulk values of soot and temperature, averaged from the profile values. The radiative fluxes using the bulk properties were higher than those using the profiles, especially in the primary zone. However, the convective fluxes compensated for this increase to some extent and the overall flux did not show a significant variation. The reason for this compensating effect is the fact that the convective fluxes are negative over large sections of the film cooled liner wall. The effect on temperature was relatively small, as shown in Fig. 6.25, illustrating the difference in temperature between the bulk and profile calculated wall temperatures. As expected the largest difference was in the primary zone, where the radiative flux is highest.

The same analysis was performed with a peak soot volume fraction of  $1 \times 10^{-5}$ . The radiative fluxes were now much higher, and the difference between the bulk and profile calculation was also higher (see Fig. 6.26). The convective fluxes were also larger. This corresponded to a larger negative flux in regions of high film cooling. The overall wall temperature differences were approaching 60K in the primary zone in this case (see Fig. 6.27).

The calculation was repeated with an order of magnitude higher soot volume fractions,  $1 \times 10^{-4}$  peak value. The trend was repeated as shown in Fig. 6.28. The bulk calculation predicted higher radiation in the primary zone, but this became lower than the profile values downstream of the primary zone. This illustrated the importance of gas temperature in the radiative flux calculation. At high soot volume fractions and relatively low gas temperatures the soot may act as a shield, reducing the radiative flux to the wall. Fig. 6.29 showed a difference in temperature between profile and bulk values approaching 90K. As expected from the flux results the temperature difference was negative downstream of the primary zone.

The final analysis was performed to evaluate the effect of ignoring the gas effects from the radiation calculation. Although the soot will tend to dominate emission this is not the case in regions containing low levels of soot. The computations were performed at the same orders of magnitude used in the previous comparison. The gas emissivity was calculated based on bulk concentrations of  $\text{CO}_2$  and  $\text{H}_2\text{O}$  from the constrained equilibrium calculation. All properties were calculated based upon bulk values.

Figure 6.30 shows the comparison of heat fluxes with and without gas effects for a maximum bulk soot concentration of  $5 \times 10^{-6}$ . The curves designated '1' represent the calculation without gas effects, and designation '2' represents with gas effects. The gas emissivity had a significant effect on the level of radiation. This resulted in a large temperature difference between the two results, as shown in Fig. 6.31. For a maximum soot volume fraction of  $5 \times 10^{-5}$  the difference in fluxes between the two cases is much lower, as shown in Fig. 6.32, resulting in a lower discrepancy in the temperatures (see Fig. 6.33). When the soot volume fraction was increased to a peak value of  $5 \times 10^{-4}$  the difference in flux with and without gas emissivity becomes very small (see Fig. 6.34). The corresponding differences in temperature were also very low (see Fig. 6.35). In all the above cases the effects of the gas were most prominent in regions of lower soot concentration.



## **6.7 Conclusions**

A radiative heat transfer model was developed based upon the discrete transfer radiation procedure. The new formulation was validated against a number of benchmark test cases before being incorporated within the network solver.

A three-dimensional ray tracing procedure for the quasi one-dimensional network solver was developed whereby all control volume surfaces and rays were described by equations. Soot and gas properties models were included in the new procedure to provide local volume emissivities. The effects of temperature and soot radial profiles in the DT method was included to examine the sensitivity of radially resolved variations in the overall computed radiative wall heat flux.

Three variations of an annular combustor were modelled using the new procedure. Two different soot profiles from a representative annular combustor were used in the DT calculation. The full calculation including approximately 25 axial cells and 40 radial stations in the flametube required 3-5 minutes to converge on the Silicon Graphics Indy Workstation, depending on the coupling selected between the radiation, energy and flow equations.

Comparisons were made between computed temperatures and experimentally obtained thermal paint temperatures. The hot-side thermal paint bands were relatively narrow, especially at the more critical peak temperatures, compared to those used in the previous chapter. However, the widths of the bands combined with their circumferential averaging produced a minimum range of approximately 50K. The same soot profiles were used in all three combustors, and hence the performance of the profiles in capturing the flametube radiative characteristics varied. The largest discrepancies between the wall temperatures occurred in the primary zone. This appeared to be an effect of the radial soot and temperature profiles used, rather than a shortfall in the radiation model. The predictions accurately captured the correct trends in the wall temperatures. The

magnitude of the wall temperatures compared well with the experimental results outside the primary zone.

The effect of the soot and temperature profiles were evaluated by examining wall heat fluxes and temperature differences. The shape of the profile became more important with increasing soot concentrations. Downstream of the primary zone the effect of the profile was small due to the lower soot concentrations and the flatter profile in this region, compared to the primary zone.

The effects of gas emission became negligible at elevated soot concentrations. However, it is unlikely that the gas effects may be ignored in the regions downstream of the combustor primary zone where the soot is depleted.

Although an accurate radiation calculation is now possible within the network solver it relies on a reasonable knowledge of the temperature and soot distribution within the combustor flametube. Physically realistic assumptions of gas temperature and soot concentrations should provide a reasonable evaluation of the wall temperature characteristics. The bulk gas temperature generated using the combustor network solver could be used for the radiation calculation. However, for the constrained equilibrium calculation to produce a realistic temperature a combustion efficiency curve must be available for the particular combustor being evaluated.

An accurate radiation model was successfully developed for the combustor network solver capable of modelling axisymmetric cannular, annular, multi-annular and reverse flow gas turbine combustor geometries. The incorporation of the discrete transfer radiation model provides a versatility and accuracy comparable to the underlying network algorithm.

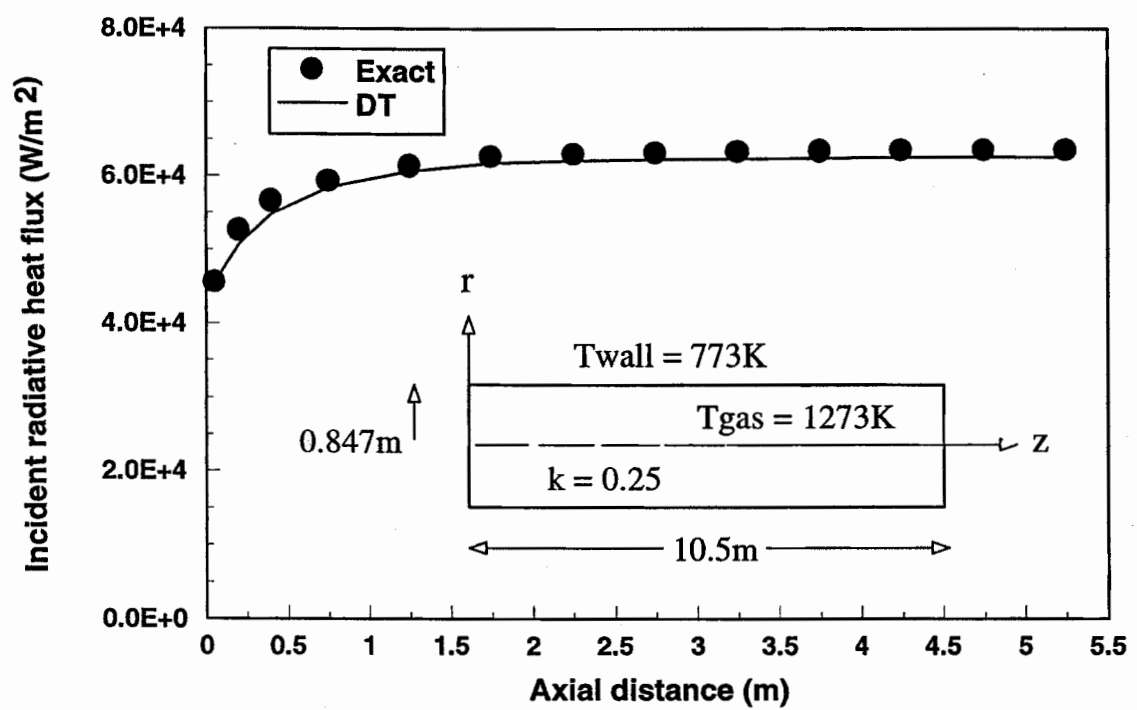


Figure 6.6. Comparison of predicted incident radiative heat flux with exact values

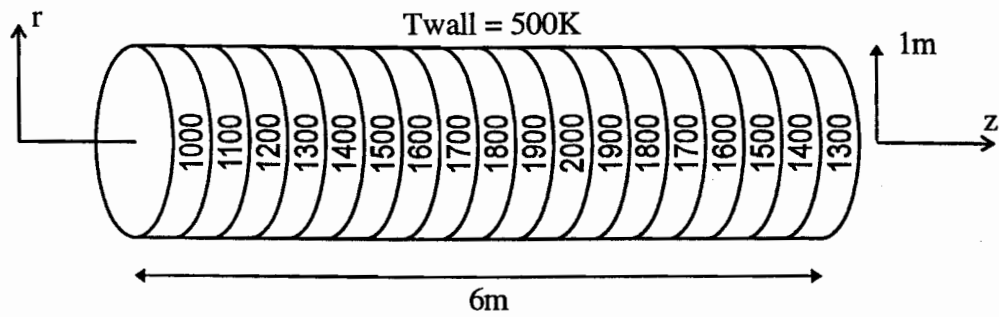


Figure 6.7. Geometry and gas properties for discrete transfer validation in a finite cylinder

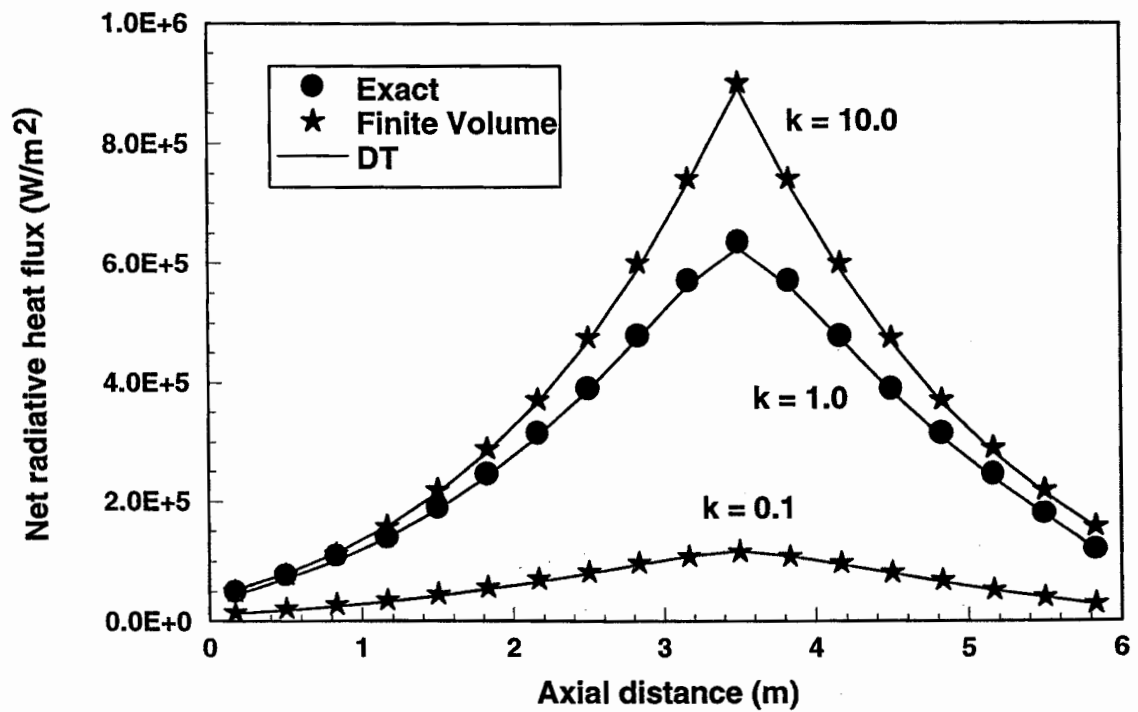


Figure 6.8. Results of comparison of net radiative heat flux along a cylinder

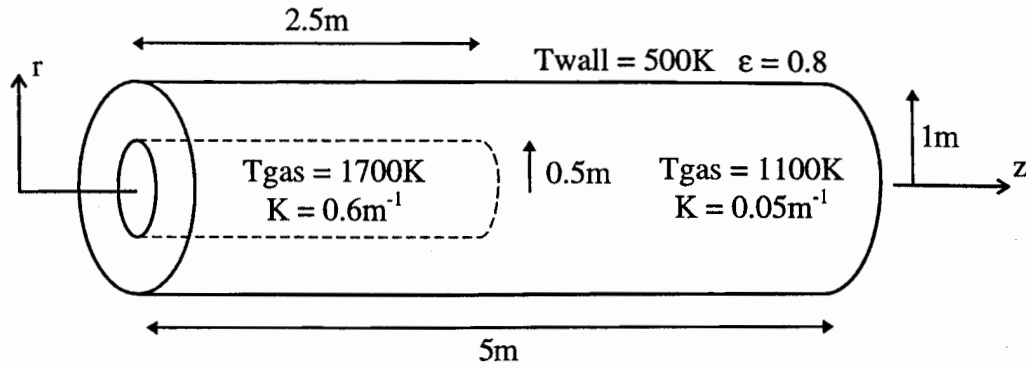


Figure 6.9. Geometry and properties for radial variation validation

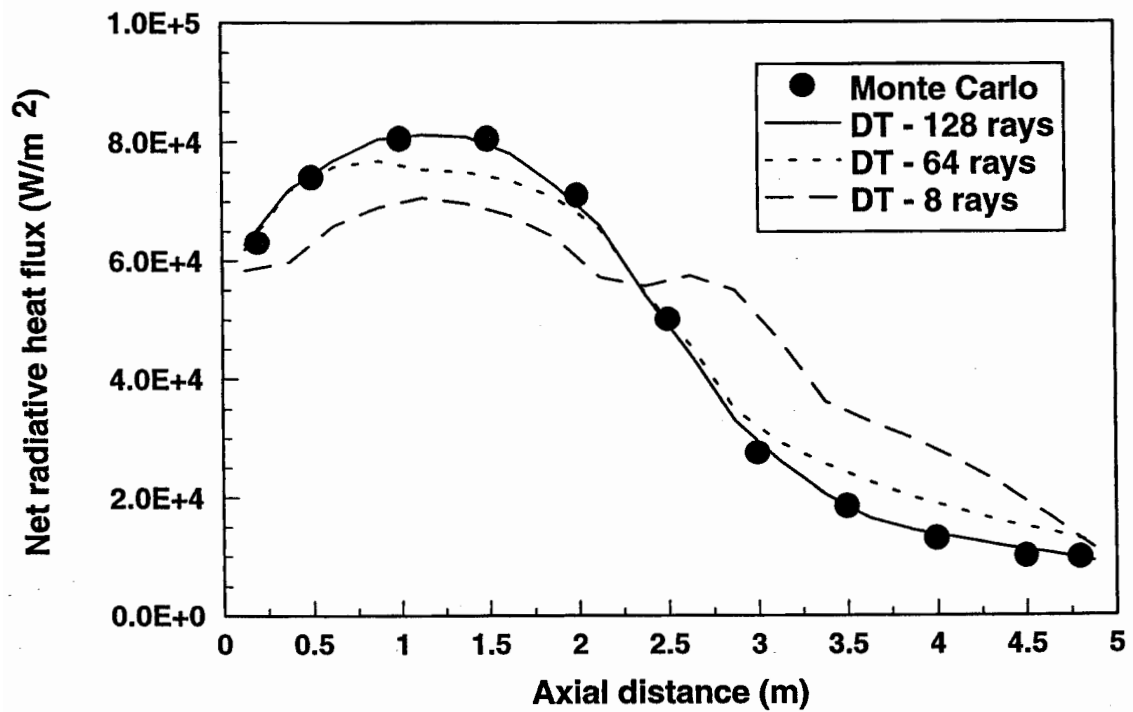


Figure 6.10. Comparison between a Monte Carlo type calculation and DT with varying numbers of rays

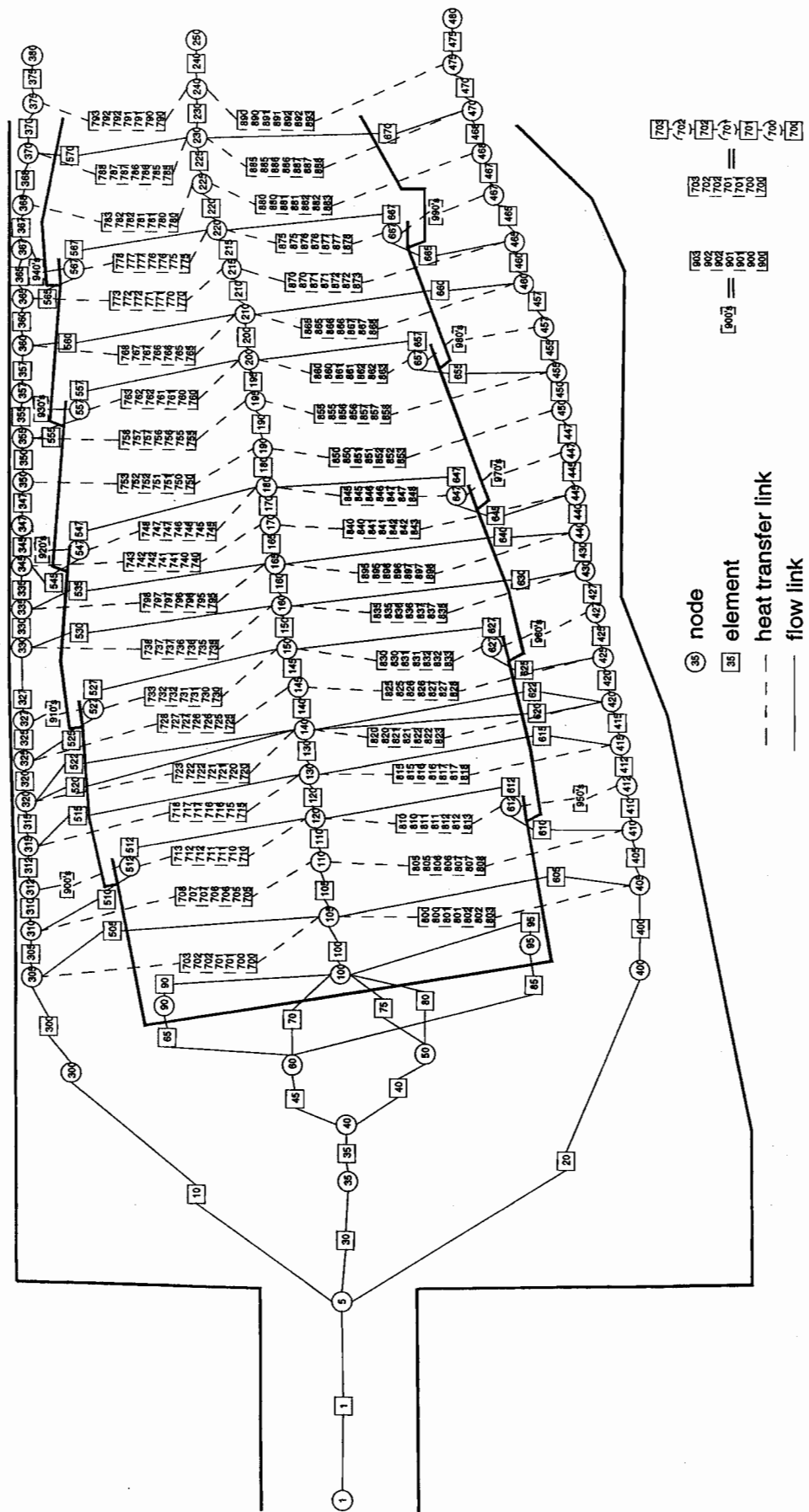


Figure 6.11. Annular Combustor .1. network diagram

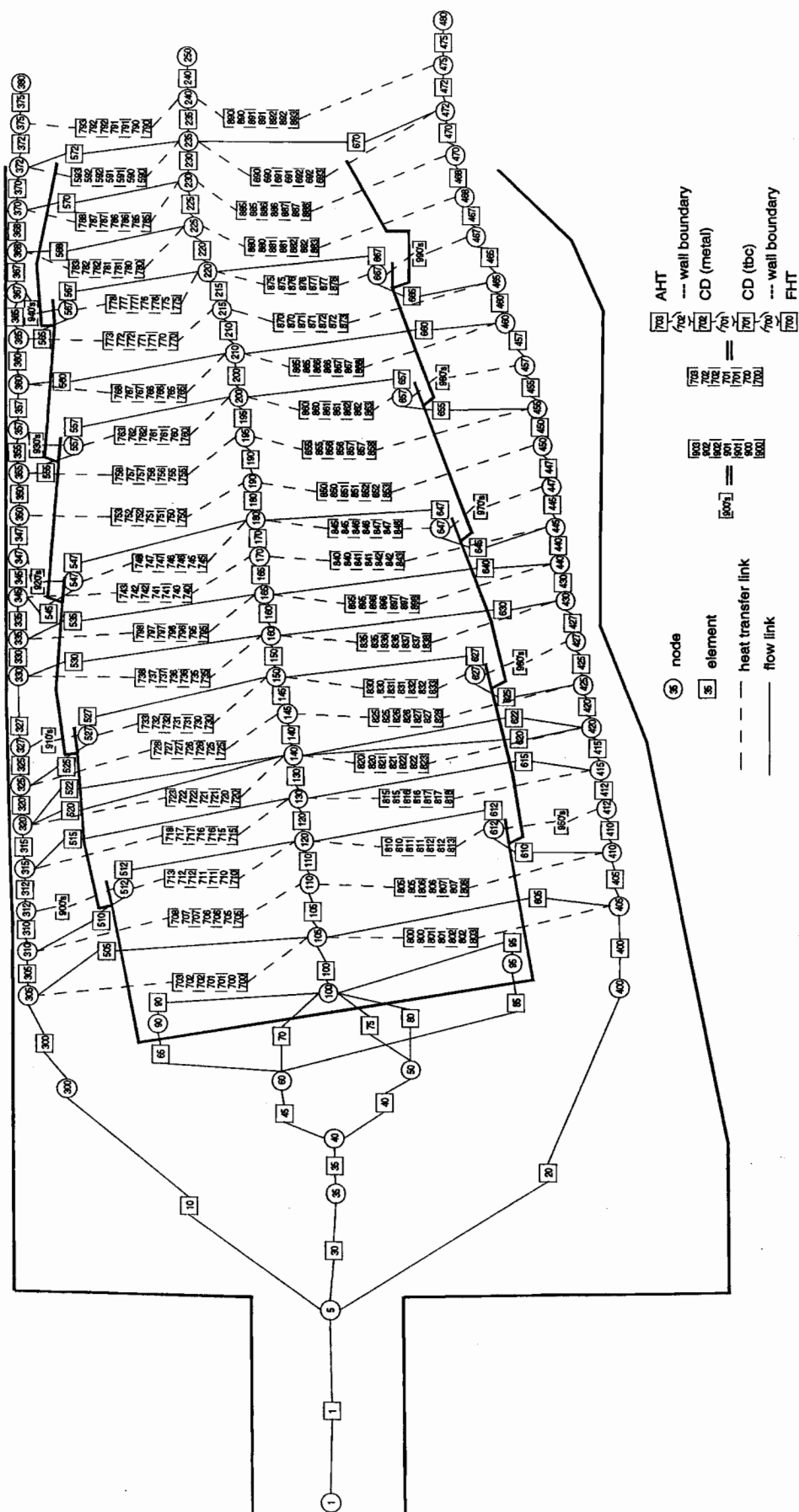


Figure 6.12. Annular combustor .2. network diagram





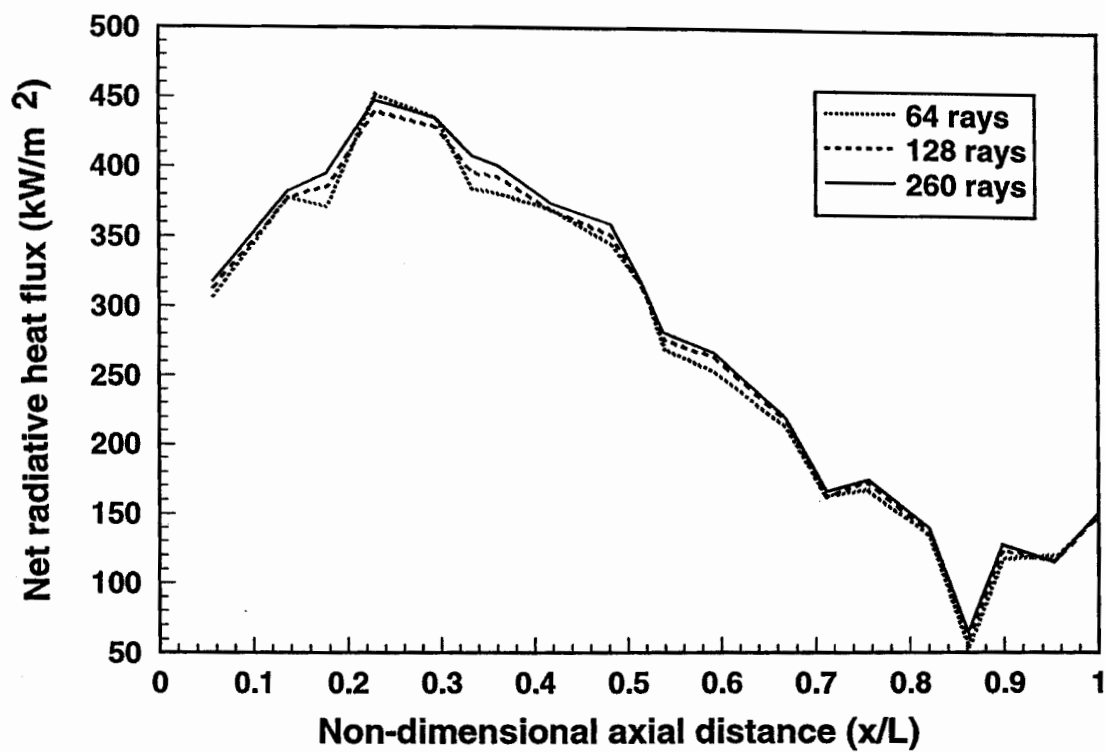


Figure 6.14. AC1 inner liner radiative heat flux comparison

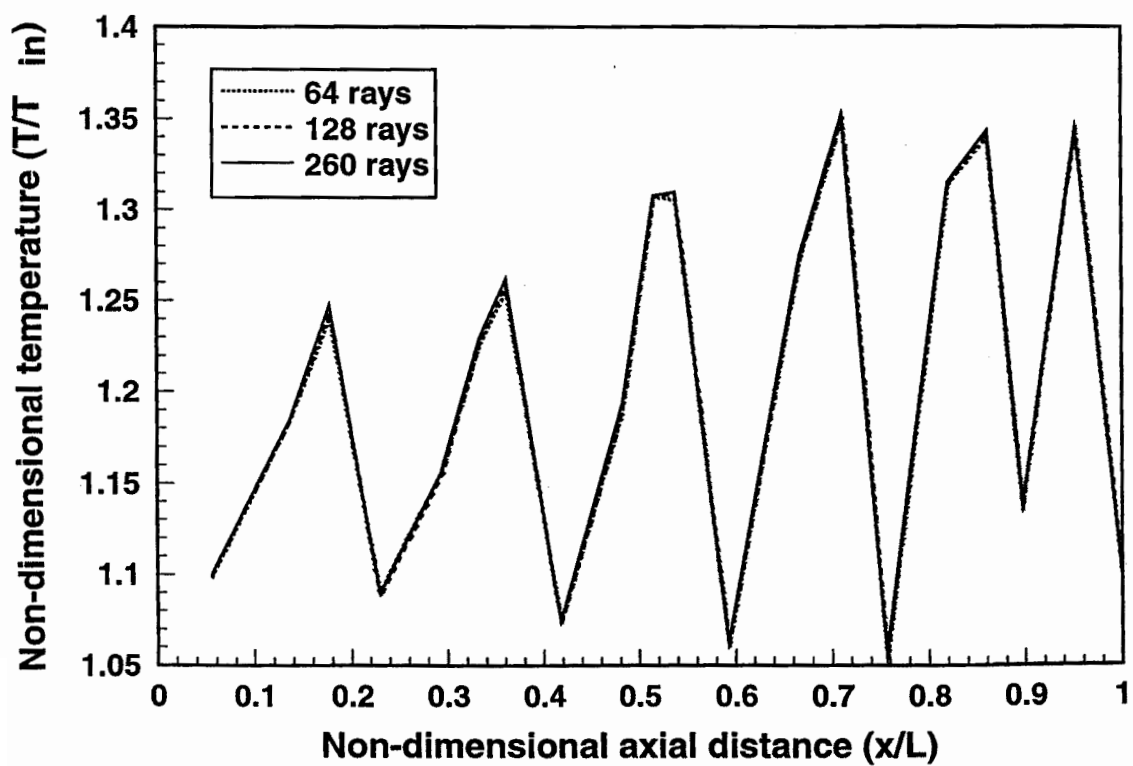


Figure 6.15. AC1 inner liner wall temperature comparison

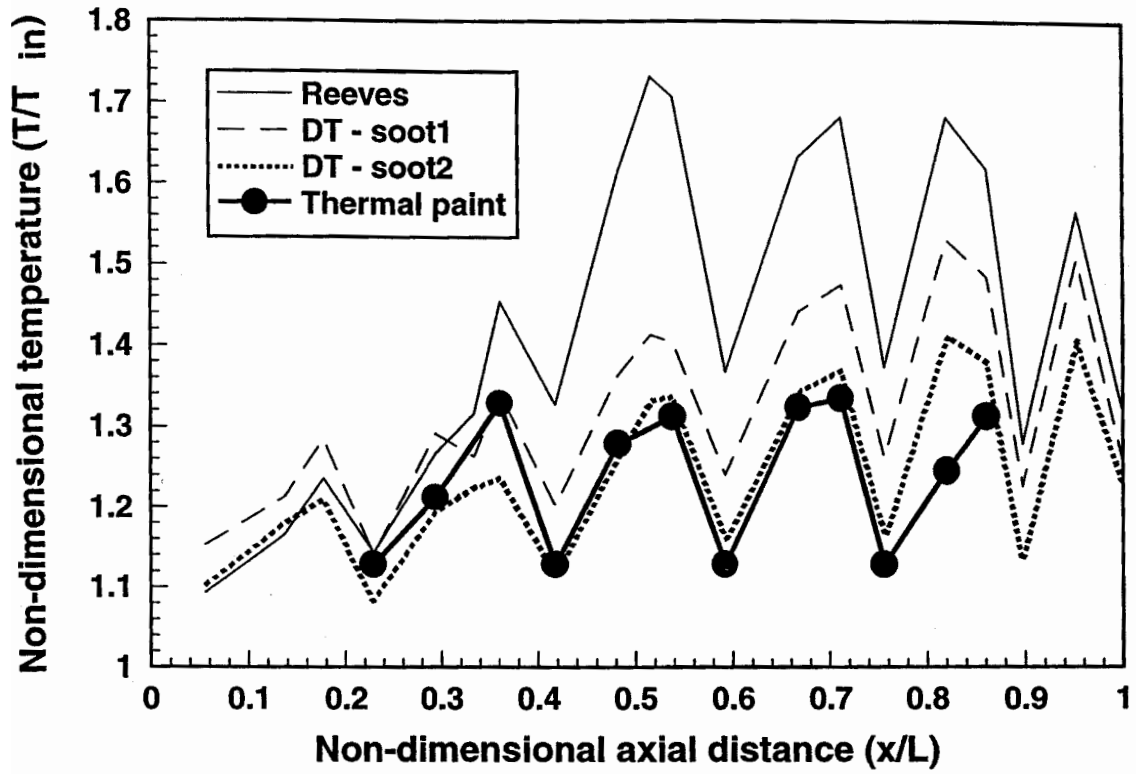


Figure 6.16. AC1 outer liner hot-side wall temperatures

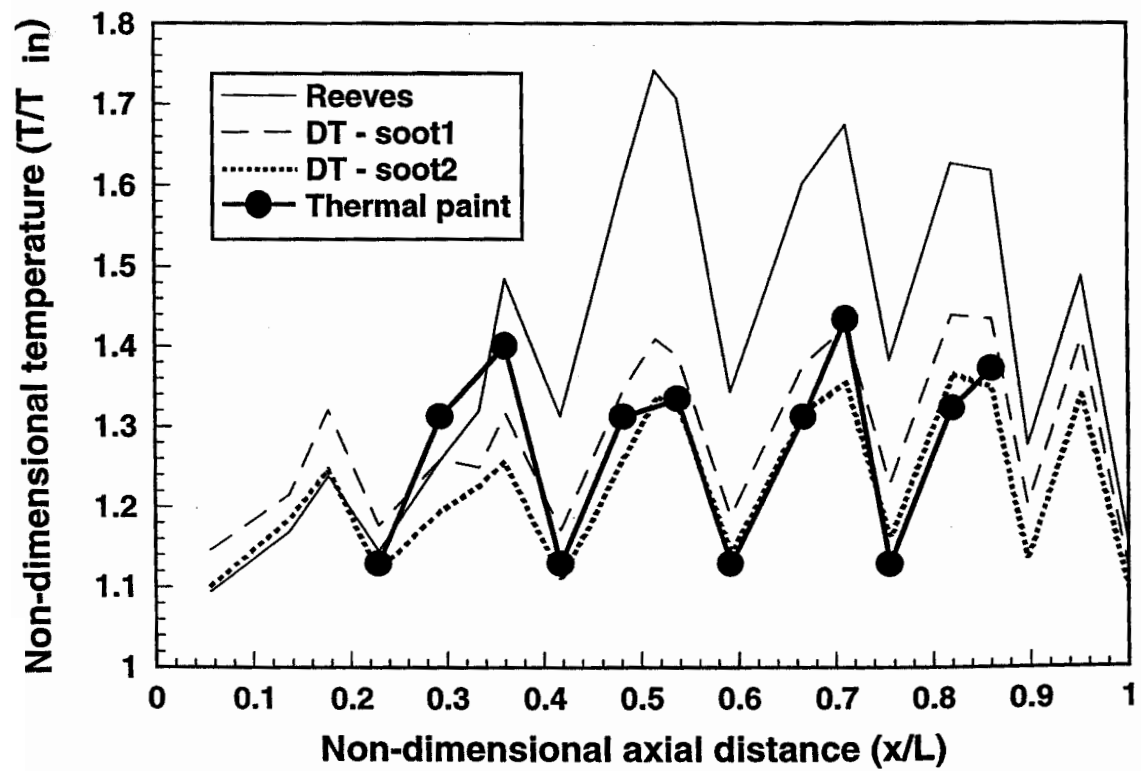


Figure 6.17. AC1 inner liner hot-side wall temperatures

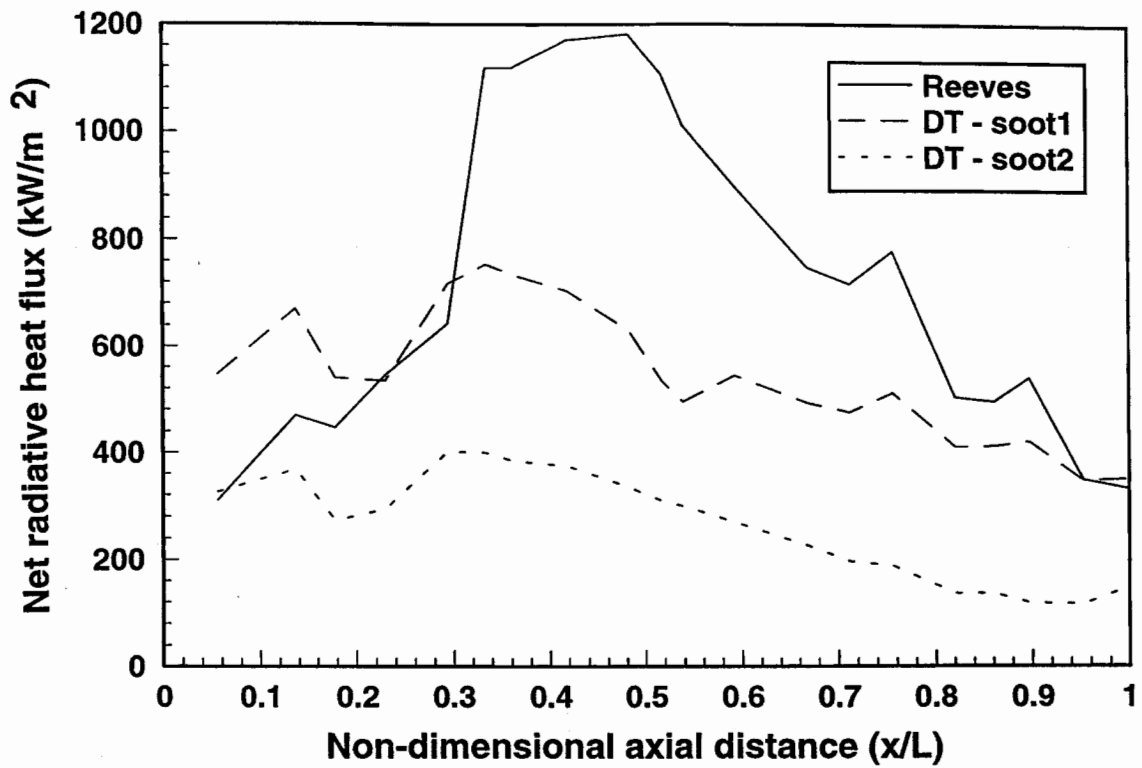


Figure 6.18. AC1 outer liner radiative heat flux comparison

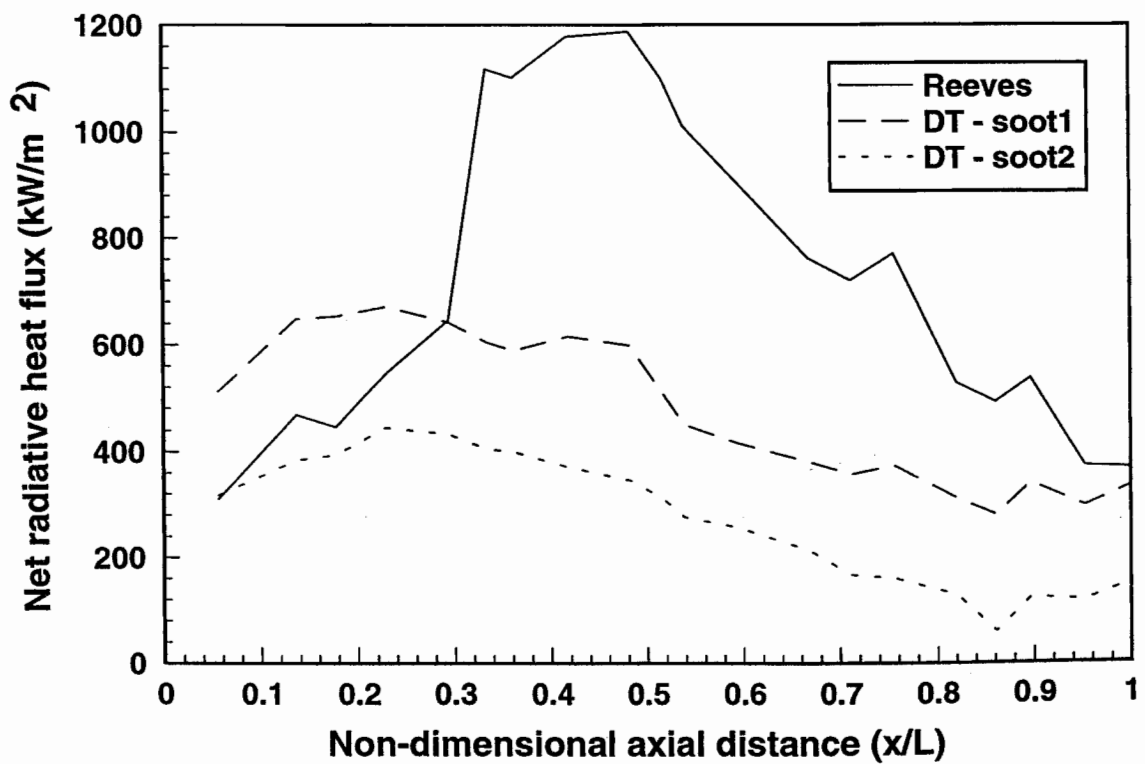


Figure 6.19. AC1 inner liner radiative heat flux comparison

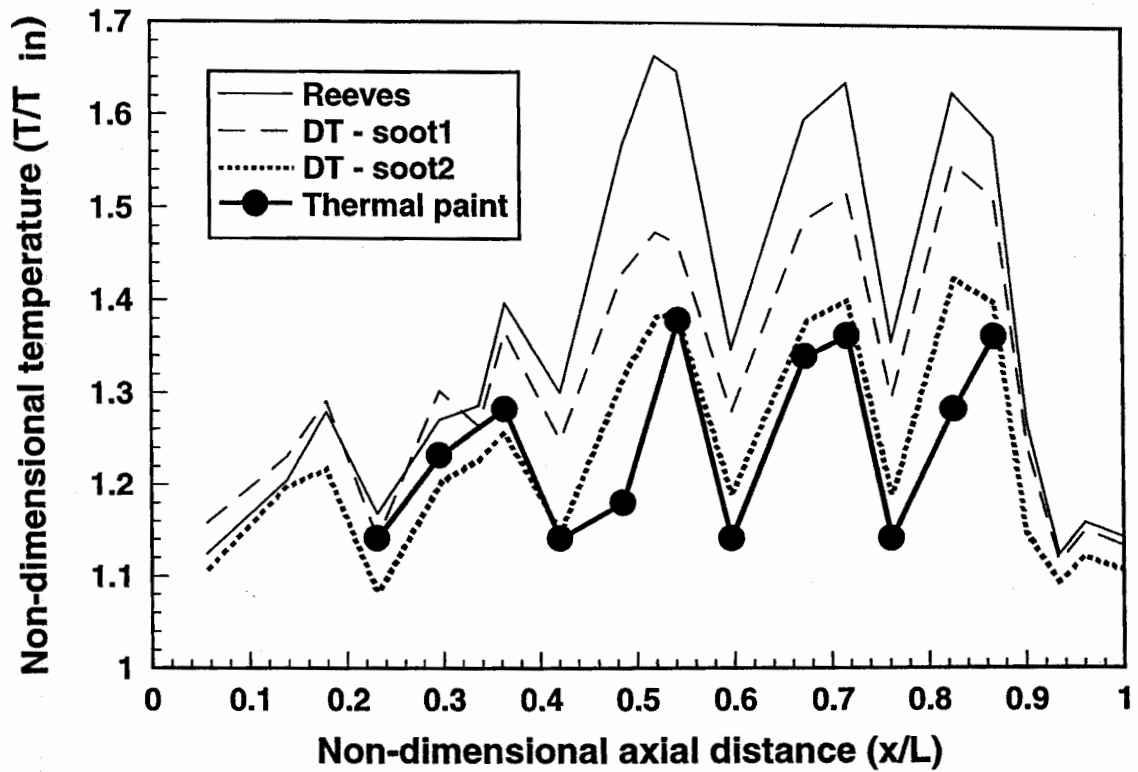


Figure 6.20. AC2 outer liner hot-side wall temperatures

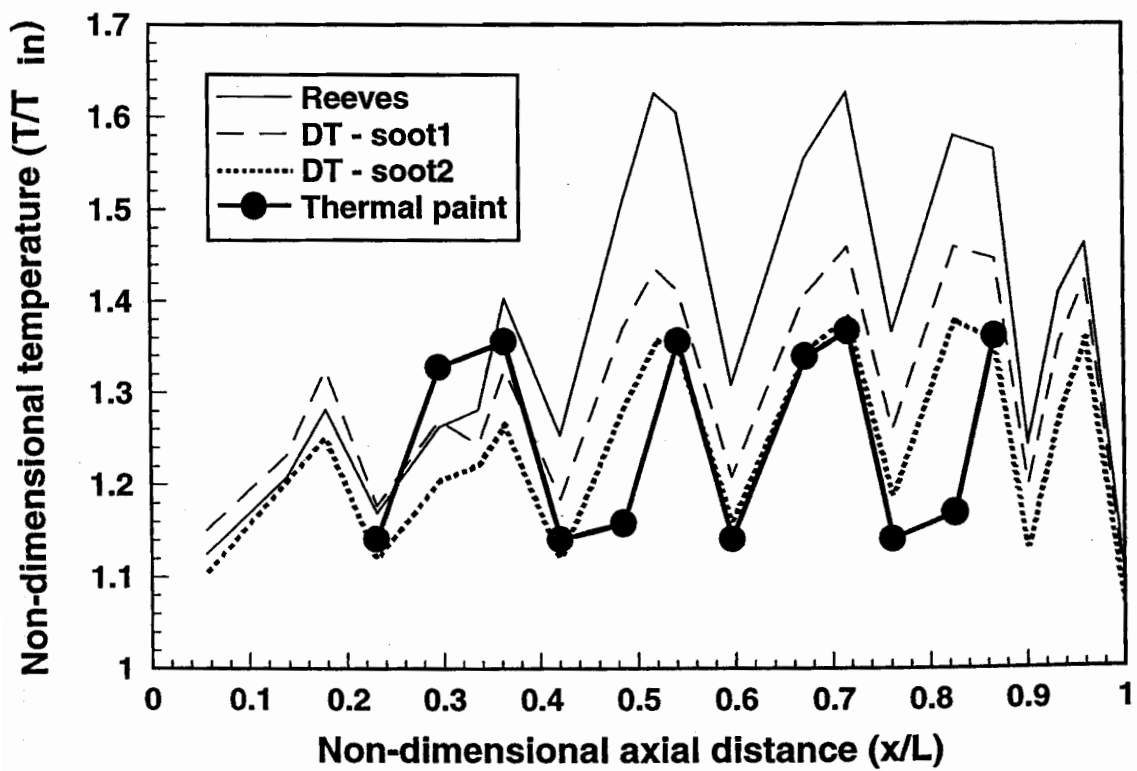


Figure 6.21. AC2 inner liner hot-side wall temperatures

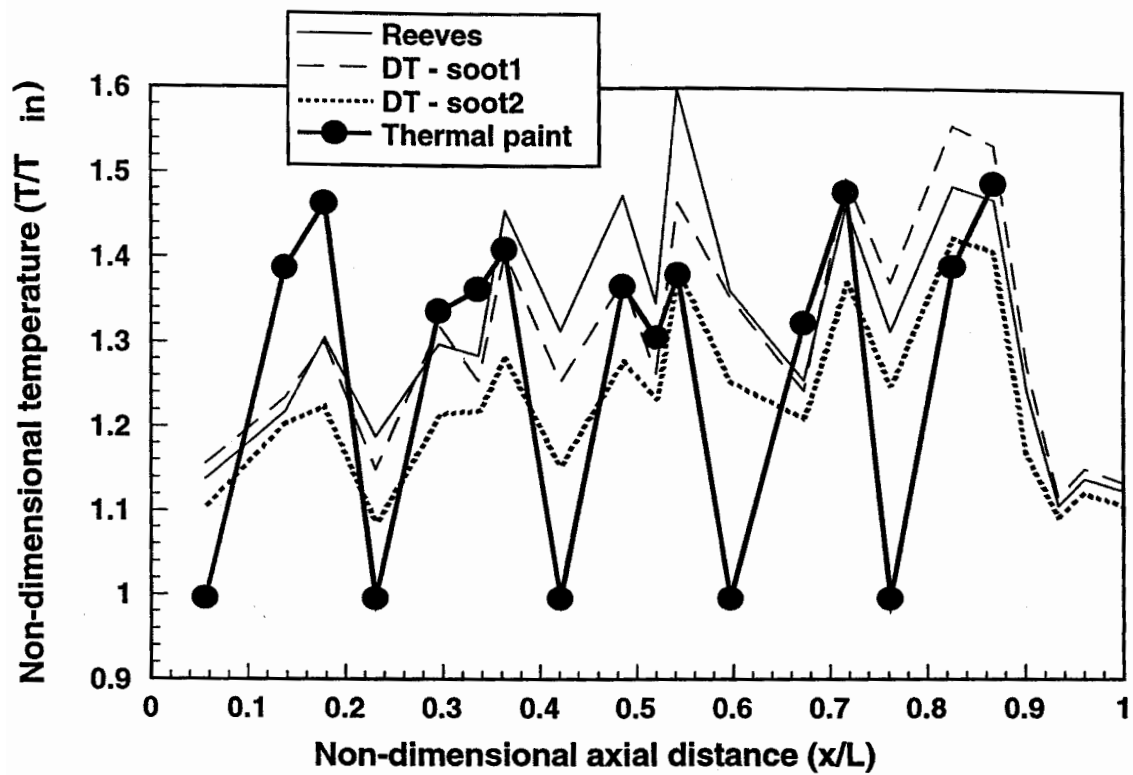


Figure 6.22. AC3 outer liner hot-side wall temperatures

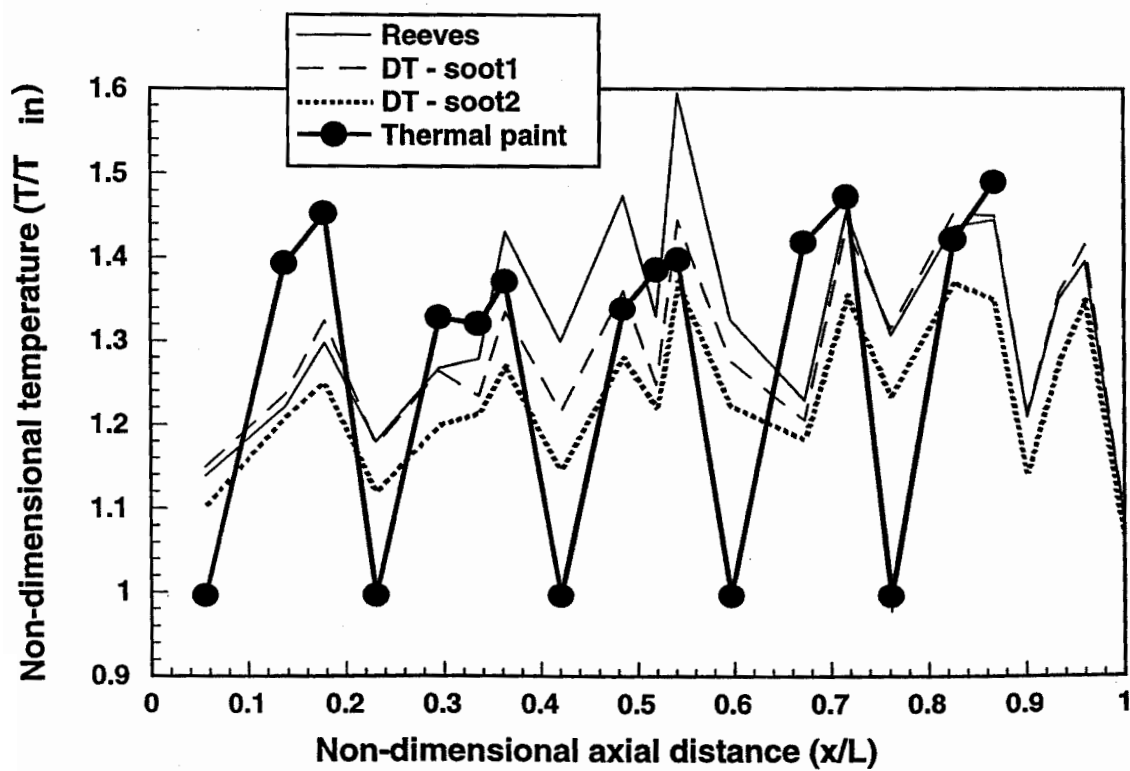


Figure 6.23. AC3 inner liner hot-side wall temperatures

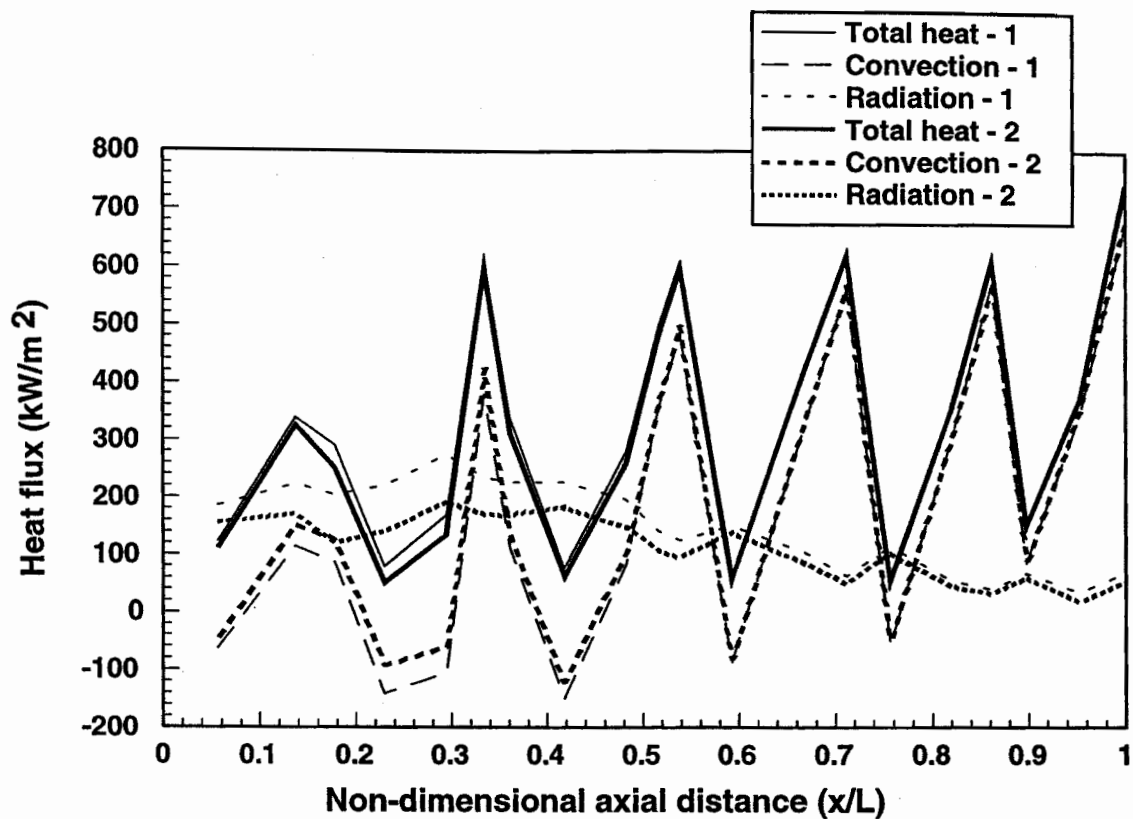


Figure 6.24. AC1 outer liner low order of magnitude soot profile heat flux comparison

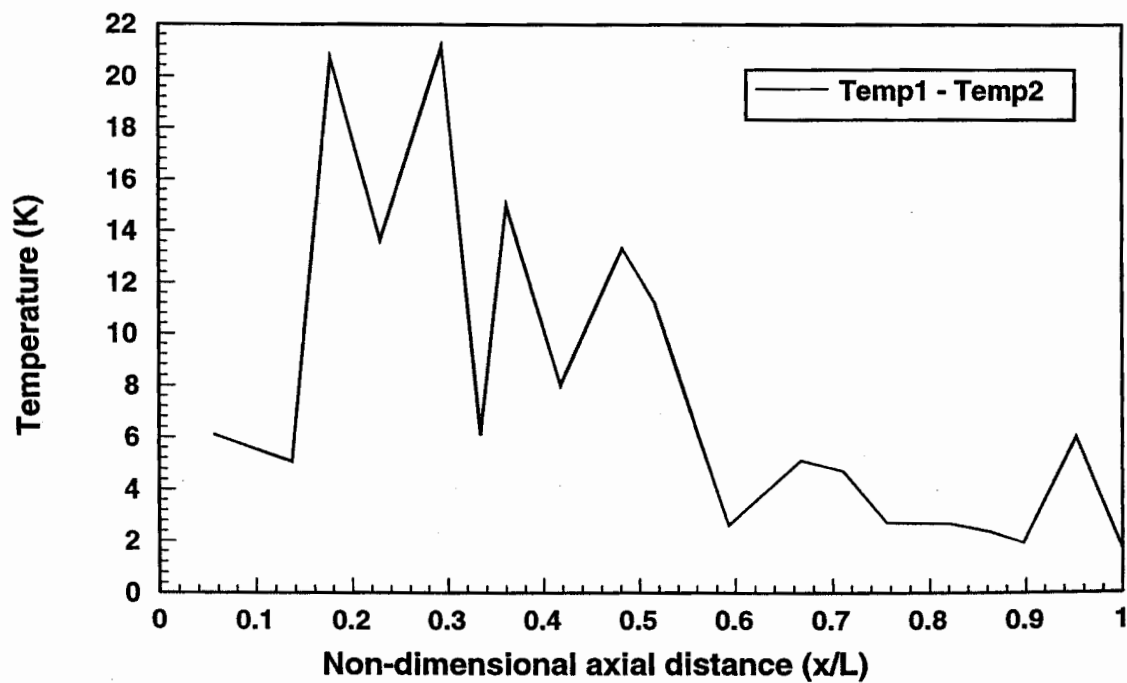


Figure 6.25. AC1 outer liner low order of magnitude soot profile  
wall temperature comparison

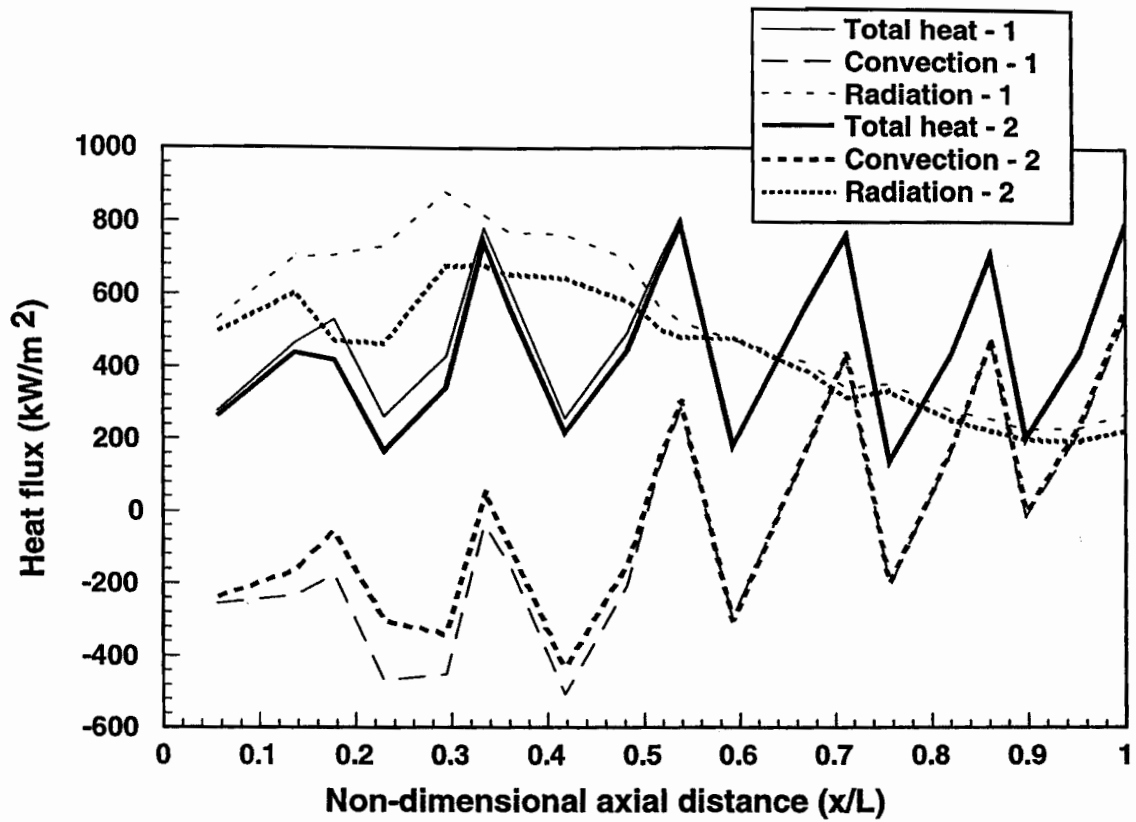


Figure 6.26. AC1 outer liner mid order of magnitude soot profile heat flux comparison

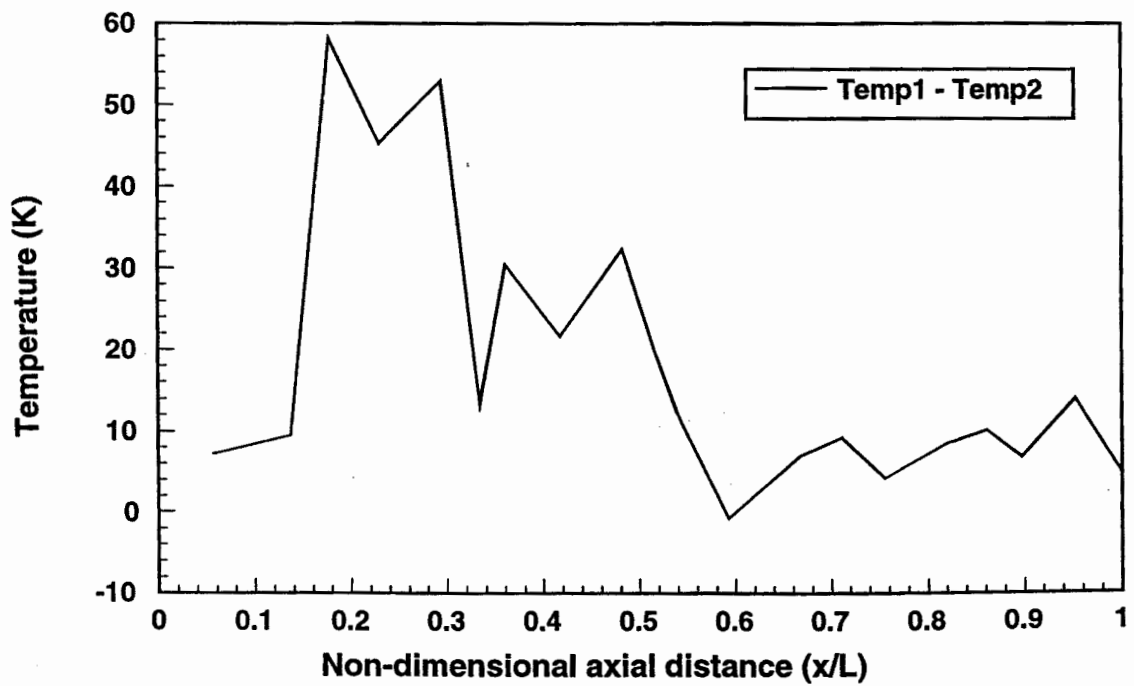


Figure 6.27. AC1 outer liner mid order of magnitude soot profile  
wall temperature comparison

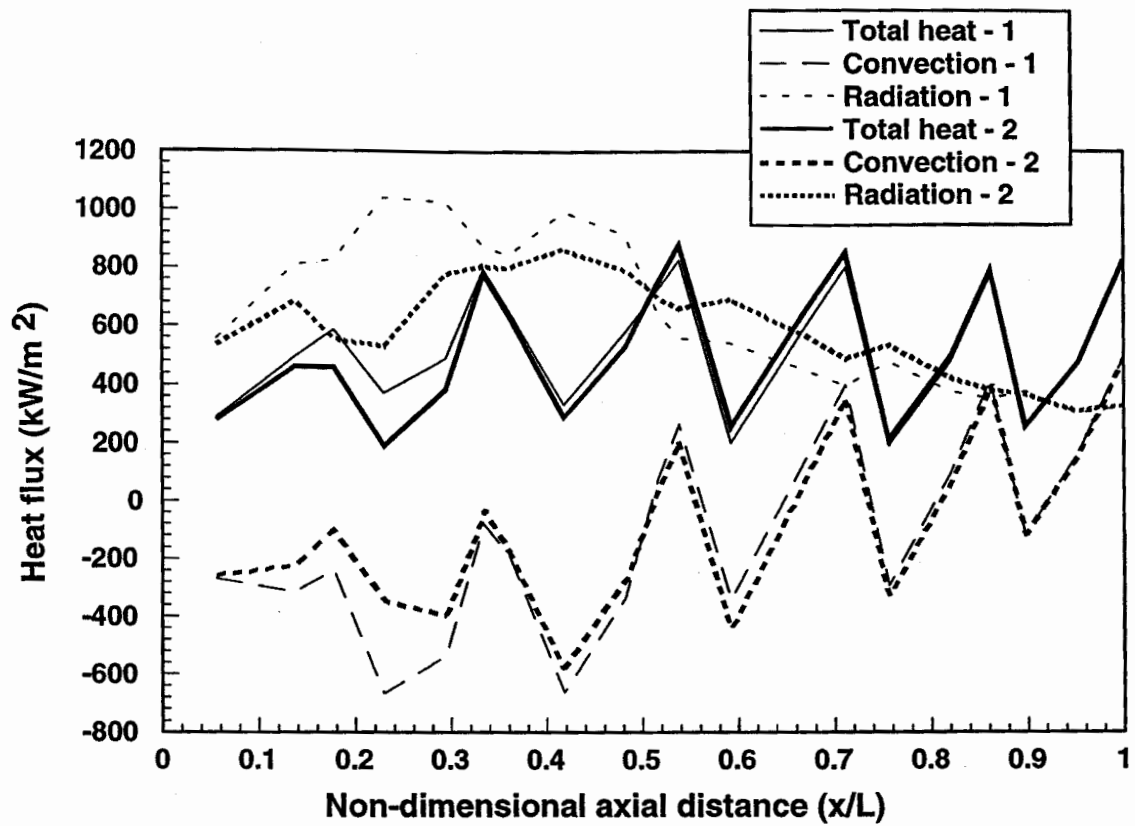


Figure 6.28. AC1 outer liner high order of magnitude soot profile heat flux comparison

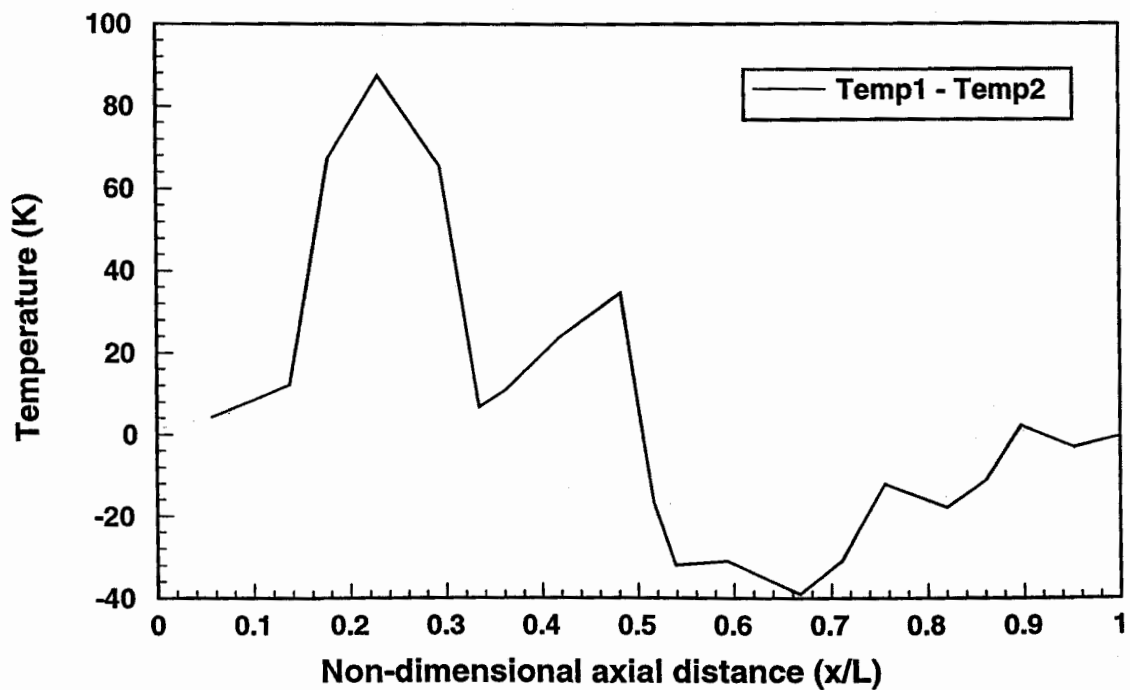


Figure 6.29. AC1 outer liner high order of magnitude soot profile  
wall temperature comparison



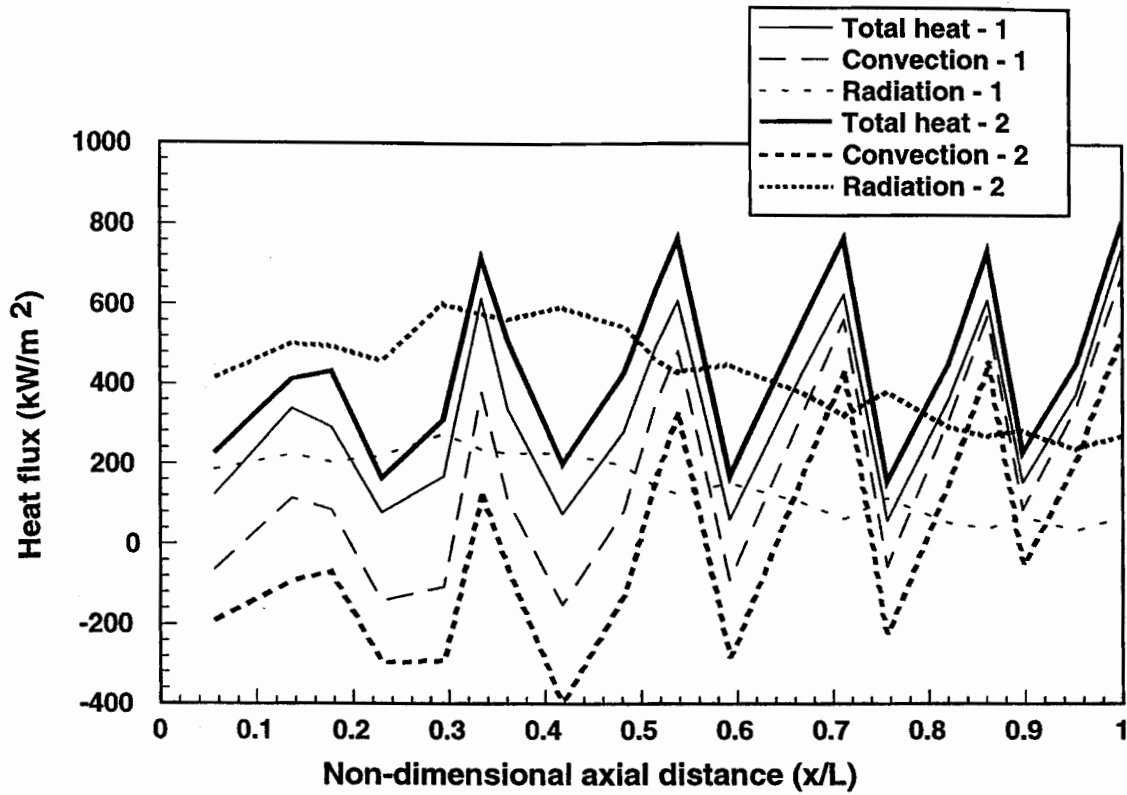


Figure 6.30. AC1 outer liner low order of magnitude soot, gas absorption  
heat flux comparison

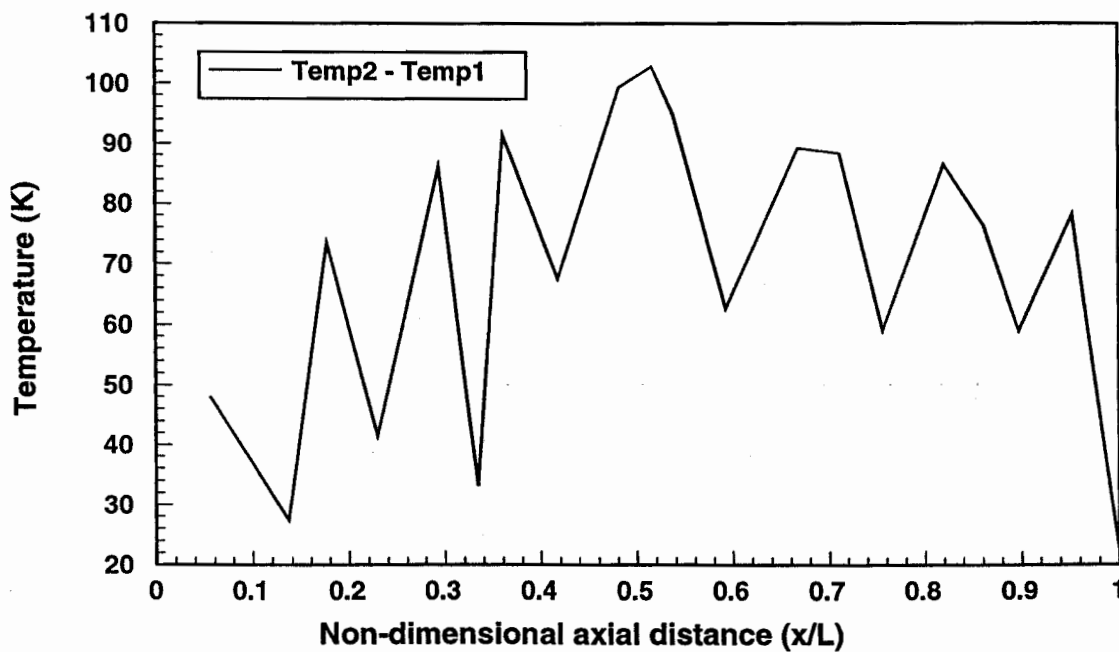


Figure 6.31. AC1 outer liner low order of magnitude soot, gas absorption  
wall temperature comparison

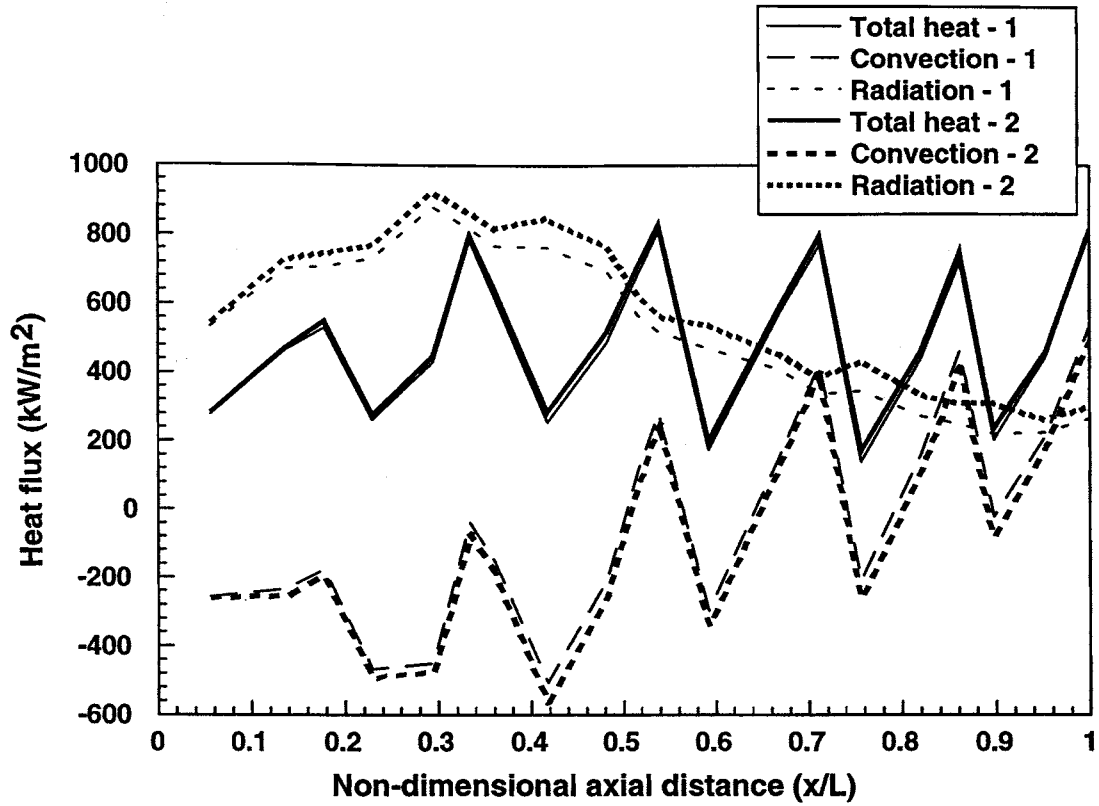


Figure 6.32. AC1 outer liner mid order of magnitude soot, gas absorption  
heat flux comparison

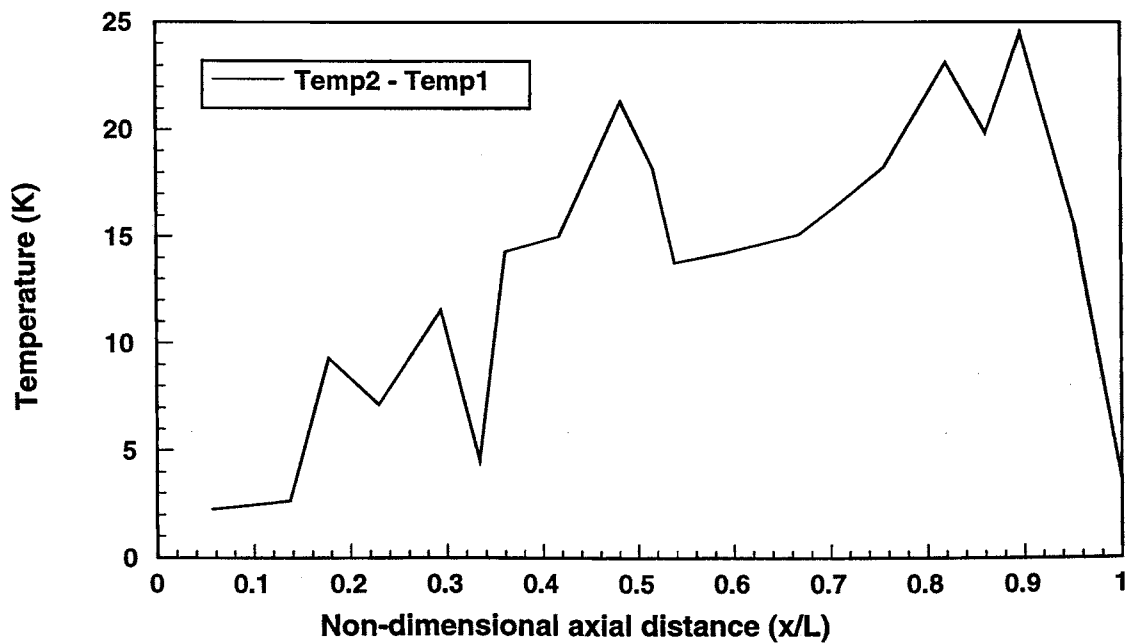


Figure 6.33. AC1 outer liner mid order of magnitude soot, gas absorption  
wall temperature comparison

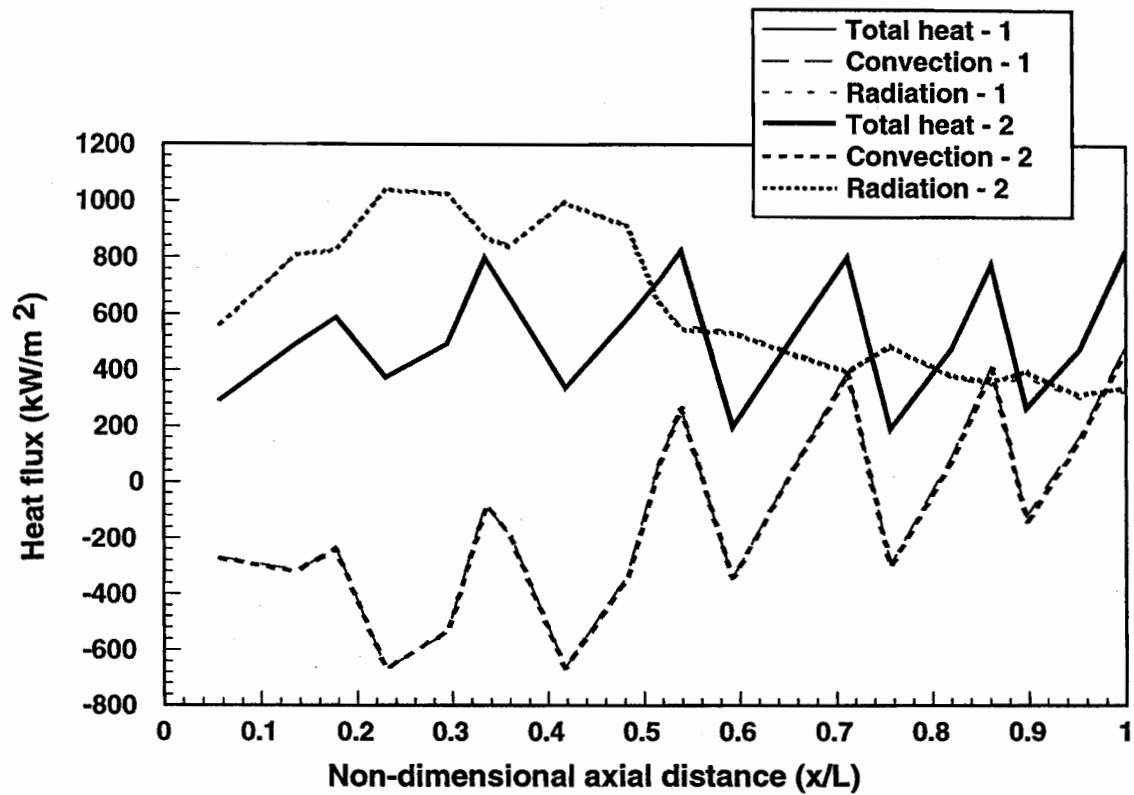


Figure 6.34. AC1 outer liner high order of magnitude soot, gas absorption  
heat flux comparison

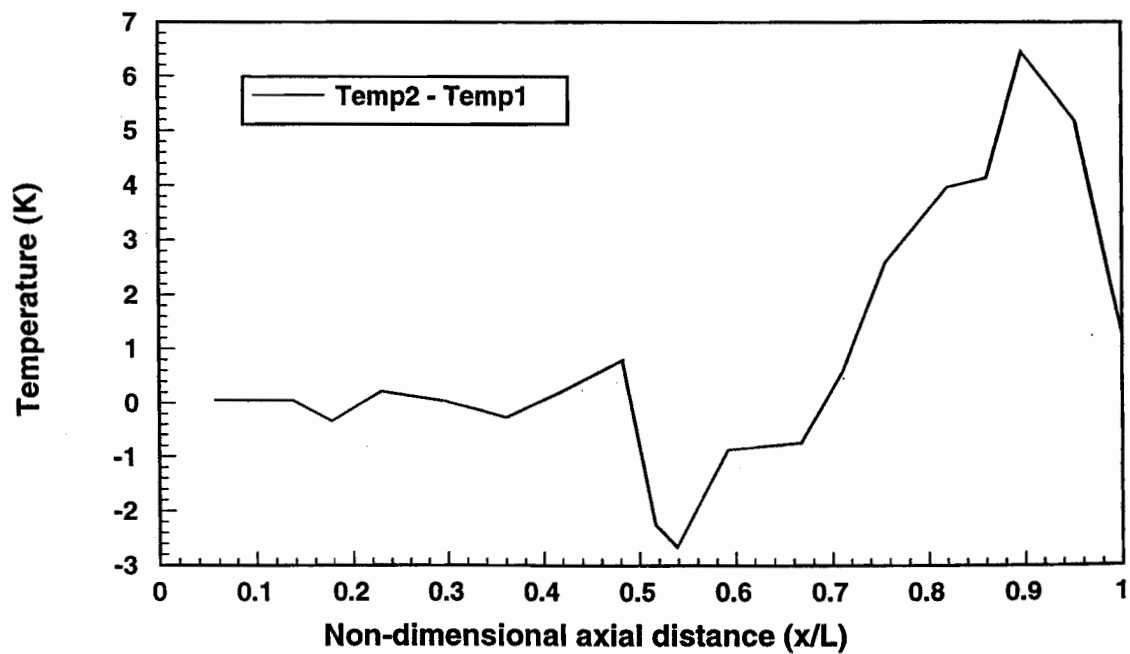


Figure 6.35. AC1 outer liner high order of magnitude soot, gas absorption  
wall temperature comparison

## 7. Conclusions

Preliminary gas turbine combustor design presents the difficult task of combining a wide range of sub-models in an unrestrictive, flexible, accurate and rapid solution procedure. A network approach has been successfully developed to meet these requirements providing a complete flow and heat transfer analysis.

Three annular combustors and a reverse flow combustor were used to validate the network flow solver. Comparisons of mass flow splits and pressure drops with proven numerical and experimental results in these cases illustrated the good accuracy of the network solver. A constrained equilibrium combustion model combined with a mixing and recirculation model provided local flame temperatures. The flow and energy equations were coupled to include the effects of the combustor temperature rise. No additional requirements or complexity were required in modelling the reverse flow combustor compared to the annular combustors.

A conjugate heat transfer analysis was developed for computing the liner wall heat transfer characteristics. A one-dimensional model accounted for radial conduction, and a two-dimensional model accounted for radial and axial conduction. Convection models included the effects of single or multiple cooling films, as well as the effects of heat pick-up by liner features within the wall itself. A number of correlations were included for modelling the effects of differing liner features in the development of cooling films. Initially a simple semi-empirical model was used for the flametube radiation calculation. Liner wall temperature comparisons between experimental thermal paint data and the network results illustrated qualitative accuracy. The wall temperature trends due to the liner cooling features were well captured by the network algorithm. The wide bands of the experimental thermal paint data limited the accuracy to which the predicted wall temperatures could be evaluated.

The flametube radiation model was identified as being of limited accuracy. A radiative heat transfer procedure was therefore developed, based upon the discrete transfer radiation model. The three-dimensional radiation model included the effects of gas and soot properties. Radial profiles of temperature and soot concentrations were incorporated to improve the accuracy of the radiation calculation. Three variations of a modern annular gas turbine combustor were used to evaluate the accuracy of the new procedure. Flametube hot-side experimental thermal paint data was found to compare well with the network results. Discrepancies between the calculated primary zone wall temperatures and measured values were attributed to short comings in the soot profiles used. Although the comparison remained limited by the width of the thermal paint bands, the bands were narrower than in the previous cases. The profile effects were found to be less critical downstream of the primary zone, in regions containing lower levels of soot. The effect of soot on the radiation calculation was typically much larger than the gas effects. However, the gas effects may be significant downstream of the primary zone where the soot levels decrease.

Radial soot and temperature distributions are unlikely to be known when designing a new combustor. However, physically realistic assumptions of soot concentrations, combined with a constrained equilibrium gas temperature should provide a reasonable evaluation of the wall temperature characteristics.

The network solver has proven successful in the modelling of rectangular, tubular, tubo-annular, annular, multi-annular, reverse flow, and lean pre-mixed combustors, as well as reheat systems, for both aeronautical and industrial applications.

A novel, versatile and accurate preliminary gas turbine combustor design algorithm, unconstrained by system geometry, has been developed using a network approach.

## 8. Recommendations for future work

The modular nature of the network algorithm makes it intentionally well suited to development by the inclusion of new sub-models. The development of the network solver highlighted areas of deficiency in the semi-empirical models used as well as the possibility of significantly extending the usefulness of a code of this type.

Improvements in the underlying sub-models will enhance the predictive capability of the network approach. The prediction of discharge coefficients from total-fed holes relies on experimental analysis performed of holes in cross flows. An experimental analysis of total-fed features, especially on the baseplate would lead to an improved empirical correlation for holes of this type. A similar analysis is required for angled effusion cooling patches. The film cooling effects generated by this feature also require clear definition through experimental analysis. Angled effusion is typically used on regions of the liner which experience unacceptably high thermal load, making the accurate modelling of the feature a necessity.

Thermal barrier coatings are becoming an increasingly popular method for lowering liner metal temperatures. There appears to be some uncertainty in the thermal conductivities of these materials at elevated temperatures. An accurate definition of thermal conductivity is required for the prediction of heat transfer, as only small variations in this already low value will have a significant effect on the heat flux predictions. Thermal barrier coatings are sprayed onto the inner surface of the flametube resulting in a rough finish. The significant surface roughness will effect the degradation of the cooling films, and enhance heat transfer from the flametube gases to the liner. Thermal barrier coating roughness has been found to have significant aerodynamic effect in gas turbine aerofoils (Watt et al, 1988). The effect the roughness has on the destruction of the liner cooling films needs to be investigated.

The accuracy of the network solver's heat transfer mechanism was evaluated using experimental thermal paint data in this work. The broad thermal paint bands limit the usefulness of the approach as a validation tool. Thermocouple measurements are required to substantiate the thermal paint data providing an improved baseline for comparison with the network predictions.

Measurements of soot and species concentrations within the flametube are a requirement for both this work and ongoing CFD development. Soot profiles derived from CFD and experimental analysis should be used to further evaluate the gas turbine combustor's radiative heat transfer mechanism.

Increasingly strict international emissions standards are of significant concern to the gas turbine industry. Gas turbine combustor emissions are currently the subject of much research and development. A number of semi-empirical models have been developed to predict levels of carbon monoxide, unburned hydrocarbons, and oxides of nitrogen (Lefebvre, 1995, Danis et al, 1996 and Connors et al, 1996). The existing components of the network model offer the basis for performing emissions predictions with relatively little effort.

Finally, the versatility, accuracy and speed of the network approach provides a very useful basis for design optimisation. The network algorithm is ideally suited for parametric analysis. However, the inclusion of a decision based algorithm would significantly enhance the fundamental design capability of the code. The highly non-linear, nature of the problem may be addressed using a genetic approach.

Genetic algorithms have been successfully employed in various design optimisation procedures (Gage, 1997). A genetic algorithm, coupled with the network solver developed here, has been used to demonstrate an autonomous gas turbine combustor design procedure with user specified performance criteria (Despierre, 1996 and Despierre et al, 1997). Although the analysis was only used to provide an initial demonstration of the method, the success achieved in optimising an existing annular

ombustor provided the confidence necessary to further develop this strategy in the future. The ability to optimise a gas turbine combustor geometry based upon performance requirements offers exciting prospects for the development of new and unusual designs.



## 9. References

- Acosta, W.A., 1987, "Liner Cooling Research at NASA Lewis Research Center", *AIAA* 87-1828.
- Adkins, R.C. and Gueroui, D., 1986, "An Improved Method for Accurate Prediction of Mass Flows through Combustor Liner Holes", *Journal of Engineering for Gas Turbines and Power*, Vol. 108, pp. 491-497.
- Al Dabagh, A.M., Andrews, G.E., Abdul Husain, R.A.A., Husain, C.I., Nazari, A. and Wu, J., 1990, "Impingement/Effusion Cooling: The Influence of the Number of Impingement Holes and Pressure Loss on the Heat Transfer Coefficient", *Journal of Turbomachinery*, Vol. 112, pp. 467-476.
- Anderson, D.A., Tannehill, J.C. and Pletcher, R.H., 1984, "Computational Fluid Mechanics and Heat Transfer", Hemisphere Publishing Corporation, U.S.A.
- Andrews, G.E., Alikhanizadeh, M., Asere, A.A., Hussain, C.I., Khoshkbar Azari, M.S. and Mkpadi, M.C., 1986, "Small Diameter Film Cooling Holes: Wall Convective Heat Transfer", *Journal of Turbomachinery*, Vol. 108, pp. 283-289.
- Andrews, G.E., Asere, A.A., Hussain, C.I. and Mkpadi, M.C., 1985, "Full Coverage Impingement Heat Transfer: The Variation in Pitch to Diameter Ratio at a Constant Gap", *Heat Transfer and Cooling in Gas Turbines*, AGARD CPP 390, No. 26.
- Bai, X.S. and Fuchs, L., 1994, "Numerical Computation of Turbulent Combustion and Thermal Radiation in Gas Turbine Combustion Chambers", *ICAS-94-6.6.1*, pp. 2098-2106.

Bai, X.S. and Fuchs, L., 1995, "Sensitivity Study of Turbulent Reacting Flow Modelling in Gas Turbine Combustors", *AIAA Journal*, Vol. 33, No. 10, pp.1857-1864.

Ballal, D.R. and Lefebvre, A.H., 1972, "A Proposed Method for Calculating Film-Cooled Wall Temperatures in Gas Turbine Combustion Chambers", *ASME 72-WA/HT-24*.

Baukal, C.E. and Gebhart, B., 1996, "A Review of Semi-empirical Solutions for Flame Impingement Heat Transfer", *International Journal of Heat and Mass Transfer*, Vol. 39, No. 14, pp. 2989-3002.

Beer, J.M., 1995, "Clean Combustion in Gas Turbines: Challenges and Technical Responses - A Review", *Journal of the Institute of Energy*, Vol. 68, pp. 2-10.

Bejan, A., 1993, "Heat Transfer", John Wiley, U.S.A.

Bilger, R.W., 1976, "Turbulent Jet Diffusion •Flames", *Progress in Energy and Combustion Science*, Vol. 1, pp. 87-109.

Boyce, R., 1996, *Private Communication*, Rolls-Royce plc, Derby, U.K.

Bressloff, N.W., Moss, J.B., Rubini, P.A., 1995, "Application of a New Weighting Set for Discrete Transfer Radiation Model", *Proceedings of the 3rd European Conference on Industrial Furnaces and Boilers*, Lisbon, Portugal.

Bressloff, N.W., Moss, J.B., Rubini, P.A., 1996, "Assessment of a Differential Total Absorptivity Solution to the Radiative Transfer Equation as Applied in the Discrete Transfer Radiation Model", *Numerical Heat Transfer, Part B*, Vol. 29, No. 3, pp. 381-397.

ressloff, N.W., 1996, "CFD Prediction of Coupled Radiation Heat Transfer and Soot Production in Turbulent Flames", PhD Thesis, School of Mechanical Engineering, Cranfield University, England.

rocklehurst, H.T., Priddin, C.H. and Moss, J.B., 1997, "Soot Predictions within an Aero Gas Turbine Combustion Chamber", to appear in *ASME/IGTI Turbo Expo '97*, Orlando, U.S.A.

Juruss, D.L., Shyy, W. and Braaten, M.E., 1987, "Numerical model for analytical predictions of combustor aerothermal performance characteristics", *APGARD CP 422*, J.S.A.

Carlson and Stoner, 1977, "Thermal Barrier Coating and High Temperature Industrial Gas Turbine", *NASA CR 135147*.

Carvalho, M.G. and Coelho, P.J., 1989, "Heat Transfer in Gas Turbine Combustors", *Journal of Thermophysics*, Vol. 3, No. 2, pp. 123-131.

Carvalho, M.G., Durao, D.F.G. and Lockwood, F.C., 1985, "Computation of Thermal Radiation for Gas Turbine Conditions", *Proceedings of the 65th AGARD/PEP Symposium*, CP-390, pp. 201-207.

Chui, E.H., Hughes, P.M.J. and Raithby, G.D., 1993, "Implementation of the Finite Volume Method for Calculating Radiative Heat Transfer in a Pulverised Fuel Flame", *Combustion Science and Technology*, Vol. 92, pp. 225-242.

Coalmer, M.S. and Vafai, K., 1995, "Investigation of the Heat Transfer Characteristics of a Typical Annular Combustion Chamber of an Industrial Gas Turbine", *Heat Transfer Engineering*, Vol. 16, No. 4, pp. 17-27.

Connors, C.S., Barnes, J.C., and Mellor, A.M., 1996, "Semi-empirical Predictions and Correlations of CO Emissions from Utility Combustion Turbines", *Journal of Propulsion and Power*, Vol. 12, No. 5, pp. 926-932.

Cross, H., 1936, "Analysis of Flow in Networks of Conduits or Conductors", *Bulletin* no. 286, University of Illinois Engineering Experimental Station, Urbana, Illinois, U.S.A.

Cumber, P.S., 1995, "Improvements to the Discrete Transfer Method of Calculating Radiative Heat Transfer", *International Journal of Heat and Mass Transfer*, Vol. 38, No. 12, pp. 2251-2258.

Danis, A.M., Burrus, D.L. and Mongia, H.C., 1996, "Anchored CCD for Gas Turbine Combustor Design and Data Correlation", *ASME Paper 96-GT-143*.

Danis, A.M., Pritchard, B.A. and Mongia, H.C., 1996, "Empirical and Semi-empirical Correlation of Emissions Data from Modern Turbopropulsion Gas Turbine Engines", *ASME Paper 96-GT-86*.

De Ris, R., 1979, "Fire Radiation - A Review", *Proceedings of the Seventeenth Symposium (International) on Combustion*, pp. 1003-1016.

Denison, M.K., and Webb, B.W., 1995, "The Spectral Line-Based Weighted-Sum-of-Gray-Gas Model in Non-isothermal Non-homogeneous Media", *Journal of Heat Transfer*, Vol. 117, pp. 359-365.

Despierre, A., 1996, "Gas Turbine Combustor Design Using Genetic Algorithms", MSc Thesis, School of Mechanical Engineering, Cranfield University, England.

Despierre, A., Stuttaford, P.J. and Rubini P.A., 1997, "Preliminary Gas Turbine Combustor Design Using a Genetic Algorithm", to be presented at *ASME Turbo Expo '97*, Orlando, U.S.A.

Docherty, P., 1982, "Prediction of Gas Emissivity for a Wide Range of Process Conditions", *Proceedings of the 7th International Heat Transfer Conference*, Vol. 2, pp. 481-485.

Dorignac, E. and Vullierme, J.J., 1995, "Experimental Study on the Transfer Coefficients of a Cooling Film on a Non-athermanous Plate: Effect of Injection Geometry", *International Journal of Heat and Mass Transfer*, Vol. 39, No. 9, pp. 1935-1951.

Dupuis, P., Robert, J.L. and Ouellet, Y., 1987, "A Modified Element Method for Pipe Network Analysis", *Journal of Hydraulic Research*, Vol. 25, No. 1, pp. 27-40.

Edwards, D.K. and Balakrishnan, A., 1973, "Thermal Radiation by Combustion Gases", *International Journal of Heat and Mass Transfer*, Vol. 16, pp. 25-40.

Edwards, D.K. and Matavosian, R., 1984, "Scaling Rules for Total Absorptivity and Emissivity of Gases", *Journal of Heat Transfer*, Vol. 106, pp. 684-689.

ESDU, 1973, Engineering Sciences Data Unit Item No. 73017, Aerodynamics Vol. 6.

ESDU, 1978, Engineering Sciences Data Unit Item No. 77031, Heat Transfer by Free Convection and Radiation, Heat Transfer Vol. 2.

Farag, I.H., 1982, "Non-Luminous Gas Radiation: Approximate Emissivity Models", *Proceedings of the 7th International Heat Transfer Conference*, Vol. 2, pp. 487-492.

Freeman, B.C., 1965, "Discharge Coefficients of Combustion Chamber Dilution Holes", MSc thesis, College of Aeronautics, Cranfield University, England.

Folayan, C.O. and Whitelaw, J.H., 1977, "Impingement Cooling and its Application to Combustor Design", *Proceedings of the Tokyo Joint Gas Turbine Congress*, pp. 69-76.

Gage, P.J., 1997, "A Genetic Approach to Modelling Flight Dynamic Characteristics", *AIAA 97-0536*.

Gardiner, J., 1995, Private Communication, Rolls-Royce, U.K.

Gordon, S. and McBride, B.J., 1971, "Computer Program for Calculation of Complex Chemical Equilibrium Compositions, Rocket Performance, Incident and Reflected Shocks, and Chapman-Jouget Detonations", *NASA SP-273*, U.S.A.

Gnielinski, V., 1976, "New Equations for Heat and Mass Transfer in Turbulent Pipe and Channel Flow", *International Chemical Engineering*, Vol. 16, No. 2, pp. 359-368.

Gupta, A.K. and Lilley, D.G., 1994, "Combustion and Environmental Challenges for Gas Turbines in the 1990s", *Journal of Propulsion and Power*, Vol. 10, No. 2, pp. 137-147.

Greyvenstein, G.P. and Laurie, D.P., 1994, "A Segregated CFD Approach to Pipe Network Analysis", *International Journal for Numerical Methods in Engineering*, Vol. 37, pp. 3685-3705.

Hammond, D.C. and Mellor, A.M., 1970, "A Preliminary Investigation of Gas Turbine Combustor Modelling", *Combustion Science and Technology*, Vol. 2, pp. 67-80.

Hanson, R.K., 1997, "Recent Advances in Laser-based Combustion Diagnostics", *AIAA-97-0115*.

Holdeman, J.D., Mongia, H.C., and Mularz, E.J., 1989, "Assessment, Development, and Application of Combustor Aerothermal Models", *NASA TM-4087*, U.S.A.

Holdeman, J.D., Srinivasan, R. and White, C.D., 1988, "An Empirical Model of the Effects of Curvature and Convergence on Dilution Jet Mixing", *AIAA-88-3180*.

Hottel, H.C., 1954, "Radiant Heat Transmission", *Heat Transmission*, ed. McAdams, W.H., 3rd edition, Ch. 4, McGraw-Hill, U.S.A.

Hottel, H.C., and Sarofim, A.F., 1967, "Radiative Transfer", McGraw-Hill, U.S.A.

Jeppson, R.W., 1977, "Analysis of Flow in Pipe Networks", Ann Arbor Science, Michigan, U.S.A.

Kaddah, K.S., 1964, "Discharge Coefficients and Jet Deflection Angles for Combustor Liner Air Entry Holes", MSc thesis, College of Aeronautics, Cranfield University, England.

Kapat, J.S. and Yang, T., 1992, "Liner Heat Loss in a Gas Turbine Combustor", *Fundamental and Applied Heat Transfer Research for Gas Turbine Engines*, HTD-Vol. 226, ASME, pp. 71-77.

Kindle, J.H., 1950, "Theory and Problems of Plane and Solid Analytic Geometry", Schaum's Outline Series, McGraw-Hill Book Company, U.S.A.

Le Grives, E., Nicolas, J.J. and Genot, J., 1979, "Internal Aerodynamics and Heat Transfer Problems Associated to Film Cooling of Gas Turbines", *ASME Paper 79-GT-57*.

Klein, A., 1995, "Characteristics of Combustor Diffusers", *Progress in Aerospace Science*, Vol. 31, pp. 171-271.

Leckner, B., 1972, "Spectral and Total Emissivity of Water Vapour and Carbon Dioxide", *Combustion and Flame*, Vol. 19, pp. 33-48.

Lefebvre, A.H., 1983 "Gas Turbine Combustion", McGraw-Hill Book Company, U.S.A.

Lefebvre, A.H., 1984, "Flame radiation in gas turbine combustion chambers", *International Journal of Heat and Mass Transfer*, Vol. 27, No. 9, pp. 1493-1510.

Lefebvre, A.H., 1995, "The Role of Fuel Preparation in Low-Emission Combustion", *Journal of Engineering for Gas Turbines and Power*, Vol. 117, pp. 617-654.

Liebert, C.H., 1978, "Emittance and Absorptance of the National Aeronautics and Space Administration Ceramic Thermal Barrier Coatings", *Thin Solid Films*, 53, pp. 235-240.

Lockwood, F.C. and Shah, N.G., 1981, "A New Radiation Solution Method for Incorporation in General Combustion Prediction Procedures", *Proceedings of the Eighteenth Symposium (International) on Combustion*, pp. 1405-1414.

Lowe, D.R., 1996, Private Communication, Rolls-Royce, England.

Lukash, V.P., 1970, "Calculation of Emissivity of Hydrocarbon Fuel Combustion Products ( $\text{CO}_2$  and  $\text{H}_2\text{O}$ ) at High Temperatures and Pressures", *Teplofizika Vysokikh Temperatur*, Vol. 9, No. 4, pp. 647-653.

Maciejewski, P.K. and Anderson, A.M., 1996, "Elements of a General Correlation for Turbulent Heat Transfer", *Journal of Heat Transfer*, Vol. 118, pp. 287-293.

Mado, R.J., and Roberts, R., 1974, "A Pollutant Emissions Prediction Model for Gas Turbine Combustors", *AIAA-74-1113*.

Magnussen, B.F. and Hjertager, B.H., 1976, "On Mathematical Modelling of Turbulent Combustion with Special Emphasis on Soot Formation and Combustion", *Sixteenth Symposium (International) on Combustion*, The Combustion Institute, pp. 719-729.



Malalasekera, W.M.G. and James, E.H., 1996, "Radiative Heat Transfer Calculations in Three-Dimensional Complex Geometries", *Journal of Heat Transfer*, Vol. 118, pp. 225-228.

Marek, C.J. and Tacina, R.R., 1975, "Effect of Free Stream Turbulence on Film Cooling", *NASA TN D-7958*.

Mattingly, J.D., 1996, "Elements of Gas Turbine Propulsion", McGraw-Hill Inc., U.S.A.

Mavris, D.N. and Roth, B.A., 1997, "A Methodology for the Robust Cooling Design of an HSCT Combustor Liner", *AIAA-97-0288*.

Mellor, A.M., 1978, "Turbulent-Combustion Interaction Models for Practical High Intensity Combustors", *Seventeenth Symposium on Combustion*, The Combustion Institute, pp. 377-387.

Mellor, A.M. and Fritsky, K.J., 1990, "Turbine Combustor Preliminary Design Approach", *Journal of Propulsion and Power*, Vol. 6, no. 3, pp. 334-343.

Mellor, A.M. (ed.), 1990, "Design of Modern Turbine Combustors", Academic Press, England.

Menguc, M.P., Cummings, W.G. and Viskanta, R., 1985, "Radiative Transfer in a Gas Turbine Combustor", *AIAA Paper no. AIAA-85-1072*.

Metcalf, M., 1996, *Private Communication*, Rolls-Royce plc, Derby, U.K.

Modak, A.T., 1979, "Radiation from Products of Combustion", *Fire Research*, Vol. 1, pp. 339-361.

Modest, M.F., 1991, "The Weighted-Sum-of-Gray-Gases Model for Arbitrary Solution Methods in Radiative Transfer", *Journal of Heat Transfer*, Vol. 113, pp. 650-656.

Modest, M.F., 1993, "Radiative Heat Transfer", McGraw-Hill Inc., U.S.A.

Mongia, H.C., 1994, "Combustor Modelling in Design Process: Applications and Future Directions", *AIAA Paper no. AIAA-94-0466*.

Mongia, H.C., Reynolds, R.S., and Srinivasan, R., 1986, "Multidimensional Gas Turbine Combustion Modelling: Applications and Limitations", *AIAA Journal*, Vol. 24, no. 6, pp. 890-904.

Mosier, S.A., Roberts, R., and Henderson, R.E., 1973, "Development and Verification of an Analytical Model for Predicting Emissions from Gas Turbine Combustors during Low-Power Operations", *AGARD-CP-125*, pp. 25-1 - 25-12, England.

Murthy, J.N., 1988, "Gas Turbine Combustor Modelling for Design", PhD Thesis, School of Mechanical Engineering, Cranfield University, England.

Najjar, Y.S.H. and Goodger, E.M., 1981a, "Soot Formation in Gas Turbines using Heavy Fuels. 1.", *Fuel*, Vol. 60, pp. 980-986.

Najjar, Y.S.H. and Goodger, E.M., 1981b, "Soot Oxidation in Gas Turbines using Heavy Fuels. 2.", *Fuel*, Vol. 60, pp. 987-990.

Nogueira, A.C., 1993, "Steady-state Fluid Network Analysis", *Journal of Hydraulic Engineering*, Vol. 119, No. 3, pp. 431-436.

Notter, R.H. and Sleicher, C.A., 1972, "A Solution to the Turbulent Graetz problem - III Fully Developed and Entry Region Heat Transfer Rates", *Chemical Engineering Science*, Vol. 27, pp. 2073-2093.

Oates, G.C., 1989, "Aircraft Propulsion Systems Technology and Design", American Institute of Aeronautics and Astronautics Inc., U.S.A.

Oechsle, V.L. and Mongia, H.C., 1993, "An Analytical Study of Dilution Jet Mixing in a Cylindrical Duct", *AIAA-93-2043*.

Oppenheim, A.K., 1954, "Radiation Analysis by the Network Method", *Transactions of the American Society of Mechanical Engineers*, Vol. 78, pp. 725-735.

Ozisik, M.N., 1985, "Heat Transfer: A Basic Approach", McGraw-Hill, U.S.A.

Paskin, M.D. and Mongia, H.C., 1993, "An Efficient Liner Cooling Scheme for Advanced Small Gas Turbine Combustors", *AIAA-93-1763*.

Patankar, S.V., 1980, "Numerical Heat Transfer and Fluid Flow", Hemisphere Publishing Corporation, U.S.A.

Poferl, D.J., Svehla, R.A. and Lewandowski, K., 1969, "Thermodynamic and Transport Properties of Air and the Combustion Products of Natural Gas and ASTM-A-1 Fuel with Air", *NASA TN D-5452*.

Poferl, D.J. and Svehla, R.A., 1973, "Thermodynamic and Transport Properties of Air and its Products of Combustion with ASTM-A-1 Fuel and Natural Gas at 20, 30 and 40 Atmospheres", *NASA TN D-7488*.

Rizk, N.K. and Mongia, H.C., 1991, "Three-Dimensional Analysis of Gas Turbine Combustors", *Journal of Propulsion and Power*, Vol. 7, No. 3, pp. 445-451.

Rodriguez, C.G. and O'Brien, W.F., 1997, "One-dimensional, steady model for Straight and Reverse Flow Gas Turbine Combustors", *AIAA-97-0289*.

Saad, M.A., 1985, "Compressible Fluid Flow", Prentice-Hall, U.S.A.

Schwarz, H.R., 1989, "Numerical Analysis: A Comprehensive Introduction", Anchor Press, Great Britain.

Shah, N.G., 1979, "New Method of Computation of Radiant Heat Transfer in Combustion Chambers", PhD Thesis, University of London.

Shah, R.K. and Johnson, R.S., 1981, "Correlations for Fully-developed Turbulent Flow through Circular and Non-Circular Channels", *Proceedings of the Sixth National Heat and Mass Transfer Conference*.

Shames, I.H., 1982, "Mechanics of Fluids", McGraw-Hill Book Company, U.S.A.

Shyy, W., Braaten, M.E. and Burrus, D.L., 1989, "Study of three-dimensional Gas-Turbine Combustor Flows", *International Journal of Heat and Mass Transfer*, Vol. 32, No. 6, pp. 1155-1164.

Siegel, R. and Howell, J.R., 1992, "Thermal Radiation Heat Transfer, Third Edition", Hemisphere Publishing Corporation, U.S.A.

Simon, F.F., 1986, "Jet Model for Slot Film Cooling With Effect of Free-Stream and Coolant Turbulence", *NASA TP 2655*.

Simon, D., Schubert, D. and Basler, U., 1984, "Advanced Combustor Liner Cooling Concepts", *Combustion Problems in Turbine Engines, AGARD -CP-353*, No. 24.

Smith, I.E., 1966, "The Application of Transpiration Cooling Methods to Gas Turbine Combustion Chambers", *College of Aeronautics Memo No. 97*, Cranfield University, England.

Sommer, R., Ammermann, D. and Hennig, E., 1993, "More Efficient Algorithms for Symbolic Network Analysis: Supernodes and Reduced Loop Analysis", *Analog Integrated Circuits and Signal Processing*, Vol. 3, pp. 73-83.

Spalding, D.B., 1971, "Mixing and Chemical Reaction in Steady Confined Turbulent Flames", *Thirteenth Symposium (International) on Combustion*, The Combustion Institute, pp. 647-657.

Srivasta, S.K., 1982, "Computations of soot and NO<sub>x</sub> emissions from Gas Turbine Combustors", *NASA CR-167930*, U.S.A.

Steward, F.R. and Kocaefer, Y.S., 1986, "Total Emissivity and Absorptivity Models for Carbon Dioxide, Water Vapour and their Mixtures", *Heat Transfer 1986*, Vols. 1-6, Ch. 479, pp. 735-740.

Sturgess, G.J., 1986, "Design of Combustor Cooling Slots for High Film Effectiveness: Part I - Film General Development", *Journal of Engineering for Gas Turbines and Power*, Vol. 108, pp. 354-360.

Sturgess, G.J. and Pfeifer, G.D., 1986, "Design of Combustor Cooling Slots for High Film Effectiveness: Part II - Film Initial Region", *Journal of Engineering for Gas Turbines and Power*, Vol. 108, pp. 361-369.

Sturgess, G.J., 1969, "Correlation of Data and Prediction of Effectiveness from Film Cooling Injection Geometries of a Practical Nature", in Norster, E.R. (ed.), *Cranfield International Propulsion Symposium*, Vol. 11, pp. 229-250, England.

Stuttaford, P.J., Anghaie, S. and Shyy, W., 1995, "Computation of high-temperature near-wall heat transfer using an enthalpy balancing scheme", *International Journal of Heat and Mass Transfer*, Vol. 38, No. 1, pg. 55-64.

Stuttaford, P.J. and Rubini, P.A., 1996, "Preliminary Gas Turbine Combustor Design Using a Network Approach", *ASME Paper 96-GT-135*, to appear in the *Journal of Engineering for Gas Turbines and Power*.

Stuttaford, P.J. and Rubini, P.A., 1997, "Assessment of a Radiative Heat Transfer Model for a New Gas Turbine Combustor Preliminary Design Tool", *AIAA 97-0294*, also submitted to the *Journal of Propulsion and Power*.

Sudarev, A.V. and Antonovsky, V.I., 1990, "Soot Content in a Gas Turbine Combustion Chamber", *Low Grade Fuels*, Vol. 2, Ch. 36, pp. 431-441.

Swithenbank, J., Poll, I., and Vincent, M.W., 1973, "Combustion Design Fundamentals", *Fourteenth Symposium (International) on Combustion*, The Combustion Institute, pp. 627-638.

Switzer, G., Sturgess, G., Sloan, D. and Shouse, D., 1994, "Relation of CARS Temperature Fields to Lean Blow-out Performance in an Aircraft Gas Turbine Generic Combustor", *AIAA-94-3271*.

Ti, H.C., and Preece, P.E., 1992, "Large-scale Fluid Network Analysis: Mixed Pressure and Flow Specifications", *The Chemical Engineering Journal*, Vol. 50, pp. 133-141.

Tien, C.L. and Lee, S.C., 1982, "Flame Radiation", *Progress in Energy Combustion Science*, Vol. 8, pp. 41-59.

Vafai, K., 1996, Private Communication, Ohio State University, U.S.A.

Viskanta, R. and Menguc, M.P., 1987, "Radiation Heat Transfer in Combustion Systems", *Progress in Energy and Combustion Science*, Vol. 13, pp. 97-160.

Watt, R.M., Allen, J.L., Baines, N.C., Simons, J.P. and George, M., 1988, "A Study of the Effects of Thermal Barrier Coating Surface Roughness on the Boundary Layer Characteristics of Gas Turbine Aerofoils", *Journal of Turbomachinery*, Vol. 110, pp. 88-93.

Wood, D.J. and Rayes, A.G., 1981, "Reliability of Algorithms for Pipe Network Analysis", *Journal of the Hydraulics Division*, ASCE, Vol. 107, No. HY10, pp. 1145-1161.

Zelina, J., Blust, J.W., and Ballal, D.R., 1996, "Combustion of Liquid Fuels in the Well Stirred Reactor", *ASME Paper no. 96-GT-47*.